UNIVERSITY OF OKLAHOMA
GRADUATE COLLEGE

LEVERAGING NEWLY-DEVELOPED ALGORITHMS TO INVESTIGATE THE IMPACTS OF EMERGING WIND FARMS ON BOUNDARY-LAYER FEATURES

A DISSERTATION
SUBMITTED TO THE GRADUATE FACULTY
in partial fulfillment of the requirements for the
Degree of
DOCTOR OF PHILOSOPHY

by ARIANNA MARIE JORDAN
Norman, Oklahoma
2026

Downloaded from SHAREOK. Persistent Handle URL: https://hdl.handle.net/11244/342667

LEVERAGING NEWLY-DEVELOPED ALGORITHMS TO INVESTIGATE THE IMPACTS OF EMERGING WIND FARMS ON BOUNDARY-LAYER FEATURES

A DISSERTATION APPROVED FOR THE
SCHOOL OF METEOROLOGY

BY THE COMMITTEE CONSISTING OF

Dr. Petra Klein (Chair)

Dr. Elizabeth Smith

Dr. Scott Salesky

Dr. Marcela Loría-Salazar

Dr. Lee Fithian

Dr. Sonia Wharton

©Copyright by ARIANNA MARIE JORDAN 2026

All Rights Reserved.

Acknowledgments

It is 5:00 A.M. Berlin time, and I couldn't be more wide awake, because writing these acknowledgments is so surreal and bittersweet in ways I cannot even begin to explain. Because even though I followed the process as I was supposed to, there was always a hint of self doubt to make me think I wouldn't actually make it to this point. I have never been someone for whom knowledge comes easily or instantly. I do not have a photography memory or a mind that absorbs information like a sponge. In fact, everything has always taken me longer (twice, sometimes three times as long) to fully understand, process, and retain, and research can be unforgiving to these traits. So while this acknowledgments section is a standard part of dissertations, I genuinely have so many people I need to thank from the bottom of my heart, because I likely would not be submitting my dissertation right now if it were not for such a strong support system.

To my advisors, Drs. Petra Klein and Elizabeth Smith, thank you for your guidance in getting me to the finish line. I can imagine the difficulty of advising someone with atypical thinking, and I thoroughly appreciate you both for being accommodating to my needs for success, be it allowing me record meetings or taking time outside of work hours to provide feedback on my work. Thank you also for always advocating for me through networking opportunities and letters of recommendation, and for believing in me, even when I couldn't believe in myself. As a Black woman navigating a space that can be isolating in graduate school even under ideal circumstances, you never stopped encouraging that I was someone more than capable of obtaining a STEM Ph.D. And, of course, thank you for jump-starting my pet-sitting business, which serves as a pretty stellar backup career. But I am in love with my current research associate job, and I

want to thank you for your flexibility as I navigate finishing this degree while starting a new full-time position in a foreign country. This is a thanks I wish to extend to my committee as well: I am extremely grateful to each and every one of you. And, of course, thank you to my boss, colleagues, and new friends here at Fraunhofer for also supporting me in this final stretch.

To my friends in this program, I am so appreciative to have met you. I have formed some core memories from all the game nights, work sessions, and hiking trips with so many in my amazing cohort. To Michelle and Maddy, I am so glad to have had you both along with me throughout this journey. I am already missing our girls' nights, Victoria's runs, and our many fun adventures like whitewater rafting! To the other special bonds I have formed in this program, thank you for always making me feel like I could enjoy the highs and be candid about the lows, even amid the severe imposter syndrome that has plagued me throughout. This comradery helped not only in pursuing the degree itself, but doing it under shaky times currently plaguing the world around us. It is a testament to our resilience that we have made it this far, and I'm proud of each and every one of you. To those who have already finished, you have my utmost congratulations — I look up to you, and I will continue cheerleading for you as you excel in whatever career you end up in. To those almost there who just need a little encouragement: I know you can do this. Chances are I have compared myself to you at some point, which is not healthy and I'm working on that! But it's also the the best way I can convey that I know you have what it takes.

I must also thank those outside the program who have encouraged me. To my hometown friends, I have never once worried about the bonds of our friendship breaking, even living all the way out here in Germany. I know quite a few people who still retain close connections to their high school friends, but I have never witnessed anyone else having such a strong, tight-knit, group maintain the special relationship

we all have. To Manny, Paige, Sal, Jodie, Jon, Whitney, Cody, and everyone else in our Garbsalia homies gang, thank you for your support as I journeyed graduate school these past several years. It's so heartwarming to know I have friends willing to fly halfway across the country, no questions asked, to celebrate my next step in life. It has been the utmost honor to grow into adulthood with you guys and extend that happiness to newer additions to the group. Thank you for your support, and I cannot wait for the many more memories to come. My family has also given me unmeasurable love and support. To my uncle, aunt, and cousins who allowed me to live with them while I was completing my master's, I am truly indebted to you in ways I can probably never repay as I would not be here without you. To my late grandmother who helped raise me in high school, I owe so much to you for helping instill a sense of independence and resilience that has carried me through this Ph.D. I miss you every day. And to my parents, thank you for always pushing me to pursue my goals, and thank you for understanding when I had to seclude myself from chatting to focus on work. I am so proud to say I am your daughter.

Finally to myself. You have battled a slew of physical and mental health that worsened throughout the course of this Ph.D., all of which was often neglected. I have not been kind to you throughout this process. There were many instances of fear and frustration that I didn't know how to push through without doubting or even hating you, and I am sorry that I didn't have more faith in you. The truth is, that's going to be something that's going to take a lot of learning even now. But as look over the finished product of my blood, sweat and tears that I created while beginning my career, I can now genuinely say that I am in awe of my abilities and am proud of myself. I vow here and now to take better care of me so that I can continue enjoying the passion that brought me here in the first place. Congratulations, Arianna, for getting to the final stages of such an amazing accomplishment. You are worthy.

Table of Contents

Acknowledgments iv

List of Tables ix

List of Figures xi

Abstract xviii

1 Introduction 1
1.1 The Atmospheric Boundary Layer 1
1.1.1 The Nocturnal Low-Level Jet 3
1.1.2 Atmospheric Boundary Layer Height 6
1.2 Previously Observed Wind Farms Effects 9
1.2.1 The American WAKE experimeNt 11
1.3 Proposed Research 13

2 Algorithms and Value-Added Data Product Evaluation 16
2.1 Instruments and Datasets 18
2.1.1 Observational Platforms 18
2.1.2 Standard Data Processing 20
2.1.3 Validation Field Datasets 22
2.2 Algorithms to Evaluate for ABL Characterization 26
2.2.1 Optimal Estimation Wind Retrieval (WINDoe) 26
2.2.2 The Fuzzy Logic ABL Height Algorithm 31
2.2.3 Validation Methodologies used during BLISS-FUL 35
2.3 Results: Performance, Sensitivity and Quality Control 45
2.3.1 WINDoe Performance Evaluation 45
2.3.2 Sensitivity of H_{FL} to Input Data 52
2.3.3 Fuzzy-Logic ABL Height Performance Evaluation 56
2.3.4 Identifying Mixing Signatures in ABL Lidar Profiles 72
2.4 Chapter Summary and Implications 78

3 Wind Farm Effects on Low-Level Mixing 81
3.1 Methods 83

3.1.1 Study Design and Scope 83
3.1.2 Instrument Configuration and Data Availability 86
3.1.3 Data Selection Criteria 91
3.2 Low-level Mixing Results 95
3.2.1 Initial Evidence of Wind Farm Mixing 95
3.2.2 NLLJ Considerations 101
3.2.3 Wind Threshold Method 110
3.3 Chapter Summary and Implications 117

4 Wind Farm Effects on ABL Height 121
4.1 Data and Methods 123
4.2 Results 126
4.3 Chapter Summary and Implications 139

5 Conclusions and Future Work 142

Appendix A 151

Appendix B 154

Reference List 157

List of Tables

1.1 Overview of common H estimation approaches and their approach to defining H. Definitions are separated by stability regime, including the physical basis of each definition, primary observational platforms, and practical considerations. 8

2.1 Summary of three campaigns for testing the optimal estimation wind algorithm and the fuzzy logic ABL height algorithm. 26

2.2 Summary of all seven radiosonde techniques along with a description of their function as an H indicator, strengths, and weaknesses as identified by past literature. 38

2.3 Weather conditions at each radiosonde launch time for the nine BLISSFUL cases of interest. For OUN radiosonde launches, all surface observations listed below come from the NWC Mesonet site. For KAEFS radiosonde launches, sky coverage data comes from the Automatic Surface Observing System (ASOS) at the Chickasha Municipal Airport in Chickasha, OK (42 km west of KAEFS; data available at `https://mesonet.agron.iastate.edu/request/download.phtml?network=OK_ASOS`). The cloud cover data was verified with GOES-16 visible satellite data. The rest of the data comes from the Washington, Oklahoma Mesonet station located at KAEFS. F.C. = 'few clouds', P.C. = 'partly cloudy', and M.C. = 'mostly cloudy.' Shaded row colors correspond to cases of interest for comparing H methods and their sky conditions (clear-sky = blue, few-partly cloudy = yellow, mostly-overcast = grey). 59

2.4 Overview of the radiosonde-based H (km) for the entire period and their detections in km from each of the seven techniques. The H_S and SD values are also listed. The * symbol indicates the techniques that match with H_S. SD refers to the standard deviation of the techniques. 60

3.1 The number of cases within each of the five NLLJ classes as categorized by Whiteman et al. (1997): "no NLLJ", "Class 0" corresponding to weak NLLJs, "Class 1" to moderate NLLJs, "Class 2" to strong NLLJs, and "Class 3" to very strong NLLJs. Going forward, these five regimes get further binned into 3 groups: weak-to-no NLLJs consisting of no NLLJ and class 0, moderate NLLJs consisting of class 1, and strong NLLJs. . 105

A.1 ARM-CF instrument configuration settings used across the analysis period. 152

A.2 CLAMPS instrument configuration settings used across the analysis period. 153

B.1 ZephIR-300 lidar configuration settings used during the Fall-Winter 2022 deployment. 154

List of Figures

1.1 Schematic of the idealized diurnal ABL (adapted from Stull (1988)). . . 2

1.2 Wind farms in the SGP (mainly Oklahoma, U.S) color coded by year they were constructed. Map retrieved from kepler.gl and wind turbine coordinate data from emp.lbl.gov. 12

2.1 Pictures of ARM-CF's lidar (Fig. 2.1a), ARM-CF's AERI (Fig. 2.1b), and the CLAMPS2 platform (Fig. 2.1c), along with zoom-in pictures of each instrument. Though only the CLAMPS2 trailer is shown here, CLAMPS1 mirrors its setup. The Fig. 2.1a, 2.1b, and 2.1c pictures were provided by Corydon Ireland at `https://asr.science.energy.gov/news/program-news/post/10247` and Gero and Hackel (2025), respectively, and the CLAMPS2 pictures were provided by NSSL at `https://apps.nssl.noaa.gov/CLAMPS/,respectively`. 19

2.2 Sample TROPoe profiles of T, θ, and q from CLAMPS1 (left column) and CLAMPS2 (right column) from 23 September 2023. 21

2.3 Map of field campaigns and observational instruments of interest beginning with the continental U.S (top left) and zooming into the north-central Oklahoma region (top middle). The sites at the bottom illustrate all stationary instrumentation sites or locations where campaigns took place, labeled based on the corresponding keys on the top right. Satellite imagery was obtained from Google Earth. 23

2.4 A comparison of VADs filtering at an SNR threshold of 0.008 from CLAMPS1 (Fig. 2.4a) and CLAMPS2 (Fig. 2.4c) with WINDoe retrievals from CLAMPS1 (Fig. 2.4b) and CLAMPS2 (Fig. 2.4d) for the case of 23 September 2023. White contours show WINDoe wind speed uncertainty in $\mathrm{m\,s^{-1}}$. 28

2.5 The classification metric for NLLJ magnitude (table) and the results of that classification applied to AWAKEN A1, CLAMPS1, and CLAMPS2 on 23 September 2023 (0005-15:15). In Figure 2.5a, each site showcases the results using different types of lidar data filtering: site A1 implemented a six-beam method with a dynamic filtering method, and both CLAMPS show VADs with the traditional SNR filtering at 0.008. These are compared with NLLJ classification results using the same data but retrieved via WINDoe (Figure 2.5b). 29

2.6 Time-height cross-sections of the variables considered in each step of the fuzzy-logic processing and their resulting H_{FL} outputs. Step 1 depicts profiles of mixing measurements (σ_w^2, high frequency σ_w^2, and inversion height) that help make up the first generation estimate, and step 2 shows profiles of mixing indicators (intensity, intensity variance, the u- and v-component ws, θ, and q) that help make up the second generation estimate. A more detailed diagram on each step can be found in Smith and Carlin (2024), specifically their Figure 4. 34

2.7 The seven radiosonde techniques as percentages of the H_S median (represented as the black horizontal line), separated by sky coverage conditions (Fig. 2.7a, 2.7b, and 2.7c represents clear-sky, few clouds-partly cloudy, and mostly cloudy-overcast, respectively). Within each sky condition category, a time window is applied for three different periods throughout the diurnal cycle to account for radiosondes not being released exactly on the hour. The number of samples (n) in each of these ranges is listed at the top left. 40

2.8 Scatterplots of ARM-CF and OU lidar VADs during LABLE I when the OU lidar was scanning two different elevation angles (40°; Fig. 2.8a, and 70°; Fig. 2.8b). The VADs were SNR-filtered at 0.008. The same is shown in Fig. 2.8c but for WINDoe, where the OU output was comprised of both the 40° and 70° elevation angles together. Results from four different range gates throughout the ABL are shown for all panels except Fig. 2.8c., which included a fifth measure at 10 m to demonstrate the abilities of its coverage. 46

2.9 Probability density functions of the ARM-CF lidar for WINDoe ws, its uncertainty, and the difference between VADs and WINDoe for a period of time in the SBL (Figs. 2.9a-2.9c) and the CBL (Figs. 2.9d-2.9f). . . 48

2.10 As in Figure 2.9, but for the OU lidar. Here, the difference was measured at both the 40° and 70° elevation angles. 49

2.11 Differences between H_{FL} using VAD- and WINDoe-derived wind profiles throughout the 0500-0500 UTC diurnal cycle for all BLISS-FUL cases. White areas indicate periods of missing data. 52

2.12 A comparison of second-generation aggregate values for the two clear-sky cases: 18 June 2021 is shown in the left column, and 22 June 2021 in the right column. Whether the input data has high- or low-resolution w or VAD data is detailed in the panel inserts as 'high-res" or "low-res". 55

2.13 The three main H estimation methods (H_S for the sounding method, H_R for the radar method, and H_{FL} for the fuzzy-logic method) under mainly clear sky conditions (18 June 2021 0500 UTC - 19 June 2021 0500 UTC for Fig. 2.13a and 22 June 2021 0500 UTC - 23 June 2021 0500 UTC for Fig. 2.13b). The H_R (green dashed line), and H_{FL} (dark blue line) methods are overlaid on CLAMPS1 w observations, a crucial contributor in the first generation aggregation of H_{FL}. All H_S results are shown with circle markers (filled for OUN and open for KAEFS), and the black vertical lines associated with them represent the standard deviation of the techniques applied. Local sunrise and sunset times are shown with vertical dashed lines. The start of any period clouds first appear over all sites were denoted at the top of the plot by the types of clouds they were. 61

2.14 Surface synoptic maps from NOAA's Weather Prediction Center for 18 June 2021 (top row) and 22 June 2021 (bottom row) at 0000, 1200, and 2100 UTC. 63

2.15 As in Figure 13, but for cases with few-partly cloudy conditions. 65

2.16 Radar imagery detailing the outflow from clustered thunderstorm cells near Pauls Valley, Oklahoma on 6 July 2021. 66

2.17 As in Fig. 2.13, but for cases with mostly cloudy-overcast conditions. . 68

2.18 Radar QVPs of Z_{DR} values using the same cases from Figure 2.17 (21 June 2021 for Fig. 2.17a and 26 June 2021 for Fig. 2.17b). Note the difference in the y-axis range compared to previous figures to view the extent of the detected H_R, though it does still exceed this larger range at times. 69

2.19 Map from Fig. 2.3 KAEFS and OU North Campus maps zoomed out in view to better view the surroundings of the two sites. 73

2.20 Time-height cross-section of CLAMPS1 and CLAMPS2 10-minute WINDoe-derived winds (Figs. 2.20a and 2.20b) and 10-minute σ_w with no SNR-filtering applied (Figs. 2.20c and 2.20d) during the PBLTops campaign on 25 August 2020. 74

2.21 PBLTops percentiles of σ_w throughout the full diurnal cycle for all available data (Fig. 2.21a), only southerly data (Fig. 2.21b), and only northwesterly data (Fig. 2.21c). The same approach is employed but only for the SBL (Figs. 2.21d-2.21f) and only for the CBL (Figs. 2.21g - 2.21i). The 50th percentile served as the mean measure, while the 25th and 75th percentile served as left and right outer bounds, respectively. To compare usable measurements not contaminated by noise, zoomed-in versions of each panel from a 0-3 $\mathrm{m\,s^{-1}}$ x-axis and 0.075-1.0 km y-axis are shown at the right of their original version, except for Fig. 2.21i where the data was not within the inset map bounds. 76

3.1 Satellite view of Oklahoma (top left; Google Earth) with a zoomed in version of the AWAKEN domain showing terrain elevation information (top right; Google Earth, with elevation information from OpenTopography and turbine latitudes and longitudes from the U.S. Wind Turbine Database). Marked locations represent AWAKEN observation sites referenced in this work. Locations of ZephIR 300 profiling lidars represent only the winter campaign, after which they were relocated elsewhere. Light gray symbols south of E36 mark turbines that were under construction and not yet operational during the deployment of CLAMPS and the profiling lidars. The bottom panels are further zoomed-in maps of the sites of interest for the study. 83

3.2 Time series of full ARM-CF lidar data 2011-2023 summer and fall-winter periods filtered for data quality. Each bar is representative of a single 24-hour case. 87

3.3 As in Figure 25 but for AWAKEN data. Only time ranges where data from both CLAMPS were available are shown. As with the ARM-CF data availability, each bar is representative of a single 24-hour case. . . 89

3.4 Root mean squared error of the ws between WINDoe and ZephIR data (Fig. 3.4a, solid lines) and the ZephIR and CLAMPS scanning lidar VAD retrievals (Fig. 3.4a, dotted lines) during the 2022 fall-winter campaign. Fig. 3.4b shows the same dataset comparisons but with mean bias calculations. WINDoe data were matched to the nearest ZephIR and VAD data heights. The ZephIR-VAD comparisons start at roughly 60 m where observations from the CLAMPS lidars begin. 92

3.5 Wind roses of using WINDoe data of the analysis periods of interest during the fall-winter and summer seasons from the ARM-CF lidar (Figs. 3.5a-3.5b) and the CLAMPS2 lidar. Only CLAMPS2 data from the far-field site is shown since, unlike CLAMPS1, had correct wd during the summer. 95

3.6 Polar plots containing rotor-layer averaged σ_w as a function of ws from all directions between 0000-1200 UTC. Blue outlines that appear on the polar region correspond to the sectors wind farms less than 10 km are located. Any ws below 3 $\mathrm{m\,s^{-1}}$ was discarded, aligning with the filtering rules that turbines are not expected to be operating below this threshold. All data available from each individual site is shown and there are not common timestamps between the sites. As in the wind roses, CLAMPS2 wd in the summer was used for the CLAMPS1 summer results. 97

3.7 Comparison of averaged σ_w levels between environments with and without nearby wind farms from the southerly sector between 0000-1200 UTC. Fig. 3.7a corresponds to the fall-winter periods from ARM-CF pre-farm (blue dashed line), ARM-CF post-farm (blue solid line), AWAKEN far-field (pink dashed line), and AWAKEN near-farm (pink solid line). Fig. 3.7b shows the same but during the summer periods. . 99

3.8 Hourly means showing NLLJ characteristics through maximum ws (Fig. 3.8a-b) and the altitude it occurs at (Fig. 3.8c-d) as measured by ARM-CF pre-farm (first column) and post-farm (second column). 102

3.9 As in Figure 3.8, but in place of ARM-CF pre-farm are results from AWAKEN far-field (first column), and in place of ARM-CF post-farm are results from AWAKEN near-farm (second column). 104

3.10 Profiles of ABL ws (Fig. 3.10a-d) and σ_w (Fig. 3.10e-h), and time-series of rotor-averaged σ_w (Fig. 3.10g) for a weak-to-no NLLJ case. Horizontal black dashed lines in the ws represent hub height, and the white dashed lines indicate the height of the rotor tip. 106

3.11 As in Fig. 3.10, but as composites for moderate NLLJ cases. 107

3.12 As in Fig. 3.10, but for composited strong NLLJ case. 108

3.13 Profiles of median σ_w from environments without nearby wind farms during the ARM-CF and AWAKEN fall-winter (Figs. 3.13a and 3.13c) and summer (Figs. 3.13b and 3.13d). The pink line denoting V_T as computed from B15. 112

3.14 The V_T from non-waked environments as calculated from ARM-CF and AWAKEN fall-winter (Figs. 3.14a and 3.14c) and ARM-CF and AWAKEN summer (Figs. 3.14b and 3.14d) at rotor layer heights (60, 85, 110, and 135 m). 114

3.15 Vertical percentiles of normalized σ_w starting at 75m from cases that only contained moderate NLLJs. The median, or 50th percentile, is plotted with outer bounds making up the the 25th and 75 percentiles. Individual profiles that made up the percentiles were shown as thin lines. Gaussian smoothing was applied to reduce noisy returns. The gray horizontal bar represents rotor layer heights. 116

4.1 Averages from second-generation output of H_{FL} runs for ARM-CF (pre-farm, dashed blue line; post-farm, solid blue line) and CLAMPS (far-field, dashed pink line; near-farm solid pink line) data from the summer periods. At the top right of the panel, the number of samples from each of the plotted averages is listed. 126

4.2 As in Fig. 4.1, but categorized by different NLLJ regimes: weak-to no (Fig. 4.2a), moderate (Fig. 4.2b), and strong (Fig. 4.2c). 127

4.3 Comparisons on 2023-08-17 between ARM-CF, near-farm, and far-field of four H methods: H_S (yellow star), H_{FL} (blue line), the turbulence-based method (white line), and the thermodynamic-based method (green line). Radiosondes originating from the ARM-CF site were displayed alongside with the three H methods from ARM-CF, and radiosondes originating from AWAKEN's site H were displayed with the near-farm and far-field H methods. 128

4.4 The same same 2023-08-17 case used in Fig. 4.3 for ARM-CF, CLAMPS1, and CLAMPS2 and their θ (first row), ws (second row), σ_w (third row), and the first and second generation H_{FL} along with second-generation mechanical- and buoyancy-based drivers (fourth row). 131

4.5 As in Fig. 4.4, but for the northerly case of 2023-08-30. 134

4.6 Outputs from the second-generation fuzzy-logic algorithm for ARM-CF (yellow line), near-farm (pink line), and far-field (blue line) on 2023-08-16 when turbines are not expected to be operating because rotor-layer winds were less than 3 $\mathrm{m\,s^{-1}}$ throughout the period. 137

B.1 Evaluation and combination of *ws* data from the ZephIR and CLAMPS lidars. The left column shows data from the near-field site, Rolling Meadows Golf Club (RMGC), collected by CLAMPS1 and Z773. The right column shows data from the far-field site of E36, collected by CLAMPS2 and Z345. Panels B.1a and B.1b show for each site, respectively, a scatterplot of winds at the measurement height closest to 180 m (exact for ZephIR, 183 m for CLAMPS) from the entire winter campaign. Panels B.1c and B.1d show a time series of winds at the same measurement heights on 2 November 2022 with error bars corresponding to the standard deviation of averaged ZephIR data. Finally, panels B.1e and B.1f are time-height cross sections of CLAMPS wind speed observations with wind barbs overlaid, also for 2 November 2022. Panels B.1g and B.1h, showing the ZephIR lidar wind speed observations in a similar way, are meant to combine with panels B.1e and B.1f above to demonstrate the two lidars as a complementary profile. 156

Abstract

Wind farms are steadily increasing around the world, and they will continue to grow in size and number as global efforts shift toward a carbon-neutral future harnessing more renewable energy. Previous observational studies found that the wakes wind farms produce can influence physical and meteorological processes in the atmospheric boundary layer (ABL). However, even high-resolution ABL measurements have data gaps that make the lower atmosphere difficult to characterize, leaving an incomplete picture of how wind farms can modulate it. As wind farms expand, it is essential to determine their implications on an ABL represented to the best ability that current tools can offer, providing knowledge on wind farm modifications that can aid in planning field studies, numerical modeling, and weather forecasting.

This dissertation analyzes the impacts of northern Oklahoma wind farms on ABL properties. These goals are accomplished using two newly developed algorithms geared toward improving ABL data analysis where limitations have traditionally existed: the first yields deeper ABL wind profiles using an optimal estimation approach, and the second estimates ABL depth throughout the full 24-hour cycle by compiling kinematic and thermodynamic profiles in a novel, synergistic framework. The wind retrieval algorithm increases coverage of ABL wind profiles, helping to resolve the full shape of northern Oklahoma's frequently occurring nocturnal low-level jet (NLLJ) even when the range of the collected wind data is too shallow to do so. In turn, this information helps accurately classify NLLJs of varying characteristics to identify any turbulence they produce that may coincide with wind farm mixing. The fuzzy-logic ABL height algorithm is then applied to determine whether such low-level mixing influences ABL depth and, by extension, the ABL as a whole.

Given the novel nature of these two algorithms, the first component of this dissertation examines their usability for wind farm research applications. This is done by testing their efficiency with past high-resolution field observations collected in northern and central Oklahoma prior to substantial wind farm development. The optimal estimation wind retrieval algorithm was found to adequately resolve ABL winds, including NLLJs that traditional retrieval methods cannot always completely resolve. The fuzzy-logic ABL height algorithm performed well provided recent precipitation had not depleted the aerosol content necessary for lidar observations. With both algorithms validated, the instruments used to measure wind farm effects were also evaluated and found to perform sufficiently in their kinematic and thermodynamic capabilities.

The second section identifies low-level mixing effects from wind farms during warm and cold months while accounting for other potential mixing sources in the region, namely the NLLJ. To do this analysis, environments with and without nearby wind farms were compared using 1) long-term datasets from a climate research site that has been active before and after the construction of a nearby wind farm, and 2) observations from a recent field campaign where one instrument platform was placed close to wind farms and another still located in the campaign domain but far from the suspected influence of wakes. Rotor-level mixing from both sets of comparisons was evident near wind farms, though it was often overshadowed by mixing from strong NLLJs. To account for this, we employ a method geared at determining the threshold wind speed at which near-surface turbulence develops. Identifying this threshold revealed that wind farm signals are most distinguishable under NLLJs of moderate strengths before mixing induced from the jet obscures wind-farm-driven mixing, affirming the presence of low-level wakes and the optimal periods for identifying them under NLLJ conditions.

Following the establishment of low-level mixing effects, it was necessary to determine if they extended throughout the rest of the ABL. The final component of this

dissertation examines this by applying the fuzzy-logic ABL height algorithm across all observations of interest. Doing so expands upon recent literature that also measured ABL height but using methods from individual instruments instead of a unification of datasets, which are prone to limitations associated with those individual methods that this fuzzy-logic height method helps mitigate. Consistent with low-level findings, the fuzzy-logic algorithm showed environments near wind farms to exhibit increased depth of the ABL. These findings agree with previous methods examining wind-farm-ABL interactions, but this first implementation of the fuzzy-logic ABL height approach for wind farm studies demonstrated that the method produces the most realistic estimates with reduced sensitivity compared to previously tested methods. Such effects were reinforced when testing different flow directions and occasions when turbines were not expected to be operational. These findings demonstrate that wind farms impact not only the low-levels, but the entire ABL, and the fuzzy-logic algorithm can accurately characterize these occurrences.

Chapter 1

Introduction

1.1 The Atmospheric Boundary Layer

The atmospheric boundary layer (ABL) encompasses the lowest few kilometers (km) of the atmosphere directly influenced by and coupled with Earth's surface. It is characterized by rapid exchanges of heat, momentum, and mass that spatially and temporally shape the temperature (T), wind speed (ws), and moisture distribution in the atmosphere (Stull, 1988; Garratt, 1994; Grant, 1997; Wallace and Hobbs, 2006). The evolution of the ABL over land differs depending on time in the diurnal cycle. During the daytime, solar heating from the Sun warms the Earth's surface, and that heat can be retained in the ground or transferred to the atmosphere through turbulent sensible and latent heat fluxes. The turbulent fluxes interact with the ABL on timescales that ranges from minutes to hours (Garratt and Brost, 1981) and create vertical turbulent motions. This well-mixed layer, also called the convective boundary layer (CBL), expands to roughly 1–3 km above ground level (AGL), where unstable conditions prevail. The growth of this CBL is generally proportional to the strength of vertical mixing and is also controlled by the entrainment of air from the free atmosphere.

After sunset, radiative cooling of the surface drastically alters the ABL structure and mechanisms. Stable conditions dominate, and the mixing driven by daytime heating weakens, giving way to mainly mechanically-driven turbulence. The preceding

day's mixed layer detaches from the surface and forms what is known as the residual layer. Radiative cooling near the surface induces T inversions (Acevedo and Fitzjarrald, 2001), which are particularly prominent under strongly stable ABL conditions (SBL), such as clear winter nights, in polar regions, or during solar eclipses (e.g., Belmont, 1957; Bradley et al., 1993; Seidel et al., 2010). The SBL makes up the layer below the inversion, which is substantially shallower than the CBL at only a few hundred meters. It is not until sunrise, when thermally-driven mixing returns, that the inversion dissipates and ABL gradually expands again. A depiction of the full diurnal cycle of an idealized ABL was composed by Stull (1988), which is replicated in Figure 1.1.

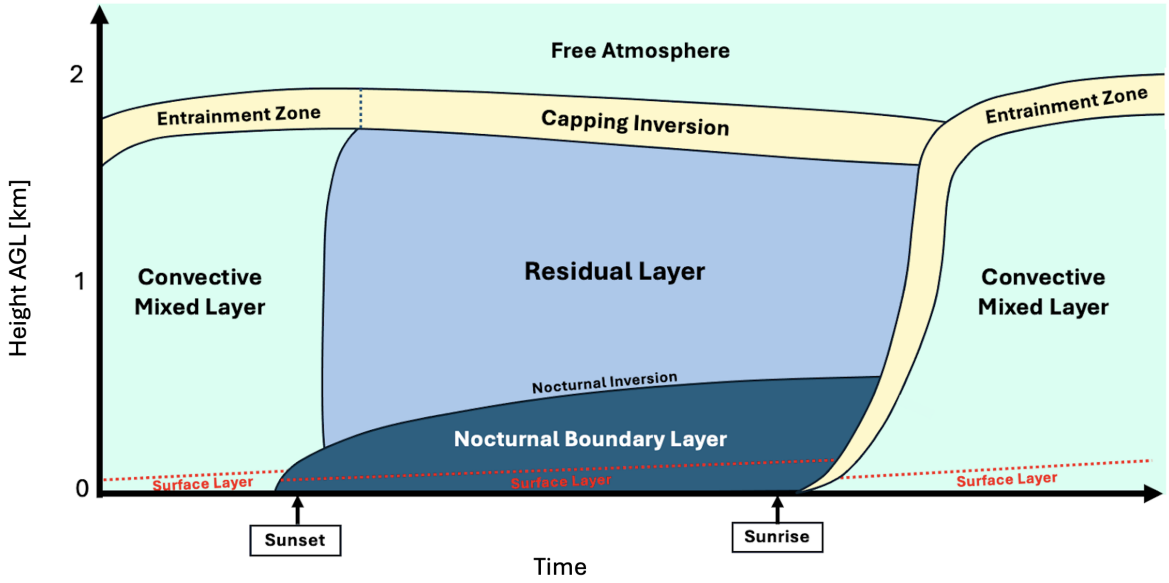


Figure 1.1: Schematic of the idealized diurnal ABL (adapted from Stull (1988)).

The ABL is a critical region to study because it contains important processes necessary for advancing research, forecasting, and numerical weather prediction that is important for saving lives and property. These processes include mechanisms that are small-scale (e.g., Garratt, 1993; Santanello et al., 2007; Krishnamurthy et al., 2021b) and mesoscale, such as precipitation and convective systems (e.g., Zhang, 2003; Bony et al., 2015; Lamraoui et al., 2019). Additionally, the ABL governs air quality, is

influenced by the surface energy balance, and hosts a variety of weather phenomena that directly impact humans and other life forms. In fact, humans and industrial production introduces additional anthropogenic complexities that can further complicate ABL dynamics, such as urbanization, greenhouse gas emissions, agricultural practices, and wind energy (e.g., Han et al., 2009; Vajda et al., 2011; Peña et al., 2016).

Wind farms, in particular, are known to produce wakes, where the rotating blades extract kinetic energy from the wind leading to the production of turbulent flow downstream (Tennekes and Lumley, 1972; Lissaman, 1979). These wakes have significant implications for local ABL characteristics, particularly under stable atmospheric conditions when they are most pronounced (Machefaux et al., 2016; Bodini et al., 2017). Despite investigations around the world geared towards studying these wind farm wakes on the ABL, the nature and extent of their influence remains poorly understood, largely due to the challenge of obtaining adequate observational data. With wind farms quickly expanding worldwide, there is growing interest in studying how they interact with the local atmosphere. To this end, Banta et al. (2013) emphasized the need for high-resolution observations capable of measuring low heights within the rotor sweep area while concurrently resolving meteorological phenomena deep within the ABL. Such observations enable reliable quantification of wind farm effects on the ABL that are separate from other predominant ABL features like a major wind resource known as the nocturnal low-level jet (NLLJ). The NLLJ and another important ABL characteristic, ABL height (H), will be discussed further before more details about wind farms are presented in Section 1.2.

1.1.1 The Nocturnal Low-Level Jet

The NLLJ is a phenomenon characterized by a well-defined, overnight wind maxima concentrated in the lower ABL (e.g., Bonner, 1968; Mitchell et al., 1995; Whiteman

et al., 1997; Rife et al., 2010). The wind usually peaks in the early morning hours, where the area of strongest ws is referred to as the 'NLLJ nose,' before dissipating around dawn (Shapiro and Fedorovich, 2010). NLLJs commonly occur within the first km above the surface, often below 500 m. Aside from those standard characteristics, though, the intensity, height, and duration of the NLLJ can all vary depending on seasonality, atmospheric conditions, and geographic location.

In the U.S Southern Great Plains (SGP), NLLJs are especially prevalent and intense, observed in approximately 63% of overnight periods annually (Song et al., 2005). Why this is the case remains an active area of ABL research, but there are a few highly regarded theories: 1) inertial oscillation driven by reduced frictional forcing after sunset (Blackadar, 1957; Parish et al., 1988; Parish, 2000; Zhong et al., 1996; Shapiro and Fedorovich, 2010); 2) terrain-induced gradients in pressure, T, and ws caused by elevation differences between the Rocky Mountains and adjacent Plains (Holton, 1967; Parish, 2017; Fedorovich et al., 2017); and 3) buoyancy influencing the NLLJ in time and space or inducing baroclinic zones (Shapiro et al., 2022; Smith et al., 2019; Gebauer et al., 2018; Shapiro et al., 2022; Gomes et al., 2025). Though NLLJs have been reported in many parts of the world, this dissertation focuses solely on those that occur in the SGP. Given the dominant role of NLLJs in this region, they must be considered to accurately characterize the region's ABL.

SGP NLLJs are often southerly in wind direction (wd), allowing them to advect moisture from the Gulf of Mexico and sustain convection to support severe weather; their dynamical and thermodynamic modulation of the lower ABL are suggested to also initiate convection (Pitchford and London, 1962; Astling et al., 1985; Trier et al., 2006; Shapiro and Fedorovich, 2010; Fedorovich et al., 2017; Gebauer et al., 2018; Carroll et al., 2019; Smith et al., 2019; Shapiro et al., 2022). They can even redistribute air pollutants (Klein et al., 2014), impact urban heat island intensities (Hu et al.,

2013), and intensify wildfires when mixed down toward the surface (Lindley et al., 2019). Additionally, the NLLJ has been found in numerous studies to alter the vertical structure of momentum and turbulence (e.g., Mahrt, 1999; Banta et al., 2002, 2006; Bonin et al., 2015).

From an observational perspective, field campaigns collecting high-quality measurements have been conducted in and around the SGP where the NLLJ could be extensively studied, such as with IHOP_2002 (Weckwerth et al., 2004), CASES-99 (Poulos et al., 2002), LABLE (Klein et al., 2015), and PECAN (Geerts et al., 2017). Ground-based remote-sensing instruments, such as Doppler scanning lidars, have been widely used to obtain detailed wind profiles in time and height showcasing the NLLJ. However, the depth of these profiles depends on how much aerosol content the lidar laser can scatter off, which weakens with altitude. The signal can also become distorted from other targets (such as precipitation or large particulate matter), which yields instrument noise in the data. Many methods are available to filter these noisy signals, including traditional fixed SNR thresholds and the more adaptive dynamic filtering approach (Beck and Kühn, 2017), but both remain limited to heights where sufficient backscatter exists. In other words, data containing NLLJ information can still be lost when the jet extends above the lidar's effective range regardless of the filtering strategy applied. This is a particularly concerning matter for relatively high-altitude NLLJs, which are common in colder months (Krishnamurthy et al., 2021b). On the same token, adequate Doppler scanning lidar datasets often used to measure NLLJs do not begin until after the first few range gates, leaving gaps in information near the surface necessary for wind farm analysis. In order to delineate between NLLJ and wind farm effects, it is necessary to have reliable coverage of wind profiles that cover the turbine wake spread while also fully encompassing NLLJ events that occur in this region. Since both features can influence turbulence properties, and because the growth of the ABL

is generally highly dependent on vertical mixing, insight on where near-surface mixing originates is needed to determine if wind farms impacts extend even to the top of the ABL.

1.1.2 Atmospheric Boundary Layer Height

The ABL depth, H, serves as a useful representative for the whole boundary layer, as it is directly proportional to the mixing and thermodynamic processes happening throughout it. Accurately characterizing H is important for applications in meteorology and related fields. For example, understanding and predicting the transport of pollutants depends on H (e.g., Beniston et al., 2017; Sørensen et al., 1996; Seaman and Michelson, 2000; Seibert et al., 2000; Wang and Wang, 2014; Yassin et al., 2018) and numerical models apply estimated H to compute turbulent mixing and chemical transport.

However, researchers rely on various methods to define and estimate H. The most direct approach is with in-situ measurements, such as those from radiosondes, which have been analyzed in local settings (e.g., Hennemuth and Lammert, 2006; Basha and Ratnam, 2009; Sawyer and Li, 2013), across the U.S. (e.g., Holzworth, 1964, 1967; Hicks et al., 2019), and on global scales (e.g., Seidel et al., 2024; Guo et al., 2024). However, there are several radiosonde techniques from which to choose that all carry their own strengths and limitations. Moreover, the high costs associated with radiosondes restricts their launch frequency, which is typically only twice a day operationally from the National Weather Service (NWS), resulting in a discontinuous temporal representation of the ABL. The Atmospheric Radiation Measurement Southern Great Plains (ARM-SGP) releases radiosondes four times daily at their main research hub in Billings, Oklahoma, and field experiments in the area may launch them even more often, but even this is not enough to fully represent ABL evolution or resolve important

ABL properties.

To address this temporal gap, continuously-collected data from ground-based remote-sensing platforms are available. Still, these methods are also not free from limitations. For example, radar wind profilers (Weber et al., 1993; Bianco and Wilczak, 2002; Turner et al., 2014b) perform well under cloud-free conditions, though their vertical resolution can be relatively coarse. Radio acoustic sounding systems (RASS) and sodars use acoustic pulses to gather information on wind, T and turbulent structures, but they are limited in vertical extent and simultaneously sensitive to ambient T and ws gradients (Beyrich, 1997). Ceilometers, which measure aerosol backscatter content, yield favorable results when compared with radiosonde-derived heights, but using backscatter gradients alone presents difficulty at night differentiating between the SBL and residual layers (Gierens et al., 2019; Zhang et al., 2022). Researchers have also used weather radars to identify Bragg scattering at and around H (Melnikov et al., 2013; Banghoff et al., 2018), though identifying the most ideal filtering conditions that serve as inputs continue to be a work of progress.

Thermodynamic profiles can also be useful for H estimation. Microwave radiometers (MWR; Solheim et al. (1998); Rose et al. (2005)) and atmospheric emitted radiance interferometers (AERI; Knuteson et al. (2004a,b)) have been sources of retrieved T, potential temperature (θ), and water vapor mixing ratio (q) profiles (retrieval method discussed further in Chapter 2) for H analysis based on gradients and inversions (Ye et al., 2022; Abraham et al., 2025). Summa et al. (2013) and Turner et al. (2014a) also assessed q from Raman lidars. Regardless, the θ can be difficult for identifying H if inversions are weak or gradients are ambiguous. Also, gradient-based estimation only infers H rather than directly measuring it. On the other hand, Doppler scanning lidars can directly observe turbulence-based characteristics using laser technology to detect aerosol motion at a high temporal resolution, making them a popular tool for

Table 1.1: Overview of common H estimation approaches and their approach to defining H. Definitions are separated by stability regime, including the physical basis of each definition, primary observational platforms, and practical considerations.

Method	**Regime**	**Platform(s)**	**Physical Basis**
Top of surface inversion	SBL	Radiosondes	H at the top of the surface-based temperature inversion, characteristic of stable stratification
Richardson number threshold	CBL & SBL	Radiosondes; numerical weather prediction models	H where bulk or gradient Richardson number exceeds a critical value, indicating the suppression of turbulence
Acoustic pulses	CBL & SBL	RASS; sodar	Acoustic pulses used to retrieve temperature, wind speed, and turbulent structure profiles; H inferred from transitions in these profiles
Thermodynamic gradient methods	CBL & SBL	Radiosondes, MWR, AERI	H defined at characteristic gradients in potential temperature, relative humidity, or water vapor mixing ratio profiles
Minimum sensible heat flux	CBL	Flux tower arrays; large eddy simulations	H defined at the level of minimum (most negative) kinematic heat flux
Capping inversion or maximum potential temperature gradient	CBL	Radiosondes, MWR, AERI	H at the base of the temperature inversion capping the mixed layer, often coinciding with the maximum vertical gradient of potential temperature
Parcel method	CBL	Radiosondes	H where virtual potential temperature equals (or slightly exceeds) its surface value, analogous to a lifted parcel reaching neutral buoyancy
Vertical velocity variance or turbulent kinetic energy threshold	CBL	Doppler lidar (vertical stares)	H at the level where turbulent kinetic energy or vertical velocity variance falls below a prescribed threshold, marking the top of the turbulent layer
Radar wind profiler	CBL	Radar wind profiler	H inferred from sharp gradient in radar reflectivity or signal-to-noise ratio associated with the capping inversion
Aerosol backscatter gradient	CBL	Ceilometer, Doppler lidar	H identified at the sharp decrease in aerosol concentration that often coincides with the top of the mixed layer
Radar Bragg scatter minimum	CBL	Dual polarization radar	Refractive index fluctuations at the top of the CBL produce enhanced radar backscatter detectable with dual-polarization radar

H estimation. Typical approaches using these instruments to quantify H are where the variance of vertical velocity falls below a certain threshold (Lenschow et al., 2000; Tucker et al., 2009; Lenschow et al., 2012; Berg et al., 2017; Krishnamurthy et al., 2021a). Unfortunately, approximating turbulence becomes difficult in the presence of persistent stable stratification, and studies utilizing Doppler lidar data tend not to include nighttime when thermally-driven mixing is greatly reduced. In fact, several H estimation methods fall victim to uncertain measurements during the SBL. This can be seen in Table 1.1 which lists these methods and their specific approach to defining H, many of which can only operate well in the CBL (Tucker et al., 2009).

Many studies have examined some of these observational methods simultaneously (e.g., Emeis et al., 2012; Collaud Coen et al., 2014; Caicedo et al., 2017; de Arruda Moreira et al., 2018; Duncan Jr. et al., 2022; Abraham et al., 2025), which were useful for highlighting the pros and cons of each method and the uncertainties involved in comparing different remote-sensing data sources. Kotthaus et al. (2023) suggests taking this approach a step further with a combination, or "synergy", of different H schemes that leverages the strengths of each instrument while the weaknesses are compensated by other datastreams, but this has yet to be accomplished for wind farm analysis. A robust representation of H and its evolution would assist in identifying wind farm influences on the entire ABL, particularly if such a method efficiently estimates H in the nighttime hours when turbine wakes are most detectable.

1.2 Previously Observed Wind Farms Effects

Wind farms consist of dozens to hundreds of wind turbines designed to harness wind energy for electricity generation, providing a more sustainable alternative to fossil fuel burning. The increase in size and density of both onshore and offshore wind farms

worldwide have made them a subject of interest in meteorology due to their interactions with the surrounding atmosphere. Our understanding of these interactions has been built through a combination of wind tunnel experiments (Chamorro and Porté-Agel, 2009; Porté-Agel et al., 2011; Aubrun et al., 2013; Hancock and Pascheke, 2014; Hyvärinen and Segalini, 2018; Fleming et al., 2019; Neunaber et al., 2021; Campagnolo et al., 2022; Hancock and Hayden, 2024) and numerical simulations (Barthelmie et al., 2007; Calaf et al., 2010, 2011; Chamorro et al., 2012; Churchfield et al., 2012; Yang et al., 2015; Draper et al., 2016; Stevens et al., 2018; Larsén and Fischereit, 2021; Stanislawski et al., 2023; Vahidi and Porté-Agel, 2024), including high-resolution modeling provided by large-eddy simulations that are ideal for analyzing small-scale turbulent flow (Calaf et al., 2010, 2011; Wu and Porté-Agel, 2012; Abkar and Porté-Agel, 2013; Keck et al., 2014a,b; Mehta et al., 2014; Abkar et al., 2016; Allaerts and Meyers, 2019; Ghobrial et al., 2025).

While these studies have provided valuable information about the wind farm impacts from an idealized framework, it is ultimately through real-world observations that researchers can gain the most direct understanding of wind farm impacts on the ABL, as field observations capture the full complexity of atmospheric conditions that controlled experiments and simulations cannot fully replicate. Such observational efforts have shown that wind farms modify surface T (Baidya Roy and Traiteur, 2010; Zhou et al., 2012; Smith et al., 2013; Siedersleben et al., 2018), surface heat and momentum fluxes (Rajewski et al. 2013; 2014), and produce turbulent wakes that can extend for several kilometers downstream (Christiansen and Hasager, 2005; Wharton and Lundquist, 2011; Hirth et al., 2013; Banta et al., 2015; Krishnamurthy et al., 2017; Cañadillas et al., 2019; Fernando et al., 2019a; Ahsbahs et al., 2020; Zhan et al., 2020; Hereon, 2021; Hirth et al., 2021). Under stable stratification, studies identified wakes extending over 50 km offshore (Platis et al., 2018; Lundquist et al., 2019; Schneemann

et al., 2020). Porté-Agel et al. (2020) offers a comprehensive list of these studies and others geared at understanding wind-farm-atmosphere interactions.

Despite this breadth of prior work, observational studies are sparse in the SGP, as most wind farms were constructed after the 2010s (Figure 1.2). However, the region offers a wealth of long-term observations both before and after widespread wind farm development, enabling a direct comparison of pre- and post-farm atmospheric conditions. Additionally, the northern Oklahoma area recently hosted a field campaign with a dedicated network of instruments specifically targeting wind farm-ABL interactions, further expanding the the region's observational record in and around wind farms.

1.2.1 The American WAKE experimeNt

The American WAKE experimeNt (AWAKEN; (Moriarty et al., 2020; Debnath et al., 2022; Moriarty et al., 2024)) was launched between 2022–2024 to address critical gaps in understanding wind-farm-atmosphere interactions. Led by the National Renewable Energy Laboratory (NREL), AWAKEN was a large-scale field campaign in northern Oklahoma, U.S. with collaborations between several government research institutions, universities, and national laboratories. The observational capabilities used during the campaign included Doppler lidars, meteorological stations, MWRs, and infrared spectrometers positioned in, around, and far from wind farms collecting high-resolution ABL profiles. The deployment location was beneficial for examining wind farm effects in conjunction with the NLLJ prevalent without complex terrain features. Also, the AWAKEN domain contained additional instrument measurement capabilities provided by the ARM-SGP's Central Facility (ARM-CF; (Sisterson et al., 2016)) and many ARM-SGP extended sites, which have been continuously collecting ABL observations since the early 1990s (Atmospheric Radiation Measurement (ARM) Climate Research Facility, 2022) using much of the same type of instrumentation deployed for AWAKEN.

More information about AWAKEN is provided later in Section 2.1.

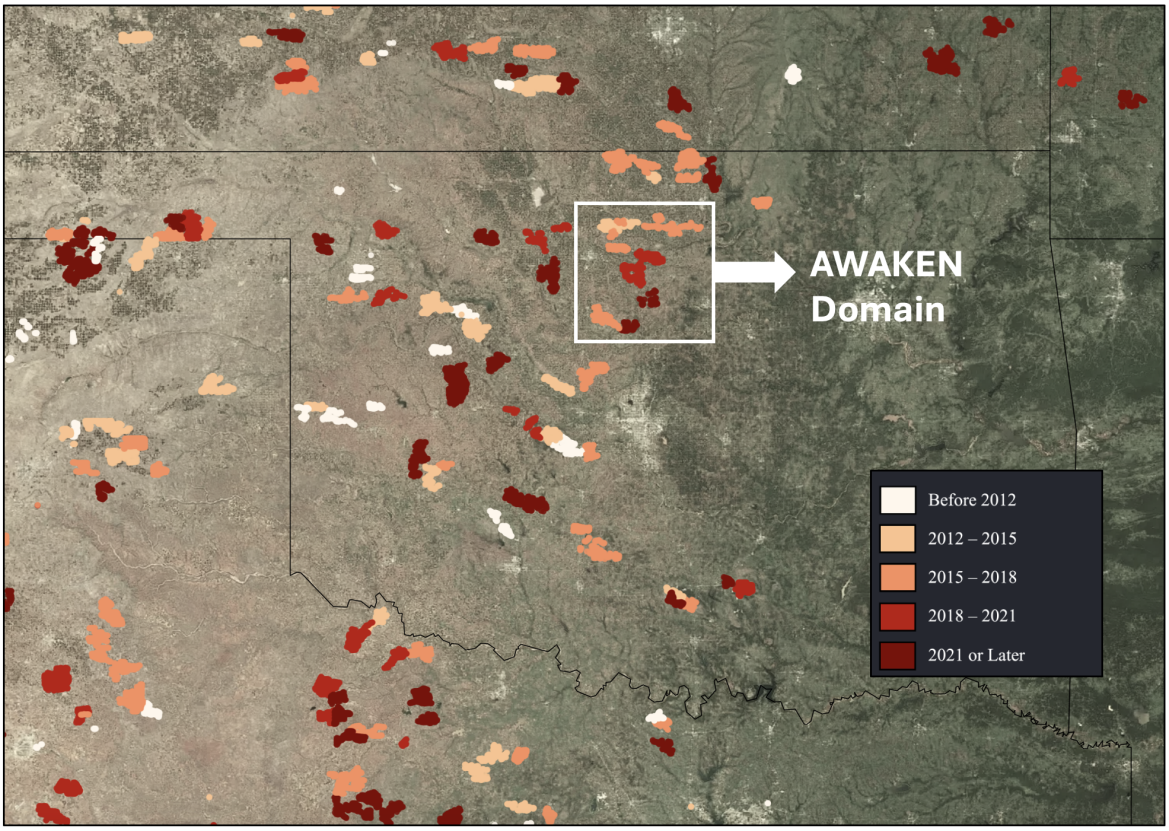


Figure 1.2: Wind farms in the SGP (mainly Oklahoma, U.S) color coded by year they were constructed. Map retrieved from kepler.gl and wind turbine coordinate data from emp.lbl.gov.

Findings on wind farm impacts using these instruments are emerging, but continue to necessitate additional insight. For example, Bodini et al. (2021) used ARM-CF data after the installation of a wind farm to the south to find it enhanced turbulent kinetic energy up to 30% and caused a ws deficit aloft. However, the eight-year observations were not separated by different NLLJ strengths, warranting a further investigation into how varying NLLJ characteristics could impede measuring wake effects from nearby wind farms. In addition, Abraham et al. (2025) found H during stable ABL periods (SBL) to increase downstream of wind farms by using traditional thermodynamic and turbulence-based H methods. That said, there were apparent differences in H at times

due to limitations in observational capabilities that befell the methods at different times, and resolving such instances would strengthen the findings.

As information on wind farm impacts in the SGP grows, several promising avenues to increase knowledge of their impacts on the ABL remain unexplored. Recently developed algorithms offer new capabilities for advancing ABL studies. One uses climatological information and an optimal estimation framework that can integrate data from multiple sources (Gebauer and Bell, 2024) to expand ABL wind profiles beyond the vertical limits imposed by lidar signal degradation, fully depicting upper-level properties like the NLLJ. The other ingests kinematic and thermodynamic datastreams from multiple remote-sensing instruments to estimate the H during both day and night using a fuzzy-logic approach (Smith and Carlin, 2024), which can be used to provide additional insight to Abraham et al. (2025). The optimal estimation wind retrieval algorithm and the fuzzy-logic ABL height algorithm can be applied to both AWAKEN and ARM observations, where the latter provides several years of available data from before and after wind farms were built nearby. These algorithms offer a unique opportunity to enhance the measuring capabilities and support long-term assessments of wind farm impacts on ABL structure and evolution. Both algorithms are described and evaluated in Chapter 2.

1.3 Proposed Research

This dissertation seeks to improve understanding of how wind farms in northern Oklahoma may influence the ABL using the advanced observational and algorithmic capabilities recently made available. While previous studies around the region have explored low-level mixing prior to wind farm development (Bonin et al., 2015), compared those non-wind-farm regimes to post-wind-farm environments (Bodini et al., 2021), and in-

vestigated wind farm effects on ABL components Abraham et al. (2025), this analysis is the first to apply the two newly-developed algorithms that extend ABL wind and H information towards improving those analyses. This is achieved using two systematic approaches for comparing environments with and without nearby wind farms: first, two ground-based remote-sensing platforms from the University of Oklahoma (OU) and the National Severe Storms Laboratory (NSSL) were deployed during AWAKEN at sites near and far from wind farms. Second, long-term ARM-CF datasets were collected, spanning years of pre- and post-construction of a wind farm to the south of the site for longer comparisons than AWAKEN could provide. With these approaches, this research seeks to address how wind-farm developments influence important ABL characteristics in northern Oklahoma. To meet this goal we investigate the following questions:

- Can novel algorithms integrating high-resolution observations accurately resolve important ABL characteristics that are important to studying wind farm effects, such as the NLLJ and H?
- To what extent does the intensity of the NLLJ act as a limiting factor in the isolation and identification of wind-farm-induced turbulence?
- Can H derived from a new fuzzy-logic height estimation approach serve as a proxy for identifying wind-farm effects on the ABL?

The following work first examines the algorithms based on extending wind profiles (Gebauer and Bell, 2024) and H estimation (Smith and Carlin, 2024) by applying them to field campaign data to assess their accuracy for AWAKEN and ARM-CF applications; this is done by incorporating results from Jordan et al. (2024) in Chapter 2. Once validated, the optimal estimation wind retrieval algorithm is applied to compare

meteorological variables at rotor-disk heights between environments nearby wind farms with locations far from them, while assessing the external influence of the prominent NLLJ (Chapter 3). Finally, the meteorological variables throughout the full ABL are analyzed, culminating in a focused evaluation of H variability across wind-farm and non-wind-farm environments using the fuzzy-logic ABL height algorithm (Chapter 4). The conclusions and future prospects of this study are discussed in Chapter 5.

Chapter 2

Algorithms and Value-Added Data Product Evaluation

The first research question focuses on expanding observational capabilities of the ABL to better characterize its features and improve investigations of wind farm impacts. In the SGP, NLLJs are an important consideration for wind farm studies, as their variability in strength, height, and vertical structure carries direct implications for wind farm-induced mixing. For instance, one of the goals of this work is to classify NLLJs by magnitude and assess the low-level mixing wind farms generate within each regime. Doppler scanning lidars can offer insight into NLLJ strength as they continuously sample well into the ABL to produce deep, representative wind profiles, but adequate lidar measurements are dependent on the range of aerosol backscatter. If NLLJs occur above this range, their full structure cannot be resolved and effectively classifying the NLLJ by magnitude becomes less reliable. To address this limitation, a flexible optimal estimation wind retrieval algorithm is evaluated, which combines direct observations with climatological background information to fill gaps in the wind profile (Gebauer and Bell, 2024). The resulting extended coverage of wind speed and direction should enable accurate NLLJ classification, including for elevated jets that reach their ws maximum above the lidar's range, but the new wind retrieval algorithm requires further validation to confirm it can be applied for analyzing the NLLJ.

Another major goal of this dissertation is to determine whether low-level mixing occurring near wind farms deepens the ABL, which can be done by estimating H at different sites. Despite the many methods available to estimate H, most carry with them limitations that complicate studying wind farm effects on H, such as deficiencies in estimating H in the SBL when wind farm wakes are strongest, limited temporal coverage that hinders observation of wake evolution, or limitations tied to the choice of observing platform (Kotthaus et al., 2023). A new fuzzy-logic algorithm addresses several of these shortcomings by incorporating multiple data streams from ground-based remote-sensing instruments, integrating kinematic and thermodynamic variables to produce a robust estimate of H (Smith and Carlin, 2024). This synergistic approach enables continuous H estimation through the full, 24-hour diurnal cycle, including the SBL. However, given the algorithm's novelty, its performance, especially across varying environmental conditions in the SGP, requires evaluation.

To this end, the optimal estimation wind retrieval algorithm and fuzzy-logic H-estimation algorithm were tested on past field datasets from multiple ground-based remote sensing instruments—the same platforms that go on to be used for the desired wind farm analysis. These instruments were stationed in the north-central Oklahoma region for many past field campaigns prior to widespread wind farm development, enabling testing of the datasets they collected before wake effects are analyzed. The capacity of ABL profiles to resolve fine-scale mechanical mixing that could mimic wind-farm-driven turbulence is also assessed, as distinguishing such signals will be critical for interpreting results in the wind farm environment. Understanding the behavior of the algorithms and testing the accuracy of the datasets they ingest provides a baseline reference of how both operate which can be referenced for the wind farm analysis to follow.

2.1 Instruments and Datasets

2.1.1 Observational Platforms

The U.S. Department of Energy's ARM-SGP network consists of several fixed instrument sites throughout Oklahoma and Kansas. It was first established in 1992 with the intent to provide publicly available long-term in-situ and ground-based remote-sensing data for the atmospheric science community (Turner and Ellingson, 2016). The main principal site is the ARM-CF, which is located in the rural, pasture setting of Billings, Oklahoma. It is the most heavily instrumented of the ARM-SGP network; particularly relevant for this work are two of these instruments with measurements dating back to the early 2010s: a Halo Photonics Streamline Doppler scanning lidar as described in Pearson et al. (2009) (Fig. 2.1a) and an atmospheric emitted radiance interferometer, or AERI (Fig. 2.1b; Gero and Hackel (2025)). Bodini et al. (2021) leveraged the stationary deployment of these single-point instruments to compare turbulent kinetic energy before and after the construction of a nearby wind farm. The algorithms evaluated here extend that work by characterizing wind farm mixing across different NLLJ regimes and estimating H with a novel method.

About 177 km south of ARM-CF sits the National Weather Center (NWC) in Norman, Oklahoma, which houses entities including the NSSL, the National Weather Service (NWS) office for Norman (OUN), and OU's School of Meteorology. Among its research groups is the Boundary Layer Integrated Sensing and Simulation (BLISS) group, which coordinates ABL research and education among researchers, professors, and students (Klein et al., 2015). BLISS operates the Collaborative Lower Atmospheric Mobile Profiling System (CLAMPS; (Wagner et al., 2019)), a trailer-based instrument suite combining a Halo Doppler scanning lidar, an AERI, and an MWR. Two such



Figure 2.1: Pictures of ARM-CF's lidar (Fig. 2.1a), ARM-CF's AERI (Fig. 2.1b), and the CLAMPS2 platform (Fig. 2.1c), along with zoom-in pictures of each instrument. Though only the CLAMPS2 trailer is shown here, CLAMPS1 mirrors its setup. The Fig. 2.1a, 2.1b, and 2.1c pictures were provided by Corydon Ireland at `https://asr.science.energy.gov/news/program-news/post/10247` and Gero and Hackel (2025), respectively, and the CLAMPS2 pictures were provided by NSSL at `https://apps.nssl.noaa.gov/CLAMPS/`,respectively.

systems exist (CLAMPS1 and CLAMPS2) which, despite minor instrument model differences, are intended to operate as sibling platforms with instrumentation and data formatting as closely matched as possible (the instrument setup of the trailer is pictured in Fig. 2.1c). The CLAMPS systems have been deployed individually and in tandem across several field campaigns, including PECAN (Geerts et al., 2017; Gebauer et al., 2018; Smith et al., 2019), Perdigão (Fernando et al., 2019b; Wildmann et al., 2019; Bell et al., 2020), and LAPSE-RATE (Bell et al., 2021). In AWAKEN, deploying one CLAMPS near wind farms and the other far outside the suspected path of wakes enables paired, simultaneous comparisons between impacted and not impacted environments, which is a capability that ARM-CF's pre- and post-construction framework alone cannot provide.

2.1.2 Standard Data Processing

The ARM-CF and CLAMPS Doppler scanning lidars all offer wind measurements primarily through conical plan-position indicator (PPI) scans, though other scan strategies are possible depending on research interests (e.g., the six-beam technique from Sathe et al., 2015; Newman et al., 2016). The PPIs can be later post-processed as retrievals with ws and wd information in time and height, most often with the velocity azimuth display (VAD; Browning and Wexler (1968)) technique, but retrievals from the optimal estimation wind and fuzzy-logic H algorithm can also be tested here. The lidars can also provide observations of vertical velocity (w) when the lidar laser points straight up, which can then be post-processed into vertical velocity variance (σ_w) to directly study turbulent mixing.

In addition to the wind and turbulence information, the thermodynamics retrievals from the AERI or MWR provide time-height profiles, such as T, θ, and q useful for considering wind-farm impacts on the ABL. The Tropospheric Remotely Observed Pro-

filing via Optimal Estimation, or TROPoe (Turner and Löhnert, 2014, 2021; Turner and Blumberg, 2019) was developed as an algorithm to retrieve profiles of T and q via optimal estimation (Rodgers, 2000; Maahn et al., 2020), configurable through a straightforward variable input parameter (VIP) file. The approach assimilates combinations of observations with a climatological prior (typically several years of radiosonde information) and feeds this information into a forward model to iteratively compute thermodynamic profiles spanning deep into the ABL.

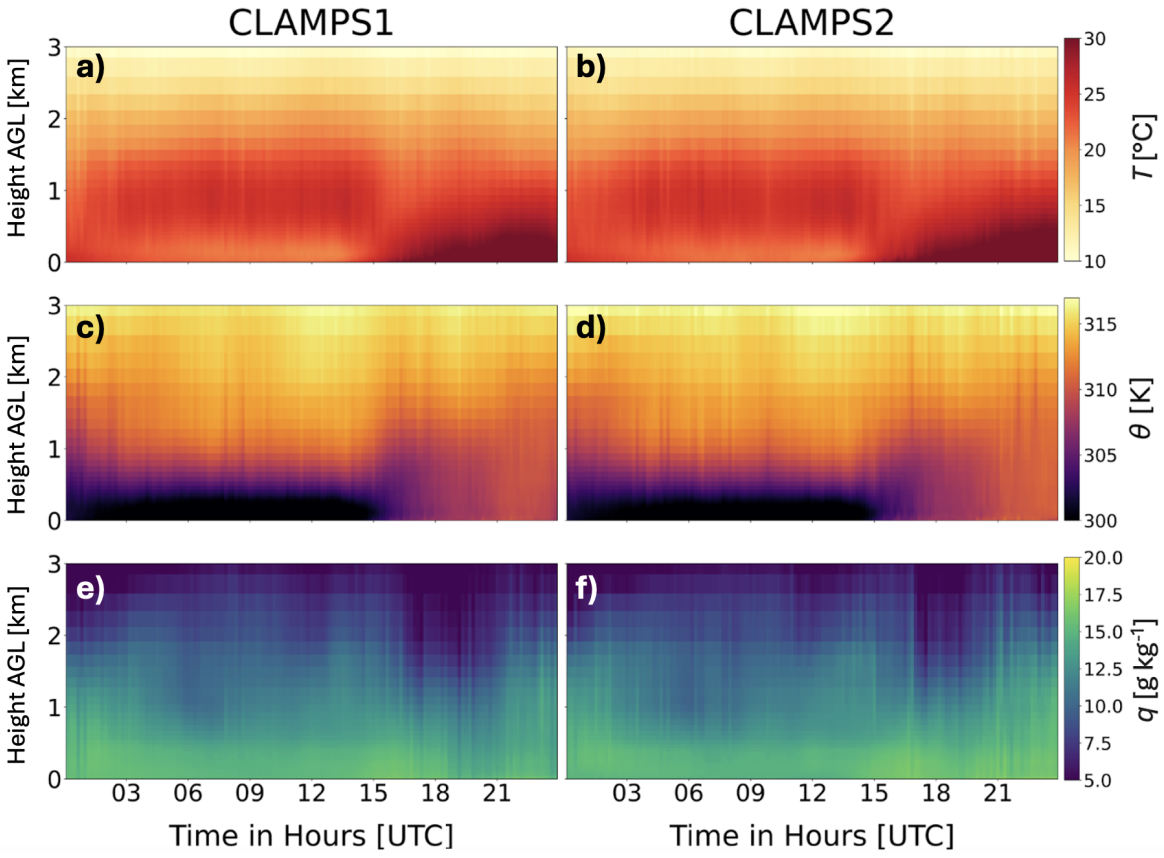


Figure 2.2: Sample TROPoe profiles of T, θ, and q from CLAMPS1 (left column) and CLAMPS2 (right column) from 23 September 2023.

This method is advantageous for examining thermodynamic ABL properties: defined in the prior covariance matrix, the correlation between different elements of the atmospheric state spreads the impact of a given observation to all correlated levels even

without direct observations at all levels, which can extend the depth of the resulting profile. On the same token, TROPoe provides a full posterior covariance matrix for the final retrieved profile from which one can obtain the 1-sigma uncertainty of the retrieval. An example of TROPoe processed retrievals showing T, θ, and q is available in Figure 2.2. There, 10-minute outputs are provided, which are standard for processing ARM-CF and CLAMPS TROPoe retrievals, but the temporal resolution can be user-defined in the VIP file.

TROPoe continues to be improved upon for better performance and accessibility, and users can run it themselves using open-sourced code at: `https://github.com/OAR-atmospheric-observations/TROPoe`. There are also ready-made TROPoe files routinely processed from ARM-CF (using AERI data) and from CLAMPS during field deployments (using AERI, MWR, or a combination of both, depending on availability). The availability of TROPoe across both platforms reflects the broader feasibility of producing additional value-added products from these datasets. In particular, the extensive data archives from ARM-CF and CLAMPS provide the kinematic and thermodynamic inputs necessary to run both the optimal estimation wind retrieval and fuzzy-logic ABL height algorithms.

2.1.3 Validation Field Datasets

It is within the interest of this study to evaluate the performance of the optimal estimation wind retrieval and fuzzy-logic ABL height algorithms on datasets consistent with those used in the wind farm analysis before applying them in that context. Performance is assessed using ARM-CF and CLAMPS data from past field campaigns, with many of the results drawn from Jordan et al. (2024). A map of all sites and instruments included in these analyses is provided in Figure 4. The campaigns used are described below and summarized in Table 1.

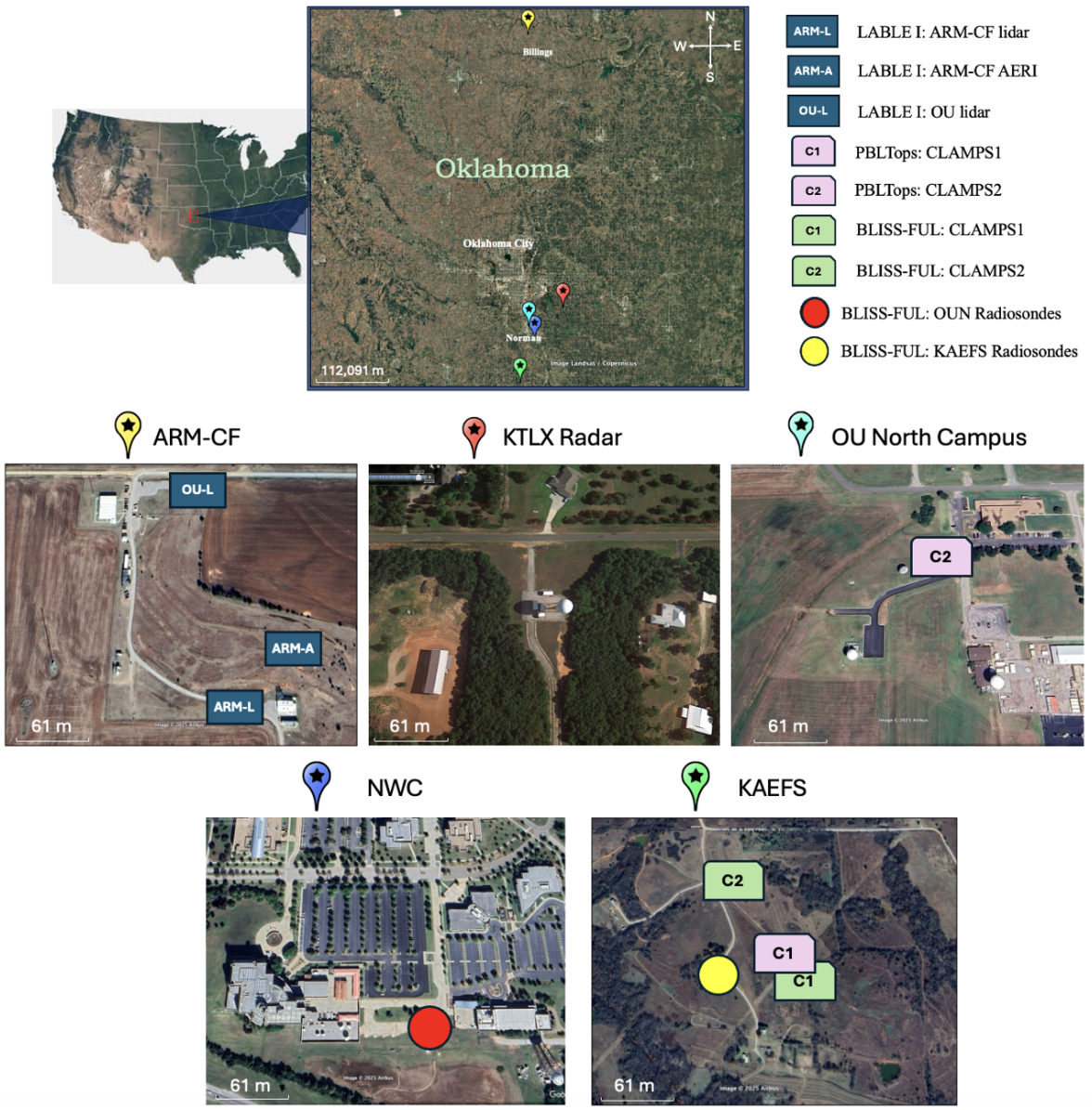


Figure 2.3: Map of field campaigns and observational instruments of interest beginning with the continental U.S (top left) and zooming into the north-central Oklahoma region (top middle). The sites at the bottom illustrate all stationary instrumentation sites or locations where campaigns took place, labeled based on the corresponding keys on the top right. Satellite imagery was obtained from Google Earth.

2.1.3.1 LABLE

The Lower Atmospheric Boundary Layer Experiment (LABLE; Klein et al. (2015)) took place at the ARM-SGP site. It was conducted to characterize ABL variability,

and it enabled personnel ranging from Ph.D. students to senior scientists to collect and analyze high-resolution observations. The campaign was made up of two periods: 18 September – 13 November 2012 (LABLE I), which targeted scientific objectives geared at exploring turbulent and thermodynamic processes, and 12 June – 3 July 2013 (LABLE II) to prioritize student-led testing of various instrument scanning strategies. Here, only the LABLE I time period is considered from which 34 cases were available. At the time, neither CLAMPS platform had been constructed yet, but the OU lidar that would eventually become part of CLAMPS1 was co-located with the ARM-CF lidar (36.6078° N, 97.4869° W). Datasets from ARM-CF lidar served as the reference against OU. The ARM-CF lidar collected PPIs using 8 azimuthal angles every 15 minutes at a 60° elevation angle, while the OU lidar sampled 72 azimuthal angles collected at two different elevation angles: 40° and 70° that alternated every 30 minutes. For comparative testing, the ARM-CF data was averaged to 30-minute time spacing to match the OU lidar timestamps, and the range gates between the two lidars were paired by closest match.

2.1.3.2 BLISS-FUL

From 3 June 2021 to 7 July 2021, the BLISS research group launched the BLISS Field Universalization Laboratory (BLISS-FUL) in collaboration with the Cooperative Institute for Severe and High-Impact Weather Research and Operations (CIWRO), and NSSL. Taking place at the OU's Kessler Atmospheric and Ecological Field Station (KAEFS) about 35 km south-southwest of the NWC, the campaign was geared at conducting field-readiness tests and calibrations of the CLAMPS instruments after periods of dormancy following the 2019 global SARS-COVID-19 pandemic. It also provided technical training for students on instrument operations, fieldwork protocols, collecting observations, and developing research hypotheses and analysis.

The BLISS-FUL campaign utilized both CLAMPS platforms co-located in the same setting where the lidars performed different scanning strategies. The CLAMPS1 lidar (34.9822° N, 97.5201° W) was programmed to constantly point vertically to measure high-temporal resolution w data, which was used to infer turbulence properties. At CLAMPS2 (34.9825° N, 97.5207° W), the lidar collected near-continuous VAD scans for high-temporal resolution horizontal wind observations. It also conducted vertical stares like the CLAMPS1 lidar, but the temporal resolution was coarser with a single stare occurring only between every 40-second VAD scan. The two CLAMPS were placed less than a km apart at KAEFS, a mostly flat, rural setting devoid of major obstructions that is comparable to the AWAKEN domain.

2.1.3.3 PBLTops

Another campaign, PBLTops, took place from 21 August – 3 September 2020 in which CLAMPS1 was deployed at KAEFS (34.9824° N, 97.5207° W) and CLAMPS2 was stationed at OU's North Campus (35.2366° N, −97.4637° W). This campaign extended further into September but CLAMPS1 data is no longer relevant after 3 September 2020 due to the repositioning of the platform. PBLTops data enables a comparison between the two CLAMPS in relatively close proximity; there was roughly 29.6 km in distance between the two platforms, they enacted the same scan strategies, and both deployment locations consisted of primarily rural surroundings. The lidars conducted 70° elevation PPI scans and operated in staring mode at all other times, yielding 1-second w scans for easy access to high-resolution σ_w information, and the AERI and MWR retrievals from both systems were available at a 10-minute resolution.

Table 2.1: Summary of three campaigns for testing the optimal estimation wind algorithm and the fuzzy logic ABL height algorithm.

Campaign	Period	Location(s)	Campaign Purpose	Platforms Deployed	Scan Strategy	Thermo. Data	Relevance to Algorithms
LABLE I	18 September – 13 November 2012	ARM-SGP 36.6078°N, 97.4869°W	Characterize ABL variability; explore turbulent and thermodynamic processes	ARM-CF lidar and OU lidar (co-located; pre-CLAMPS)	ARM-CF: 8-azimuth PPI, 60° elev., 15-min. OU: 72-azimuth PPI, 40° & 70° elev., 30-min	ARM-CF AERI	WINDoe evaluation: co-located lidars with different scan strategies enable direct wind retrieval comparison
BLISSFUL	3 Jun – 7 Jul 2021	KAEFS, ∼35 km SSW of NWC. CLAMPS1: 34.9822°N, 97.5201°W. CLAMPS2: 34.9825°N, 97.5207°W	Post-COVID instrument readiness tests, calibrations, and student training	CLAMPS1 and CLAMPS2 (co-located <1 km)	CLAMPS1: continuous vertical stare (w). CLAMPS2: near-continuous VAD and intermittent stare	AERI and MWR (both CLAMPS)	Fuzzy-logic ABL height evaluation: thermodynamic and kinematic data from co-located CLAMPS support algorithm testing
PBLTops	21 Aug – 3 Sep 2020*	CLAMPS1: KAEFS (34.9824°N, 97.5207°W). CLAMPS2: OU North Campus (35.2366°N, 97.4637°W)	Paired inter-CLAMPS comparison at two rural sites	CLAMPS1 and CLAMPS2 (separated ∼29.6 km)	Both: 70° elevation PPI and staring mode (1-sec w scans)	AERI and MWR (both CLAMPS), 10-min resolution	Systematic CLAMPS inter-comparison: separated deployment tests consistency of both WINDoe and fuzzy-logic retrievals across platforms

2.2 Algorithms to Evaluate for ABL Characterization

2.2.1 Optimal Estimation Wind Retrieval (WINDoe)

Another optimal estimation framework has emerged over the past few years that works similarly to TROPoe but for radial velocity inputs to extract ABL wind profiles. Baidar

et al. (2023) used lidar VAD scans with the intention to resolve gaps in information VADs leave after filtering out areas of low SNR. This mainly occurs where aerosols are sparse and in the near-surface ABL where PPIs are subject to a "blind zone" effect in the lidar's lowest range gates. Instead of removing low SNR signals, the study used optimal estimation to extract information from the noise as additional information that can be processed alongside the climatological prior. The findings were favorable but the algorithm could only ingest lidar VAD scans, so the algorithm was extended by Gebauer and Bell (2024) to adopt any Doppler lidar scan mode and combine multiple sources of wind data, such as radar wind profilers, surface meteorological observations or model information. It became the Wind via Optimal Estimation (WINDoe), with the ability to produce deep wind profiles and their uncertainty information that can be used alongside TROPoe profiles to deduce conditions throughout the entire ABL. Users interested in running the open-sourced WINDoe algorithm can navigate to `https://github.com/OAR-atmospheric-observations/WINDoe`.

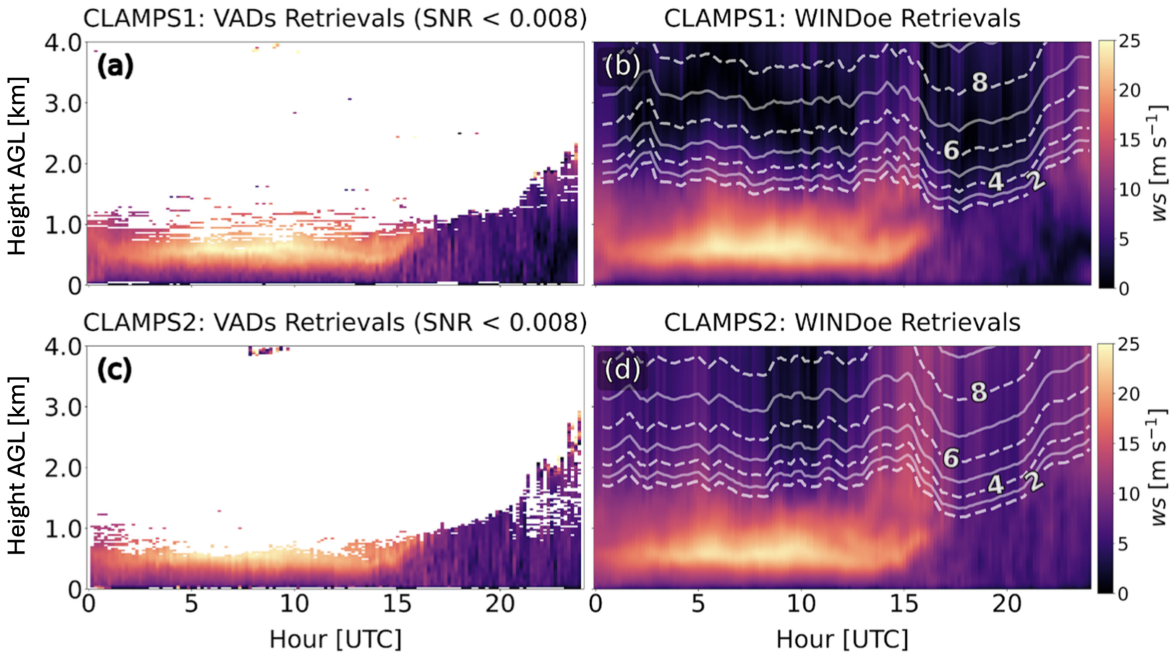


Figure 2.4: A comparison of VADs filtering at an SNR threshold of 0.008 from CLAMPS1 (Fig. 2.4a) and CLAMPS2 (Fig. 2.4c) with WINDoe retrievals from CLAMPS1 (Fig. 2.4b) and CLAMPS2 (Fig. 2.4d) for the case of 23 September 2023. White contours show WINDoe wind speed uncertainty in $\mathrm{m\,s^{-1}}$.

To demonstrate a visual of WINDoe, Figure 2.4 applies it to sample CLAMPS data during AWAKEN. There, we compare traditional 10-minute, SNR-filtered VADs against 10-minute WINDoe outputs from CLAMPS PPI scans. Detailed information about AWAKEN's deployment plan is delivered in Chapter 3, but the CLAMPS were located at sites with similar characteristics no more than 30 km from each other. Fig. 2.4a and 2.4c represent VADs with a minimum SNR threshold of 0.008 (about 21 dB), which is a common filtering value to apply but sometimes requires adjustment depending on weather conditions or aerosol content. Fig. 2.4b and 2.4d show WINDoe-processed observations with uncertainty information presented as contours with corresponding values (smoothed using a 30-min rolling window), detailing the vast difference in information content. Since each lidar's sensitivity differs slightly, a fixed SNR threshold produces data gaps at different heights across the two systems;

WINDoe helps compensates for this by replacing discarded low-SNR returns with optimally estimated values, improving inter-lidar consistency aloft.

	No NLLJ	Class 0	Class 1	Class 2	Class 3
ws [m s^{-1}]	< 10	≥ 10	≥ 12	≥ 16	≥ 20
Above-Nose Shear [m s^{-1}]	< 5	≥ 5	≥ 6	≥ 8	≥ 10

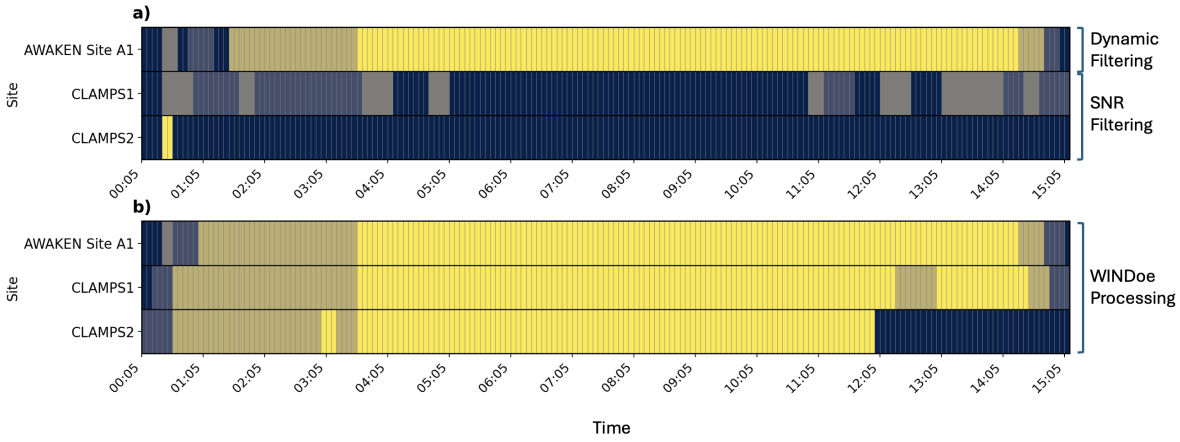


Figure 2.5: The classification metric for NLLJ magnitude (table) and the results of that classification applied to AWAKEN A1, CLAMPS1, and CLAMPS2 on 23 September 2023 (0005-15:15). In Figure 2.5a, each site showcases the results using different types of lidar data filtering: site A1 implemented a six-beam method with a dynamic filtering method, and both CLAMPS show VADs with the traditional SNR filtering at 0.008. These are compared with NLLJ classification results using the same data but retrieved via WINDoe (Figure 2.5b).

For the desired assessment of accurately classifying the NLLJ, WINDoe extends the wind profile beyond the lidar's reach, using climatological information when observations are too shallow to resolve the entire jet, but still drawing on level-to-level correlations near the height of the lidar's beam extinction. This framework allows the observations at these levels to provide meaningful information to constrain the retrieval rather than having it fall back entirely on climatology. As a result, WINDoe-resolved NLLJ estimates are expected to be generally reliable, as NLLJs do not typically extend into levels where retrieval uncertainty becomes large. The WINDoe skill in resolving the NLLJ can be examined through broad comparisons with other lidar-based approaches.

Quint et al. (2025) applied an automated NLLJ classification algorithm (White-

man et al., 1997; Vanderwende et al., 2015) to various lidars in AWAKEN's domain, which calculates how strong an NLLJ is based on the strength of its ws and above-nose shear. One site, A1 (only ∼10 km from CLAMPS1), had a scanning lidar operated by ARM-SGP that conducted a six-beam scan strategy and incorporated the dynamic filtering method (Beck and Kühn, 2017). Unlike a fixed SNR threshold, which discards all returns below a prescribed level, dynamic filtering identifies valid data by exploiting the self-similarity of valid measurements in the joint radial velocity–SNR space. This allows more data to be retained at the margins of the lidar's range where its signal is weak but physically meaningful, but dynamic filtering is still constrained to heights where backscatter is present: once the lidar signal is extinguished, no filtering strategy can recover wind information from the noise floor. On the other hand, WINDoe extends profiles into regions of vanishing signal by blending observations with a climatological prior. While considering differences in scan strategies, temporal resolution, and filtering techniques, the NLLJ strength classification was compared between sites A1, CLAMPS1, and CLAMPS2 (Figure 2.5) using the same 23 September 2023 case from Fig. 2.4. There, a table of the criteria of each class is also provided ranging from no NLLJ presence (No NLLJ) to very strong jets (Class 3). The A1 lidar was included in these comparisons despite performing a different scan strategy to showcase WINDoe's flexibility with ingesting different types of wind profiling scans. The CLAMPS lidar data were first examined with traditional SNR filtering applied (Fig. 2.5a), then again using WINDoe profiles (Fig. 2.5b).

With the traditional SNR filtering, the CLAMPS1 lidar detected a weaker NLLJ class for most of the period compared to A1, while the CLAMPS2 lidar struggled to detect the NLLJ through nearly the entire period. As seen in Fig. 2.4, the height of the NLLJ maximum was at a level where applying the SNR filter eliminated observation data specifically relevant to the above-nose shear condition used in this NLLJ classifi-

cation; it was captured best by A1's dynamic filtering. Conversely, when WINDoe was applied to all three sites, agreement drastically improved between both CLAMPS and A1 sites (Fig. 2.5b). The capability of WINDoe to incorporate any lidar scan type (e.g., CLAMPS VAD or Site A1's six-beam scan) serves well for consistency across multiple AWAKEN instruments for any other spatial comparisons useful during the wind farm analysis.

For testing the accuracy of WINDoe, the LABLE campaign was an ideal choice. The dual positioning of the ARM-CF and OU lidars allows for WINDoe to be compared to VAD scans to determine how realistic the high-altitude measurements are. There are also checks of agreement between WINDoe and VADs that can be performed whenever observations from the latter have high availability. Note that the data from the two lidars had certain differences between them despite being nearly identical systems that perform similar scan strategies. For instance, the ARM-CF lidar only employed one elevation angle while the OU lidar used two, but WINDoe can ingest both types of datasets. The ARM-SGP location is also suitable for this testing given that climatological radiosonde information that serves as the prior inputs directly originate from routinely-launched ARM-SGP radiosondes and will serve equally useful for CLAMPS wind farm analysis later as ARM-SGP lies directly within the domain of AWAKEN.

2.2.2 The Fuzzy Logic ABL Height Algorithm

The fuzzy-logic ABL height algorithm utilizes a fuzzy logic approach to compute the depth of the ABL continuously through daytime and nighttime. Unlike the TROPoe or WINDoe algorithms, this algorithm does not rely on long-term climatological information to resolve gaps in observations but seamlessly integrates multiple instruments bearing different capabilities for a synergistic H result, hereafter called H_{FL}. The concept of fuzzy logic has been used widely in the atmospheric science community, such

as for identifying non-precipitation echoes and radar artifacts (Gourley et al., 2007; Mahale et al., 2014), classifying hydrometeor methods (Vivekanandan et al., 1999; Liu and Chandrasekar, 2000; Park et al., 2009), and detection of precipitation modes (Yang et al., 2013). Bonin et al. (2018) first devised a composite fuzzy logic algorithm that could use Doppler lidar data to continuously measure H and its evolution throughout the diurnal cycle, which is a more robust alternative to instantaneous "snapshot" measurements provided by radiosondes.

The method was expanded by Smith and Carlin (2024) to include thermodynamic profiles as input parameters for even better representation of ABL conditions, particularly at nighttime when turbulence decays and H is difficult to rectify from kinematic measurements alone. In essence, the algorithm ingests multiple data streams and passes input data through membership functions that assign a measure of "truth," as opposed to binary true or false from Boolean logic. Next, a weighted mean is taken of all the values, where they can then be aggregated and the H is defined based on a predetermined threshold of that aggregate value (here, 0.5 is used, roughly requiring at least half the inputs to agree on the ABL membership condition).

This algorithm invokes a two-step process: the first step incorporates mixing measurements (σ_w, high-frequency σ_w, and inversion height). Smith and Carlin (2024) also implemented a stepwise weighting function defined by local sunrise and sunset times, ensuring the inversion height has presence in the algorithm overnight and during morning and evening ABL transitions. These inputs are aggregated, and, if the aggregate values are greater than the predetermined threshold, they are categorized as being within the ABL; values less than the threshold are categorized as being outside the ABL. The lowest level where conditions are no longer categorized as within the ABL represents H. The algorithm's second step is constrained by the initial estimate of H and includes indicators of mixing (e.g., SNR and SNR variance, u- and v-components

of the wind, and thermodynamic measurements) to produce a more refined estimate of H using the same general approach as in step 1. A visualization of these example variables going into each step is shown for an example day in Figure 2.6.

Smith and Carlin (2024) analyzed the performance of H_{FL} from multiple deployments to test the algorithm, from which sufficient results were found, but they investigated areas that contained surrounding infrastructure (the OUN office at the NWC), the platforms were not at the same site, or the sites were not local to Oklahoma. Since that study, both CLAMPS platforms were deployed for BLISS-FUL, collecting high-resolution kinematic (available as VAD or WINDoe-derived retrievals) and thermodynamic data (available as TROPoe-derived retrievals) in close proximity to one another. This offers a chance to study H_{FL} while eliminating added complexities of differing sites. Furthermore, each CLAMPS implemented different scan strategies, enabling the opportunity for deducing instrument settings for H_{FL} that are most ideal for the wind farm analysis. Lastly, BLISS-FUL had two sources of additional observational methods that can estimate H to compare with H_{FL}: 1) radiosonde data, which are intended to serve as a measure of true H due to their direct in-situ capabilities, and 2) radar data, which offers temporal-based coverage that radiosondes cannot provide; both of these sources are described further below. Comparing these three independent H-estimation methods provides deeper insight into the H_{FL} performance, particularly if done under various atmospheric conditions where some methods could falter where others do not.

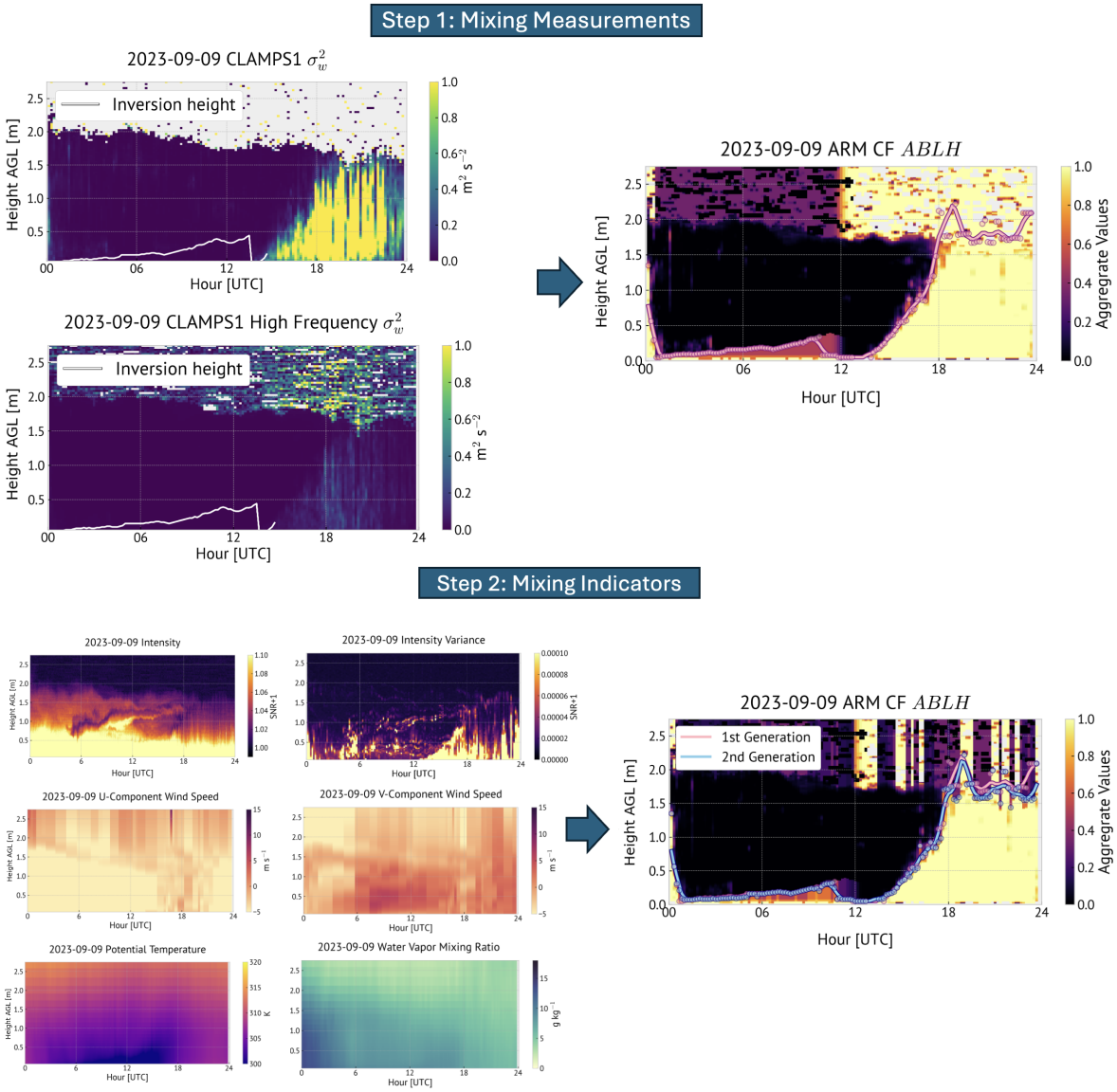


Figure 2.6: Time-height cross-sections of the variables considered in each step of the fuzzy-logic processing and their resulting H_{FL} outputs. Step 1 depicts profiles of mixing measurements (σ_w^2, high frequency σ_w^2, and inversion height) that help make up the first generation estimate, and step 2 shows profiles of mixing indicators (intensity, intensity variance, the u- and v-component ws, θ, and q) that help make up the second generation estimate. A more detailed diagram on each step can be found in Smith and Carlin (2024), specifically their Figure 4.

For comparison with these other H estimation methods, H_{FL} was computed ingesting the highest quality datasets either CLAMPS platform provided. CLAMPS1

vertical stares data were incorporated (w, intensity, and backscatter with a 0.008 SNR filtering applied), while the CLAMPS2 lidar supplied high-resolution ws and wd produced via WINDoe. The TROPoe retrievals were produced using AERI data from both CLAMPS, and the datasets from the two systems were consistent in temporal and vertical resolution, so H_{FL} was not sensitive to the choice of AERI input data. Therefore, θ and q profiles from CLAMPS2 TROPoe retrievals were chosen save for a single day they were unavailable (30 June 2021), in which CLAMPS1 AERI was used. Both CLAMPS lidars operated at an elevation angle of 70° and issued 18-m vertical spacing.

As in any application, potential limitations of the instruments could impact the algorithm. In addition to comparing and validating H_{FL} with other methods, it was tested independently under various temporal resolutions of kinematic data to assess when it performs most favorably. Further, H_{FL} outputs using WINDoe and VADs were compared to determine potential differences the two wind datasets may pose on the algorithm.

2.2.3 Validation Methodologies used during BLISS-FUL

2.2.3.1 The Radiosonde Method

The in-situ capabilities of radiosondes are typically relied upon to verify other methods of estimating H, but there are a plethora of different radiosonde H approaches from which to choose. Seven of the most common have been explicitly explored by Seidel et al. (2010): two parcel-based techniques, three gradient-based techniques, and two techniques that detect inversions. The classic parcel technique (h_{θ_v}), a commonly applied H indicator, determines the height at which virtual potential temperature (θ_v) becomes equal to its surface value (Holzworth, 1964). Coniglio et al. (2013) extended

this parcel technique, adding 0.6 K to the surface h_{θ_v} (denoted as $h_{\theta_v+0.6}$), intending to avoid shallow H detections in the evening ABL transition before the nocturnal inversion gets established (note that identifying the best correction value is still in progress, e.g., Liu and Liang (2010) applied a slightly smaller correction value of 0.5 K). The gradient-based approaches define H at the height of the maximum θ gradient (h_θ), the minimum relative humidity (RH) gradient (h_{RH}), and the minimum q gradient (h_q). Finally, H can be estimated where the top of the surface-based T inversion (h_{TOP}) and the bottom of the elevated T inversion (h_{BOT}) exists. An overview of these techniques is presented in Table 2.2, along with their different strengths and weaknesses as determined by previous studies, including Seibert et al. (2000), Seidel et al. (2010), Collaud Coen et al. (2014), Li et al. (2021), Duncan Jr. et al. (2022), and Kotthaus et al. (2023).

Although radiosonde H techniques are well regarded for estimating H, no single technique can serve as "true" H with 100% certainty; to date, H from any approach (radiosonde or otherwise) can only be inferred at best. However, there is a basis for an observed truth assumption by considering radiosonde estimates collectively. Smith and Carlin (2024) took the median of the seven aforementioned techniques (H_S). The median produces an overall H determined by where the majority of the techniques yield the best agreement while reducing the influence of outlier estimates. Regional expectations for H_S can be obtained from multi-year operational radiosonde launches, and any H_S from a BLISS-FUL radiosonde that aligns with these climatological expectations can be treated as H with stronger certainty. Such analysis can be further strengthened by separating out different weather environments, as more complex atmospheric conditions are expected to cause greater spread between techniques. Therefore, in addition to validating H_{FL}, the H_S of the radiosonde techniques during BLISS-FUL is also analyzed here as a suitable true H measure. Along with H_S, the standard deviation is measured to help determine the spread between the techniques considered.

Two sources of radiosonde data were available during BLISS-FUL. The first was operational OUN radiosondes from the Norman, OK NWS office (Lockheed Martin LMS-6). High-resolution, 1-second data were processed and made available for this research during the BLISS-FUL period and for the years 2011–2016 during the months of June and July (publicly available data can be retrieved, typically at a coarser resolution). Radiosondes from NWS offices around the U.S. are usually launched around 0000 and 1200 UTC each day (though the actual balloon releases often occur up to an hour before these times). The second source was International Met System iMet-4 radiosondes launched from CLAMPS1 at KAEFS throughout the period at times that OUN soundings typically are not released. These research-grade radiosondes returned data to a ground station at 1-second resolution located adjacent to CLAMPS1. All radiosonde data were quality controlled post-flight by the data provider (e.g., the NWS Radiosonde Replacement System applies corrections for solar heating and moisture hysteresis; United States National Weather Service, Field Systems Operations Center, Observing Systems Branch (2018)).

Table 2.2: Summary of all seven radiosonde techniques along with a description of their function as an H indicator, strengths, and weaknesses as identified by past literature.

Radiosonde Techniques	H Indicator	Strengths	Weaknesses
h_{θ_v}	First level where θ_v is equal surface value	Performs well in the CBL (Seibert et al., 2000)	High uncertainty may occur if there is no pronounced inversion CBL top (Seibert et al., 2000); is difficult to obtain in the SBL (Wang and Wang, 2010)
$h_{\theta_v+0.6}$	Same as h_{θ_v}, but with 0.6 K applied to surface value threshold avoid inaccurate observations of a shallow evening H before the stable-layer nocturnal inversion has finished growing	Avoids detecting shallow evening H before the nocturnal inversion is established (Coniglio et al., 2013)	Identifying the best correction value is still in progress
h_θ	Height of the maximum potential T gradient	Generally performs well in the CBL and SBL (Li et al., 2021)	Consistently yields high H compared to other methods (Seidel et al., 2010)
h_{RH}	Height of the minimum RH gradient	Performs well in the SBL (Li et al., 2021)	Overestimates in the presence of clouds; instrument errors are common in dry weather (Wang and Wang, 2014)
h_q	Height of the minimum q gradient	Better agreement with the gradient-based techniques of h_θ and h_{RH} (Seidel et al., 2010) than the rest of the techniques	Cloud layer could cause a false h_q due to excess water vapor (Ao et al., 2008)
h_{TOP}	Height of the top of a surface-based inversion	A distinct indication of a SBL (Bradley et al., 1993)	Ambiguous in presence of clearly defined surface inversion; may only be useful for SBL analysis (Seidel et al., 2010)
h_{BOT}	Height of the bottom of an elevated inversion	Asserts when and where mixing processes are capped in the PBL (e.g., Ao et al., 2012; Basha and Ratnam, 2009; Seidel et al., 2010)	Ambiguous in absence of elevated inversion (Seidel et al., 2010)

To compute H_S, both KAEFS and OUN sounding data were interpolated to a common 20-m vertical grid using a Savitzky-Golay third-order filter (Savitzky and Golay, 1964) with a 500-m smoothing window to assist in reducing localized fluctuations in the mean vertical profiles. Following Seidel et al. (2010), we exclude the h_{BOT} technique during the SBL since its existence assumes a different ABL structure than the other techniques under stable conditions. In these same periods, sensitivity testing in the emerging Jordan et al. (2026) showed h_{θ_v} often yielded unrealistically shallow H that was strong enough to bias the overall median and was thus also removed during the SBL. Lastly, h_{TOP} was removed during the CBL since surface-based inversions occur predominantly under stable conditions and are uncommon during the daytime. Other quality control procedures were applied as in Seidel et al. (2010) and Smith and Carlin (2024); we consider OUN and KAEFS sounding data between 50–2500 m, and the first observed data point from each profile was excluded to account for possibly large vertical gradients due to discrepancies in surface data entries and ground station processing applied to large differences in the data.

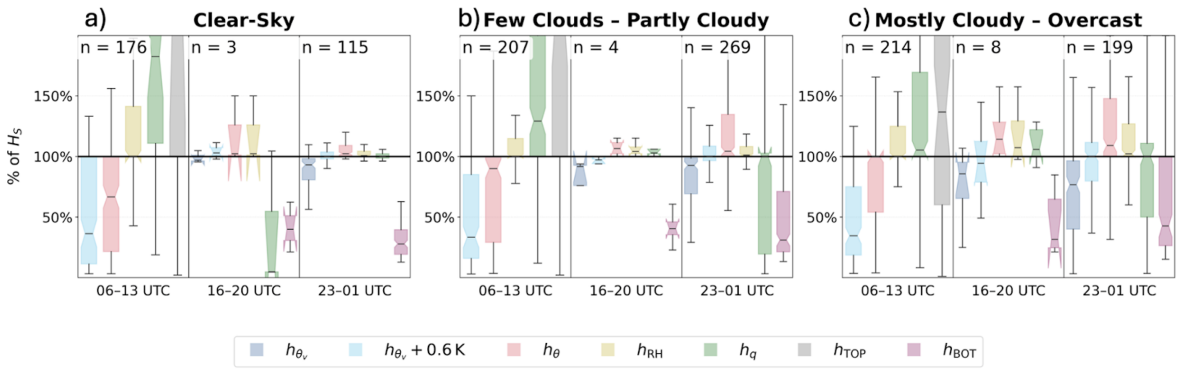


Figure 2.7: The seven radiosonde techniques as percentages of the H_S median (represented as the black horizontal line), separated by sky coverage conditions (Fig. 2.7a, 2.7b, and 2.7c represents clear-sky, few clouds-partly cloudy, and mostly cloudy-overcast, respectively). Within each sky condition category, a time window is applied for three different periods throughout the diurnal cycle to account for radiosondes not being released exactly on the hour. The number of samples (n) in each of these ranges is listed at the top left.

Long-term radiosonde data from OUN spanning the same months as the BLISS-FUL campaign but across multiple years were used to establish a regional H climatology from the method, providing the context needed to assess how representative the individual BLISS-FUL cases were of typical warm-season ABL conditions in the region. The datasets spanned June and July 2011–2016, and they were binned by three cloud cover conditions: clear-sky, few clouds-partly cloudy, and mostly cloudy-overcast. Sky conditions were derived from the Norman Westheimer Airport Automatic Surface Observing System (ASOS) archives (Iowa Environmental Mesonet, Iowa State University, 2021). Within the cloud cover bins, the data was also grouped by different launch times: 0600-1300 UTC (stable), 1600-2000 UTC (convective), and 2300-0100 UTC (evening transition). We summarize the resulting distributions in the notched box plots in Figure 2.7.

It is immediately clear that h_{TOP} had the largest deviation from the other techniques

in the stable period. There was frequent overestimation by this technique compared to the overall median in the SBL. There are two explanations playing a role: first, surface-based inversions are most pronounced under cool nighttime conditions, but the many years of ABL conditions in the SGP during the summer assessed here show that the altitude of nighttime inversions are variable. Secondly, it has also been found that both inversion techniques are sensitive to vertical resolution, where they can produce H at a questionable level if even minor fluctuations are present (Smith and Carlin, 2024). Fig. 2.7 was reproduced without including h_{TOP} in the SBL (not shown), but the results from the other techniques were unchanged, indicating that h_{TOP} is an extreme enough outlier that it is not likely to strongly impact the overall H_S, which relies on median computations which is more outlier-resistant than an average.

All other techniques disagreed more under clear-sky stable conditions than clear-sky convective conditions. The $h_{\theta_v+0.6}$ and h_θ techniques estimated shallower depths, while h_q commonly surpassed H_S levels. Findings from the parcel-based techniques were not surprising; they measure at the first height θ_v equals the surface value, which tends to occur much lower in the ABL than peaks in T or moisture profiles that correspond to the gradient-based techniques. The large percentile spread of h_q is particularly apparent under clear-sky conditions, suggesting high sensitivity for this technique, where cloud bases are associated with distinct thermodynamic gradients that are easier to detect. Accordingly, h_θ and h_{RH} seemed to also slightly improve under cloudier conditions, though not as drastically.

The greater spread among techniques during SBL conditions reflects the added complexities that occur in that period. The 1200 UTC soundings were frequently launched during the morning transition, with sunrises commonly preceded 1130 UTC (0630 local time). The accompanying shifts in ABL structure, such as the onset of thermal mixing and the decay of the NLLJ, likely degrade technique performance

when captured in the sounding profile. On the other hand, the convective cases were unlikely to be affected by evening transition dynamics, as sunset in June and July typically occurred well after the 0000 UTC sounding launch (around 0130 UTC, or 1630 local time). Given that technique agreement varies with sky conditions, as shown here, subsequent analysis separates cases by cloud cover to better isolate the conditions under which each method performs most reliably.

2.2.3.2 The Radar Method

Weather radars can observe clear-air Bragg scatter, which can provide information relevant for H detection. Bragg scatter is observed when well-mixed air at the top of the ABL and dry, free troposphere air are mixed by turbulent eddies, which causes fluctuations in q and T gradients (Wyngaard and LeMone, 1980; Fairall, 1991). If the refractive index perturbations produced by the turbulent mixing are on a spatial scale of half the radar wavelength, Bragg scattering occurs and the received signal is enhanced. As a result, turbulent mixing and the refractive index variability cause an enhancement of radar reflectivity Z, the maximum of which can be representative of H (Heinselman et al., 2009; Melnikov et al., 2011, 2013). However, Z associated with Bragg scatter can be obscured by biological scatterers (birds, bugs, and insects), which can have comparatively high Z. Differential reflectivity (Z_{DR}) — defined as the logarithmic ratio of Z at the horizontal and vertical polarizations (Seliga and Bringi, 1976; Kumjian, 2013)) — has proven to be valuable for differentiating between Bragg scattering and biological scatterers and can improve the detection of Bragg scatter capable of detecting H (Melnikov et al., 2011, 2013). Unlike Z measurements, which are additive, the intrinsic Z_{DR} of Bragg scatter is 0 dBz, allowing for easier differentiation from the high Z_{DR} characteristic of biological scatterers.

To measure Z_{DR}, it is necessary to employ radars with dual-polarization capa-

bilities, such as NWS Weather Surveillance Radar-1988 Dopplers (WSR-88Ds; Crum and Alberty (1993); Saxion and Ice (2012)). As opposed to single-polarization radars that only obtain data using a horizontally polarized electromagnetic wave, WSR-88Ds can acquire information using horizontally and vertically polarized signals to calculate Z_{DR}. Banghoff et al. (2018) used Z_{DR} values from WSR-88Ds to identify H in the CBL. PPI azimuths of Z_{DR} collected by WSR-88D radars were averaged across all PPI azimuths. Then, by converting range to height, quasi-vertical profiles (QVPs; Ryzhkov et al. (2016); Tobin and Kumjian (2017)) were computed at each volume scan time and constructed as time-height profiles for easy identification of the Bragg scatter over time. Within these quasi-vertical profiles, local minima of Z_{DR} coincide with Bragg scatter layers and, hence, can be used as a method to estimate the top of the ABL (H_R). Banghoff et al. (2018) shows several selected cases in which this Z_{DR}-identified H correlates well with a few aforementioned radiosonde H detection techniques in different seasons and regions in the continental United States. It should be possible to retrieve H_R from any of the 150 WSR-88Ds operated within the United States, which is highly attractive in terms of cost efficiency, spatial coverage, and the promise of long-term records (dual polarization upgrade was completed in 2013).

The location of the WSR-88D in the Twins Lake area south of Oklahoma City, OK (KTLX) enables the inclusion of H_R as another method to compare with H_{FL} from a source not too far from the CLAMPS at KAEFS during BLISS-FUL. Including the KTLX H_R provides an H estimate continuous throughout time alongside H_{FL}, offering additional context in periods without radiosonde launches and providing another source of understanding of the expected behavior relative to conditions of the day. Overnight, the radar method is not expected to perform well due lack of turbulence and the minimum observing height given the radar elevation angle impeding observations at very low levels (though research is currently ongoing to understand techniques and

indirect methods for outlining the SBL's residual layer).

For this analysis, QVPs were produced using the same steps as Banghoff et al. (2018), where mean profiles were produced from averaging the PPI scans. The Z_{DR} minima within Bragg scatter signatures were used to identify H_R. Gates with Z_{DR} values below -2 dB were excluded to remove ground clutter and noise, as well as those with both $Z > 0$ dBz and $\rho_{hv} > 0.8$ to remove gates likely to be contaminated by precipitation. Banghoff et al. (2018) employed an elevation angle of 4.5°, so the closest elevation angle to 4.5° was also applied here (typically within 0.1°), which was still high enough to minimize effects of ground clutter, beam ducting, or superrefraction. We must keep in mind that a 4.5° elevation angle in ideal atmospheric conditions means the first gate of usable data from the WSR-88D (at a range of 2125 m) approximately 310 m. Since the current implementation of this method is only known to be valid in convective conditions, H_R is only shown from 1200–0000 UTC.

Note that the surface characteristics at KTLX differ from the other two sites. The KTLX radar is located 65 km north-northeast of KAEFS and 35 km from the OUN office, and it is surrounded by dense tree cover and gently rolling terrain, though the broader landscape remains largely flat with sparse infrastructure. This setting poses some similarities to the KAEFS site, which is characterized by relatively flat land with scattered rolling hills and creeks, though tree coverage is considerably greater at KTLX. In contrast, NWS OUN is situated among university buildings, parking lots, and managed lawns, with the town of Norman to the north and natural vegetation with shrubs and low trees to the south. The surface differences from KTLX and the other locations should be kept in mind when interpreting site-to-site differences in the data.

2.3 Results: Performance, Sensitivity and Quality Control

2.3.1 WINDoe Performance Evaluation

We evaluated WINDoe performance by comparing retrievals from the ARM-CF lidar, serving as the reference dataset, and the OU lidar across the LABLE I cases (Figure 2.8). This comparison is presented in three ways: Fig. 2.8a shows SNR-filtered VADs from the OU lidar (40° elevation angle) compared to those from the ARM-CF (60° elevation angle), Fig. a repeat of this comparison in 2.8b but for the OU lidar scanning at a 70° elevation angle, and Fig. 2.8c shows 30-minute WINDoe retrieval comparisons from ARM-CF (60°) and OU (40° and 70° combined). Setting lidar scans to higher elevation angles yields better sampling with height and improved sensitivity to vertical wind motion, as the beam orientation more closely aligns with the vertical axis, but this geometry also means that horizontal winds contribute only a small fraction of the measured radial velocity. As a result, any retrieval error in that component is mathematically amplified when projecting back to horizontal wind speed. Conversely, lower elevation angles orient the beam more nearly horizontally, directly capturing horizontal flow and sampling a broader horizontal circle that smooths small-scale variability, but the beam ascends slowly with range, limiting data recovery at upper levels where the geometry becomes unfavorable for retrievals.

Despite differing elevation angles and, at times, range gate spacing, the VADs agreed remarkably well between the two lidars in Figs. 2.8a-b, consistent with Baidar et al. (2023) and Gebauer and Bell (2024). Agreement was strongest at 500 m, where both of OU's elevation angles produced a near one-to-one correspondence with ARM-CF. The greatest disagreement occurred at 91 m in Fig. 2.8b, between the ARM-CF 60°

and OU 70° beams. This occurred because steeper elevation angles sample more of the vertical wind component and less of the horizontal, reducing their accuracy at low levels; this leads to comparing two sets of independently degraded low-level estimates rather than one accurate reference against one poor one. Steeper angles also place the effective blind zone at greater heights above the surface, further inhibiting low-level accuracy between 60° and 70° beam comparisons. This explains the better agreement at 91 m in Fig. 2.8a: despite the larger angular difference between OU's 40° and ARM-CF's 60° beams, the 40° geometry yields more accurate low-level wind speed retrievals, producing better overall correspondence.

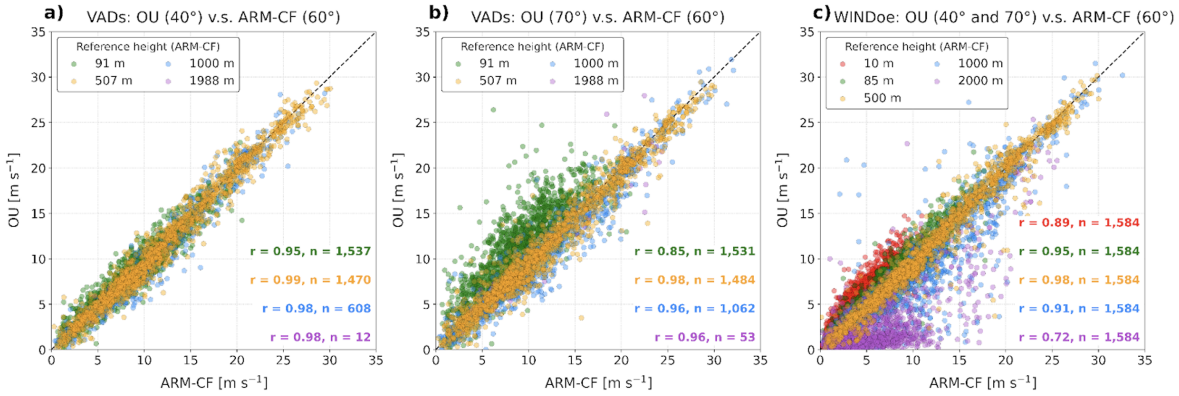


Figure 2.8: Scatterplots of ARM-CF and OU lidar VADs during LABLE I when the OU lidar was scanning two different elevation angles (40°; Fig. 2.8a, and 70°; Fig. 2.8b). The VADs were SNR-filtered at 0.008. The same is shown in Fig. 2.8c but for WINDoe, where the OU output was comprised of both the 40° and 70° elevation angles together. Results from four different range gates throughout the ABL are shown for all panels except Fig. 2.8c., which included a fifth measure at 10 m to demonstrate the abilities of its coverage.

In Fig. 2.8c, which represents WINDoe-to-WINDoe comparisons, there was greater scatter aloft, especially around 2 km. At first glance, the ARM-CF lidar appears to overestimate ws values at these heights; however, this reflects how the optimal estimation framework responds to diminishing SNR ratio rather than a systematic

bias. As SNR decreases above each lidar's effective range, WINDoe progressively draws towards the climatological prior, which differs from the VADs in Figs. 2.8a–b: it simply exclude retrievals where SNR falls below their 0.008 threshold. Unlike the VADs in Figs. 2.8a-b, where sample counts decrease steadily with altitude, WINDoe yields the same number of samples at all heights. The apparent overestimation aloft therefore reflects the inclusion of prior-influenced retrievals at heights where the VAD has already lost coverage; these are not cases with strong observational signal but rather profiles where the algorithm, by design, acknowledges limited information by blending toward the prior. A similar pattern was reported in Baidar et al. (2023), and they also compared VADs and results from the wind retrieval algorithm. Observing the same behavior here, even when one of the analyzed lidars operates a different scan configurations, helps provide confidence that datasets from both systems perform as expected under the WINDoe approach and supports the use of the OU lidar for when it becomes a part of CLAMPS1 for wind farm analysis.

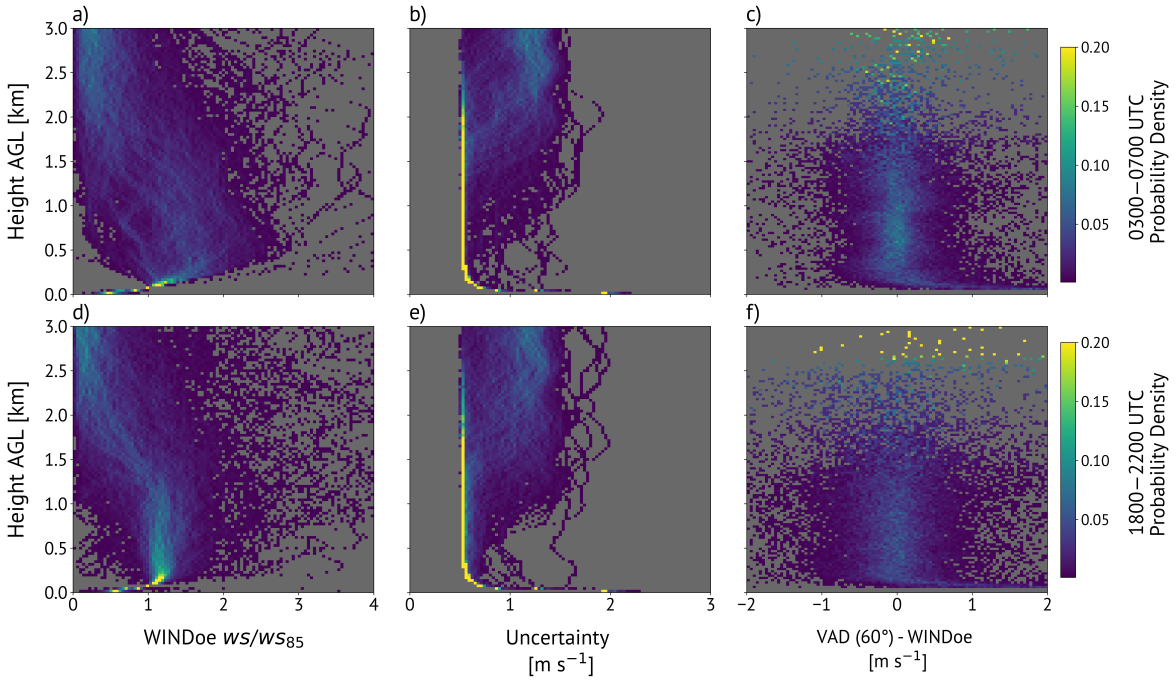


Figure 2.9: Probability density functions of the ARM-CF lidar for WINDoe ws, its uncertainty, and the difference between VADs and WINDoe for a period of time in the SBL (Figs. 2.9a-2.9c) and the CBL (Figs. 2.9d-2.9f).

We can further investigate any discrepancies aloft that WINDoe may introduce or amplify using conditional probability density functions. We computed these for WINDoe ws (normalized by ws at 85 m to enhance visibility of the shape of the wind profiles), its uncertainty, and the difference between VAD and WINDoe retrievals for a day and night time window (0300–0700 UTC; Figs. 2.9a-c, and 1800–2200 UTC; Figs. 2.9d-f). WINDoe in Fig. 2.9a showed the expected vertical ws profile with height, where areas of stronger ws are representative of NLLJ signatures and probabilities above this layer shift towards lower ws. The uncertainty in Fig. 2.9b was concentrated at less than 1 m s^{-1}, which gradually increased in altitude as SNR declined. Other than that, though, probabilities were overall close to zero with few exceeding a difference of 1 m s^{-1}.

The daytime and nocturnal VAD-WINDoe distributions were broadly similar, though daytime cases showed more dispersion over the CBL (Fig. 2.9f), consistent with a more turbulent and rapidly evolving ABL (i.e., less uniform flow than with the NLLJ). Under convective conditions, ws and wd can vary more rapidly in both time and height, which challenges the assumption of the VAD technique that flow is horizontally homogeneous across the scanning cone. This assumption becomes increasingly difficult to satisfy at greater heights, where the scan radius expands and spatial variability within the retrieval volume grows. By contrast, WINDoe retrieves the entire wind profile at once using a prior wind profile covariance that accounts for level-to-level correlations, so modest discrepancies between the two retrieval methods at this time is reasonable.

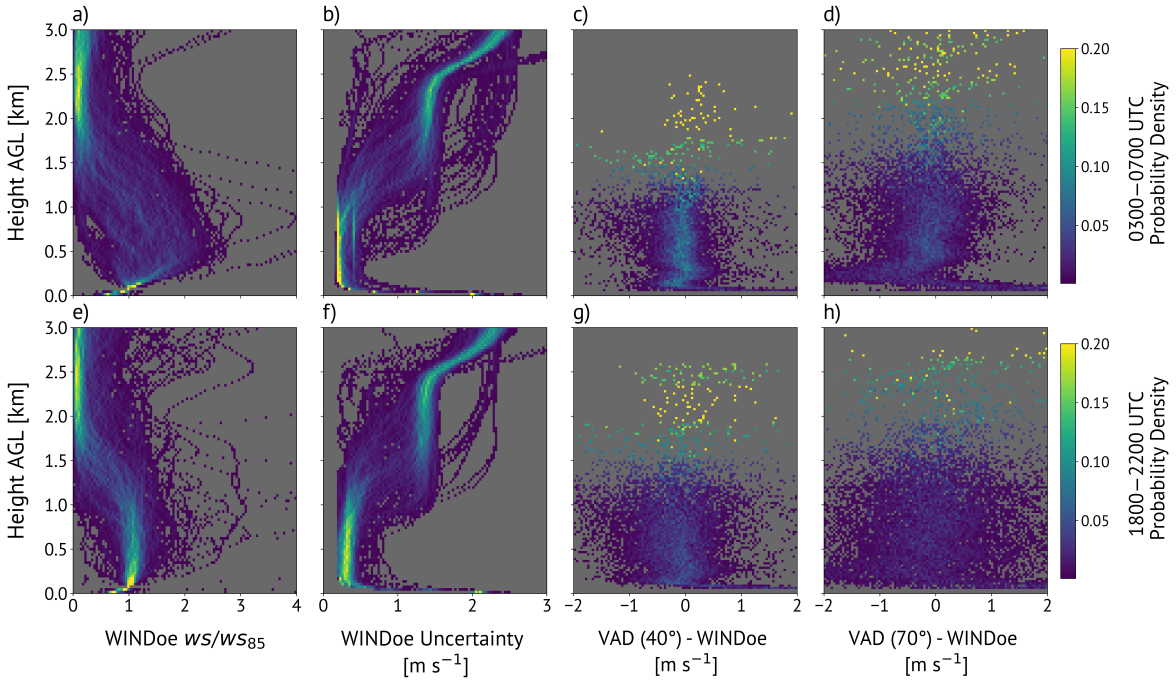


Figure 2.10: As in Figure 2.9, but for the OU lidar. Here, the difference was measured at both the 40° and 70° elevation angles.

The same analysis was applied to the OU lidar data (Figure 2.10). In the nocturnal

ws profiles (Fig. 2.10a), there looked to be fewer observations of stronger *ws* aloft compared to ARM-CF data (Fig. 2.9). This is a reflection of the differences in vertical resolution between the two lidars, where the higher-resolution data from the OU lidar grew sparse at lower heights than the ARM-CF lidar. The original intent was to capture both lower and upper ABL flow using the two elevation scanning angles from the OU lidar; however, differences in range gate spacing led to limitations aloft. The OU lidar's finer vertical resolution (18 m), compared to the ARM-CF's lidar (30 m), resulted in a smaller sampling volume and fewer scattering targets, which increased noise and reduced data quality at higher altitudes. This is portrayed in Fig. 2.10b where uncertainties dramatically increased aloft compared to ARM-CF, which is tied to the high disagreement at 2000 m in Fig. 2.8c. Figs. 2.10c and 2.10d depicted less scatter in the retrieval differences than ARM-CF in Fig. 2.9, though this also came with the cost of less vertical coverage from the OU lidar. The largest differences between the two methods happened in the lower levels during daytime (Figs. 2.10g–h); while the daytime *ws* distribution (Fig. 2.10e) was similar in shape to the nocturnal case in Fig. 2.10a, the uncertainty (Fig. 2.10f) was less tightly constrained near zero than at night, consistent with the more turbulent and variable CBL conditions discussed above.

Figures 2.8–2.10 show that the OU lidar aligned well with the ARM-CF lidar from VAD retrievals within the range of observable data, helping to support the reliability of both systems for the wind farm analysis. When the WINDoe algorithm was examined, profiles between the two lidars matched closely at 10-m, even though these types of scanning lidars are unable to reliably sample below about 60 m. Although WINDoe can assimilate surface meteorological station data, Gebauer and Bell (2024) and subsequent ongoing work suggests that WINDoe near-surface winds remain robust with or without this addition. The layer between the surface layer and the lowest observed lidar height

is small enough that is largely anchored by the lidar observations above (i.e., through layer-to-layer correlations), and adding a surface constraint typically only makes a modest difference to the inferred near-surface winds. Therefore, the wind farm analysis presented here uses lidar-only inputs in WINDoe to ensure consistency across sites and over long-term periods when other instruments are unavailable.

The results also inform on how scan patterns also play a role on the WINDoe retrievals. The OU lidar used here is later implemented into CLAMPS1, and scans from both CLAMPS platforms often operate only at 70° for the research interests of OU and NSSL. At this steeper elevation angle, the beam projects only weakly onto the horizontal plane, but reduces retrieval uncertainty aloft where shallower scan angles would have already lost signal. If the wind farm analysis was specifically centered on changes in flow patterns in the lower levels, the scan setting of 40° or lower would likely be better for the analysis. The primary goal of applying WINDoe here is to fully resolve all NLLJ occurrences to ensure proper binning of cases based on how NLLJ strength is classified. As such, using a higher elevation angle better samples winds deeper in the ABL, so the 70° setting remains preferred for the CLAMPS lidars during AWAKEN.

2.3.2 Sensitivity of H_{FL} to Input Data

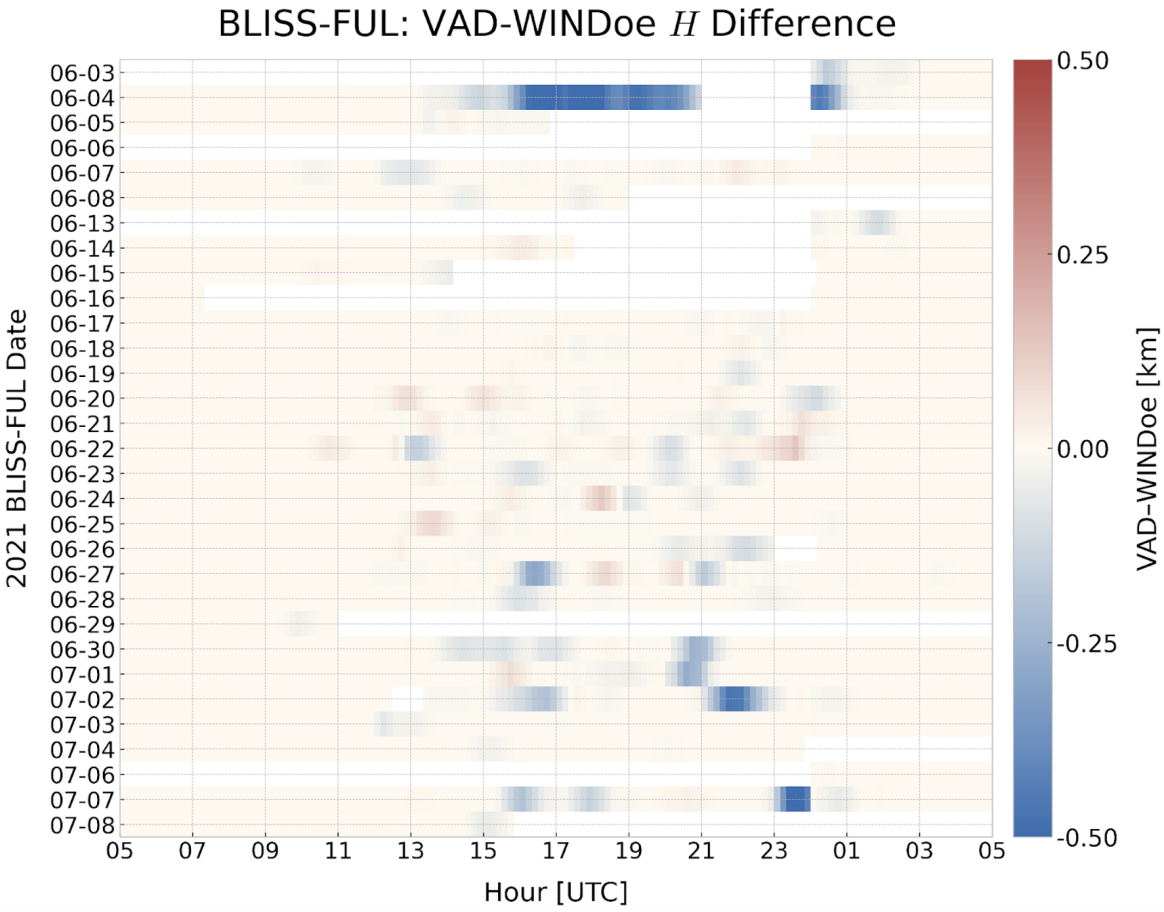


Figure 2.11: Differences between H_{FL} using VAD- and WINDoe-derived wind profiles throughout the 0500-0500 UTC diurnal cycle for all BLISS-FUL cases. White areas indicate periods of missing data.

Before comparing the fuzzy-logic algorithm to other H estimation methods, it was necessary to first establish which available datastreams were most appropriate as algorithmic inputs. While the algorithm in principle relies on VAD retrievals as the wind profile input, the work presented here represents the first implementation of WINDoe-derived winds in this capacity. Therefore, a comparison between H_{FL} incorporating WINDoe versus VAD wind inputs was conducted to characterize any differences intro-

duced by this choice. Figure 2.11 shows plots of those differences across all BLISS-FUL cases. The SBL was nearly void of any differences between either output, signifying that VADs or WINDoe could be applied during nocturnal conditions. However, the CBL exhibited both positive and negative differences as high as 250 m with WINDoe-derived H_{FL} had more instances of measuring lower compared to VADs-derived H_{FL}. The largest differences occurred over a span of several hours in the afternoon on 4 June 2021; the exact cause is unknown but immediate loss of data after these differences suggests a possible instrument malfunction rather than discrepancies stemming from the retrievals themselves.

For the remaining differences, it is suspected the Haar wavelet transform in the second generation aggregation struggled to identify gradients in the WINDoe profiles. This is plausible because WINDoe profiles are more vertically smooth than VADs, which can weaken the sharp gradients the wavelet transform targets. VAD profiles also often ended more abruptly before noise dominates aloft, whereas WINDoe transitions smoothly into areas dominated by high uncertainty. Investigating these discrepancies in more detail is a worthwhile topic for future work, but going forward, we proceed with the fuzzy-logic-based processing using WINDoe to favor incorporating extended ABL profile coverage into the algorithm.

It was also desired to assess how different temporal resolution of the ingested datastreams impacts the resulting H_{FL}. If VADs better retain relevant information content during the daytime than WINDoe, it is also sensible to investigate if H_{FL} also benefits from additional information content provided by VADs at high temporal resolutions. Given ws and wd information enter the algorithm during its second generation, we hypothesise that high-resolution w observations (which contribute most heavily to the first generation) would yield the best representation of H_{FL}. To evaluate this hypothesis and determine optimal scan priorities, tests were conducted using different temporal

resolutions of lidar w and VAD data for the 0500-0500 period. Different inputs of the lidar data were as follows:

- 1-second w from CLAMPS1 (high-res w),
- CLAMPS1 w downsampled to 10-second resolution (low-res w),
- 40-second VADs from CLAMPS2 (high-res VAD), and
- CLAMPS2 VADs downsampled to 5-minute resolution (low-res VAD).

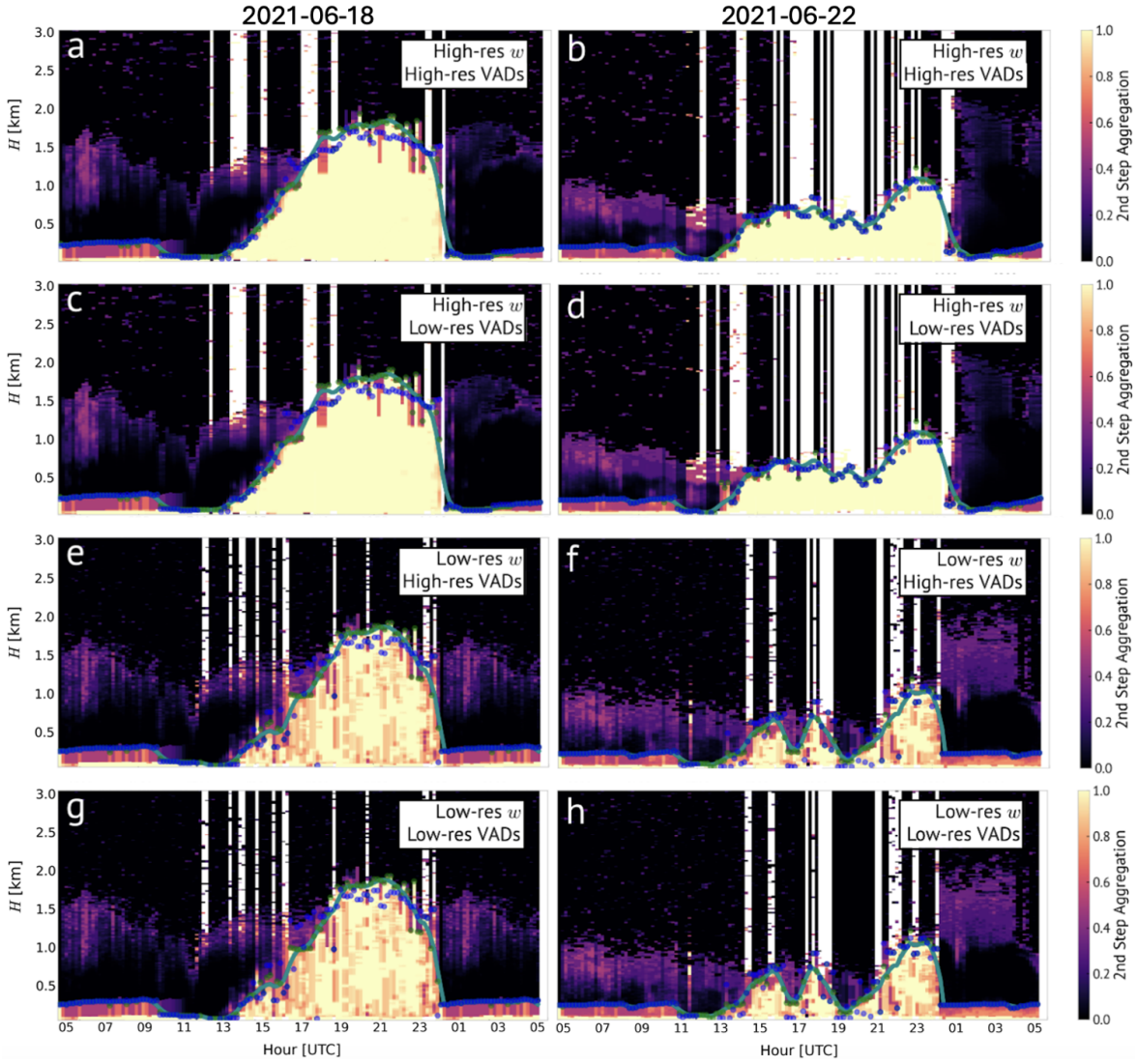


Figure 2.12: A comparison of second-generation aggregate values for the two clear-sky cases: 18 June 2021 is shown in the left column, and 22 June 2021 in the right column. Whether the input data has high- or low-resolution w or VAD data is detailed in the panel inserts as 'high-res" or "low-res".

Figure 2.12 shows second (final) generation aggregate values of H_{FL} results from two selected cases with almost completely clear-sky conditions. Initial tests employed 40-second w data from CLAMPS2, but subsequent tests adopted a 10-second temporal resolution using downsampled CLAMPS1 data, better reflecting a temporal resolution

setting more likely to be applied in broader applications.

In both cases, there was little-to-no change to all H_{FL}, even when applying low-resolution VADs (Figs. 2.12a-d). However, notable differences are presented in the Figs. 2.12e and 2.12f results where combining high-resolution VADs and low-resolution w observations led to large differences. The aggregate values were noisier, and the uncertainty was higher, particularly after 2100 UTC for both cases. This introduced large dips at 1700 and 1900 UTC on 22 June 2021 that did not exist before, causing a reduction in H_{FL}. When both w and VAD observations consisted of low resolution inputs, the 22 June 2021 computation in Fig. 2.12h showed slightly different areas of low aggregated values at 1400 UTC, but there were otherwise no noticeable changes in H_{FL} there or in the 18 June 2021 H_{FL} with respect to Fig. 2.12e.

These findings highlight the value of measuring high-resolution w for obtaining quality results using the fuzzy-logic algorithm. This should not be interpreted as a suggestion to neglect VAD scans from the algorithm; ws and wd are important inputs to the algorithm in the second generation step. The recommendation to users considering building scans compatible with H_{FL} is to simply prioritize high-resolution vertical staring modes alongside other scan types in their lidar scan strategies. In terms of optimal wind farm analysis, high-resolution 1-second stares data are available from both long-term ARM-CF lidar data and both CLAMPS lidars during AWAKEN.

2.3.3 Fuzzy-Logic ABL Height Performance Evaluation

Comparisons between the radiosonde, radar, and fuzzy-logic methods took place over multiple BLISS-FUL days. These comparisons were separated into the three different sky conditions as done when evaluating the radiosonde method (section 2.2.3.1): clear-sky, few clouds-partly cloudy, and mostly cloudy-overcast. In an effort to target cases with consistent conditions at OUN, KTLX, and KAEFS, sky conditions were classified

using categorical sky cover observations from the same ASOS resource used for the long-term OUN analysis, but for here at the Chickasha Municipal Airport in Chickasha, OK (42 km west of KAEFS). In addition, GOES-16 satellite imagery (National Centers for Environmental Information, 2026) was then used to spatially confirm that the classified conditions were representative across all three sites; infrared imagery was used for soundings launched under SBL conditions prior to sunrise, while visible imagery was used for all other launch times.

Other surface weather conditions stemmed from the Washington, Oklahoma Mesonet station (Brock et al., 1995) located at KAEFS, and Table 2.3 details some of these meteorological variables along with the sky conditions for all the BLISS-FUL radiosonde launches. Two BLISS-FUL cases were selected for each sky-coverage category where sky conditions at all sites were most consistent throughout midnight-to-midnight local time (0500-0500 UTC). These are represented as time-height cross-sections from 0500–0500 UTC local time as opposed to 0000–0000 UTC to better view time results from radiosondes launched around 0000 UTC.

To determine if BLISS-FUL radiosondes can serve as validation, the H for the different sounding techniques and the median value, H_S, from all OUN and KAEFS radiosondes is presented in Table 2.4. The KAEFS campaign soundings show the same trends as observed with the long-term OUN radiosonde results shown in Fig. 2.7. The h_q technique consistently overestimated H in BLISS-FUL for all stable periods while exhibiting better consensus with the other techniques in the CBL. Similarly, the parcel-based techniques produced the lowest H compared to the other techniques as expected, with the exception of 6 July 2021. In regards to the inversion-based techniques, h_{TOP} always surpassed all the techniques except h_q on 25 June 2021 and h_{BOT} routinely measured more shallow depths. The most consistent agreement between techniques was between $h_{\theta_v+0.6}$, h_{θ_v}, and h_{RH} during the SBL. These results are consistent with

the long-term OUN radiosonde climatology shown in the notched box plots of Fig. 2.7, indicating that the BLISS-FUL soundings sampled conditions that are climatologically representative of the region. As such, H-values from the BLISS-FUL radiosondes were adopted as reference for evaluating the performance of the fuzzy-logic and radar-based boundary-layer H estimation methods.

Table 2.3: Weather conditions at each radiosonde launch time for the nine BLISSFUL cases of interest. For OUN radiosonde launches, all surface observations listed below come from the NWC Mesonet site. For KAEFS radiosonde launches, sky coverage data comes from the Automatic Surface Observing System (ASOS) at the Chickasha Municipal Airport in Chickasha, OK (42 km west of KAEFS; data available at `https://mesonet.agron.iastate.edu/request/download.phtml?network=OK_ASOS`). The cloud cover data was verified with GOES-16 visible satellite data. The rest of the data comes from the Washington, Oklahoma Mesonet station located at KAEFS. F.C. = 'few clouds', P.C. = 'partly cloudy', and M.C. = 'mostly cloudy.' Shaded row colors correspond to cases of interest for comparing H methods and their sky conditions (clear-sky = blue, few-partly cloudy = yellow, mostly-overcast = grey).

Case Day and Site Launch Time	Air Temperature (°C) at 1.5 m	RH at 1.5 m (%)	Wind Speed (m s^{-1}) at 10 m	Solar Radiation (W m^{-2})	Sky Coverage
17/06/2021					
OUN 1127 UTC:	22	83	1.79	11	Clear
KAEFS 1446 UTC:	28.8	64	4.3	590	Clear
OUN 2309 UTC:	32.1	46	3.6	206	F.C.
18/06/2021					
OUN 1126 UTC:	22	88	1.79	11	Clear
OUN 2310 UTC:	32.6	44	4.8	294	F.C.
21/06/2021					
OUN 1136 UTC:	25.1	80	1.79	1	Overcast
22/06/2021					
KAEFS 2203 UTC:	28.1	38	5.8	600	Clear
25/06/2021					
OUN 1141 UTC:	26.6	72	3.3	0	P.C.
26/06/2021					
OUN 1901 UTC:	26	79	3.3	655	Overcast
28/06/2021					
OUN 2237 UTC:	28	72	2.1	570	M.C.
06/07/2021					
KAEFS 2024 UTC:	30.5	58	1.2	803	P.C.
KAEFS 2121 UTC:	30.6	59	3.9	539	P.C.
KAEFS 2220 UTC:	31.2	58	3.5	645	P.C.
KAEFS 2333 UTC:	30.8	59	1.5	352	P.C.
07/07/2021					
KAEFS 1029 UTC:	21.5	98	1.3	0	M.C.
KAEFS 1524 UTC:	29	72	2.1	678	F.C.

Table 2.4: Overview of the radiosonde-based H (km) for the entire period and their detections in km from each of the seven techniques. The H_S and SD values are also listed. The * symbol indicates the techniques that match with H_S. SD refers to the standard deviation of the techniques.

Case Day and Site Launch Time	h_{θ_v}	$h_{\theta_v+0.6}$	h_{θ}	h_{RH}	h_q	h_{TOP}	h_{BOT}	$\boldsymbol{H_S}$	**SD**
17/06/2021									
OUN 1127 UTC	–	*0.06	*0.06	*0.06	0.78	1.04	–	0.06	0.424
KAEFS 1446 UTC	0.06	0.06	*0.24	0.720	0.720	–	0.4	0.24	0.265
OUN 2309 UTC	0.06	1.26	1.24	*1.2	*1.2	–	0.4	1.2	0.480
18/06/2021									
OUN 1126 UTC	–	*0.06	*0.06	*0.06	0.340	nan	–	0.06	0.121
OUN 2310 UTC	1.48	1.86	1.96	1.96	1.96	–	0.32	1.92	0.09
21/06/2021									
OUN 1136 UTC	–	*0.06	*0.06	*0.06	2.08	2.12	–	0.06	0.999
22/06/2021									
KAEFS 2203 UTC	1.26	1.3	1.34	2.38	2.38	–	0.44	1.3	0.778
25/06/2021									
OUN 1141 UTC	–	0.22	*0.66	*0.66	1.780	0.880	–	0.66	0.517
26/06/2021									
OUN 1901 UTC	0.44	0.52	1.68	1.64	1.62	–	0.28	1.07	0.621
28/06/2021									
OUN 2237 UTC	1.0	1.22	2.0	2.02	2.02	–	0.420	1.22	0.681
06/07/2021									
KAEFS 2024 UTC	2.00	2.18	0.14	1.940	*1.24	–	0.46	1.590	0.788
KAEFS 2121 UTC	2.2	2.36	0.14	1.5	0.6	–	*0.32	0.32	0.943
KAEFS 2220 UTC	1.14	1.34	*1.32	1.36	1.36	–	0.4	1.320	0.452
KAEFS 2333 UTC	2.120	2.26	0.14	2.2	0.06	–	0.28	1.2	1.023
07/07/2021									
KAEFS 1029 UTC	–	*0.06	*0.06	*0.06	0.72	3.64	–	0.06	1.39
KAEFS 1524 UTC	0.78	1.04	0.72	*0.7	0.68	–	0.28	0.7	0.266

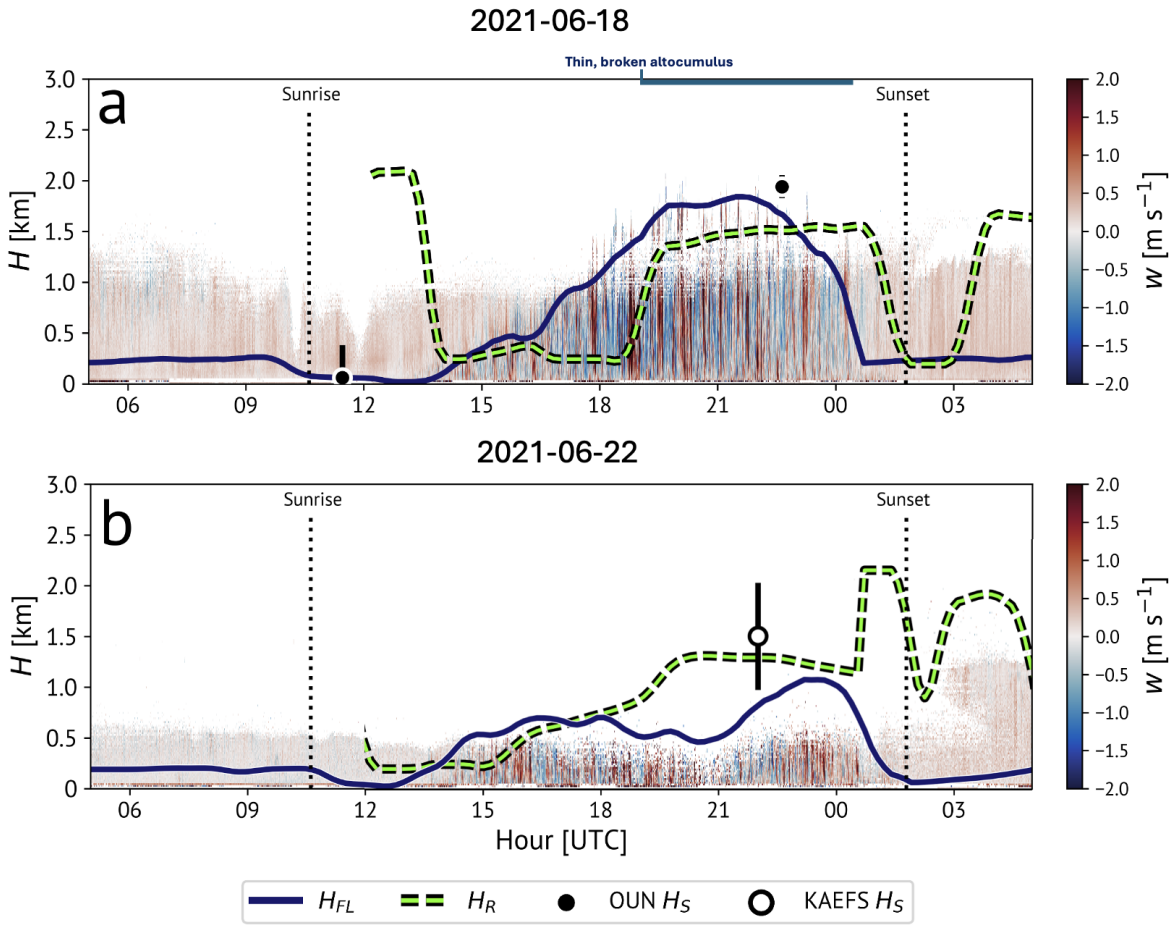


Figure 2.13: The three main H estimation methods (H_S for the sounding method, H_R for the radar method, and H_{FL} for the fuzzy-logic method) under mainly clear sky conditions (18 June 2021 0500 UTC - 19 June 2021 0500 UTC for Fig. 2.13a and 22 June 2021 0500 UTC - 23 June 2021 0500 UTC for Fig. 2.13b). The H_R (green dashed line), and H_{FL} (dark blue line) methods are overlaid on CLAMPS1 w observations, a crucial contributor in the first generation aggregation of H_{FL}. All H_S results are shown with circle markers (filled for OUN and open for KAEFS), and the black vertical lines associated with them represent the standard deviation of the techniques applied. Local sunrise and sunset times are shown with vertical dashed lines. The start of any period clouds first appear over all sites were denoted at the top of the plot by the types of clouds they were.

Figure 2.13 showcases time series plots from each of the three methods during clear-sky periods. From the BLISS-FUL dataset, we selected the two cases with the most

consistently clear conditions over the full 0500–0500 diurnal window; however, the first case, 18 June 2021 (Fig. 2.13a), included brief afternoon intrusions of altocumulus over the site. The H_{FL} measured 54 m at 1126 UTC just after sunrise, agreeing well with the radiosonde H_S measuring 60 m at that time. The H_R method had large discrepancies between H_{FL} that appeared random compared to H_{FL} evolving from the SBL to the CBL, indicating that H_R struggles even in the early hours of the daytime. By the time of the near-0000 UTC radiosonde launch, both methods produced lower H estimates than H_S. The individual radiosonde techniques were in great agreement (i.e., small standard deviation), suggesting a confident radiosonde H that the other methods seem to underestimate. Spotty areas of altocumulus were still present around this time making it possible for the gradient-based techniques to estimate higher than completely clear skies (see Table 2.4), but even $h_{\theta_v+0.6}$ was more elevated than H_{FL} or H_R. In terms of H_{FL}, this finding mimics those from Smith and Carlin (2024). They note that remote-sensing-based methods tend to underestimate H due to degrading instrument sensitivity with altitude. Rather than representing a single well-defined level, the ABL top is better characterized as a transition zone, and different retrieval methods may preferentially detect different parts of that layer (with remote-sensing approaches more likely to identify its lower boundary).

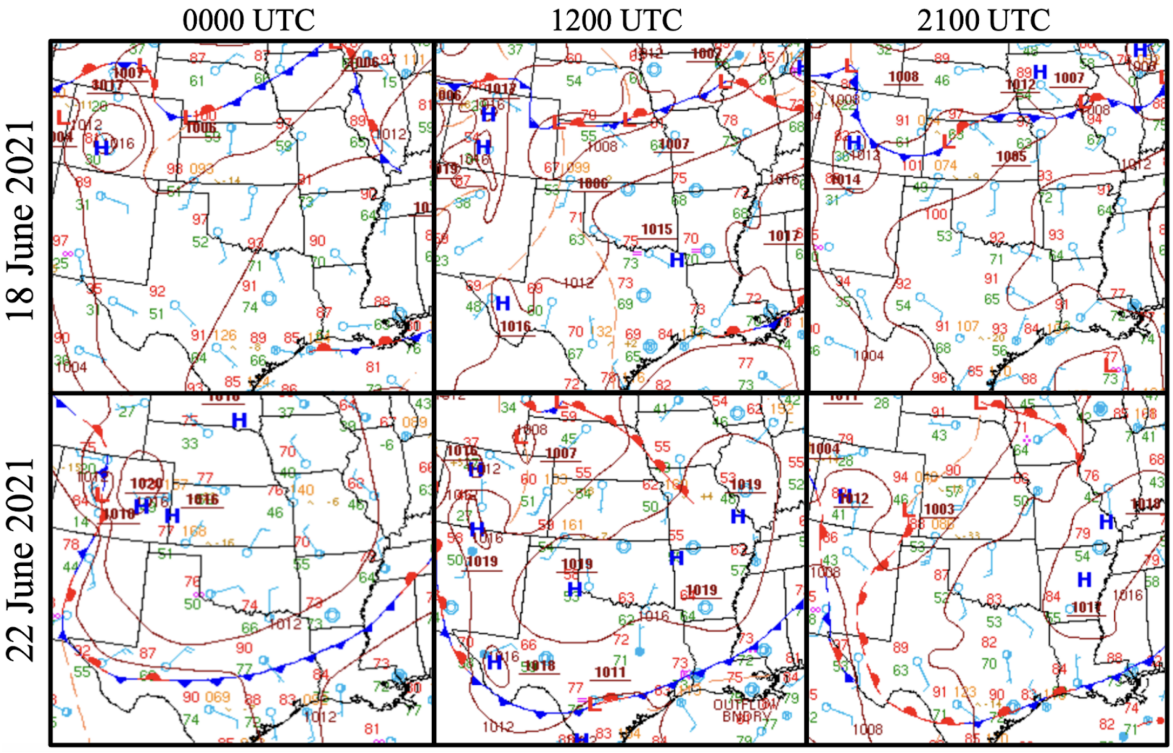


Figure 2.14: Surface synoptic maps from NOAA's Weather Prediction Center for 18 June 2021 (top row) and 22 June 2021 (bottom row) at 0000, 1200, and 2100 UTC.

The same pattern can be seen when comparing H_{FL} compared again with the afternoon H_S on 22 June 2021 in Fig. 2.13b (a morning sounding was unavailable in this case). On the other hand, the H_S matched nearly perfectly with H_R during this time, though there was a fair amount of disagreement (i.e., larger standard deviation) among the individual radiosonde techniques, where h_{RH} and h_q estimated at much more elevated heights and h_{BOT} much lower. Still, the growth of H_{FL} from 1800–0000 UTC seemed more stunted and less representative of the canonical clear-day ABL (e.g., Stull, 1988) compared to in Fig. 2.13a.

While the definitive state of the accuracy of H_{FL} or H_{RH} cannot be confirmed without consistent radiosonde observations throughout that entire period, the lower-level measuring of H_{FL} is related to limited aerosol backscatter following the cold front

passage that restricted the lidar's effective range, artificially capping the maximum H retrieval. As described in Smith and Carlin (2024), w data is a primary input for the fuzzy-logic algorithm as part of the initial H estimation process. Limited lidar signal depth limits the maximum H the algorithm can produce. A sparse or completely extinguished lidar signal can occur not only during rainfall, but also afterwards when precipitation removes much of the aerosol loads in the ABL, reduced aerosol loads leads to decrease in backscatter (unless aerosols are replenished by a distinct origin, such as industrial emissions). While the Fig. 2.13b case itself was devoid of clouds and precipitation, there was indeed rainfall observed from the KAEFS mesonet on the previous day, 21 June 2021, accompanied with a passing cold front. That front can be seen much further south on the case day of interest in Figure 2.14, resulting in a much different synoptic set-up associated with the 18 June 2021 case in Fig. 2.13a. Despite Fig. 2.13b's cloudless conditions well before the afternoon period, the storm system from the previous day may have dampened H_{FL} and led to strong disagreement across the individual sounding-based techniques (i.e., the cool, dry conditions associated with the post-frontal high pressure system may have increased ambiguity in moisture gradients, causing erroneously high h_{RH} and h_q values). While clear sky conditions are still the most optimal for assessing very different approaches to estimating H together, these lingering effects from frontal passages and precipitation events must be considered when using the fuzzy-logic algorithm.

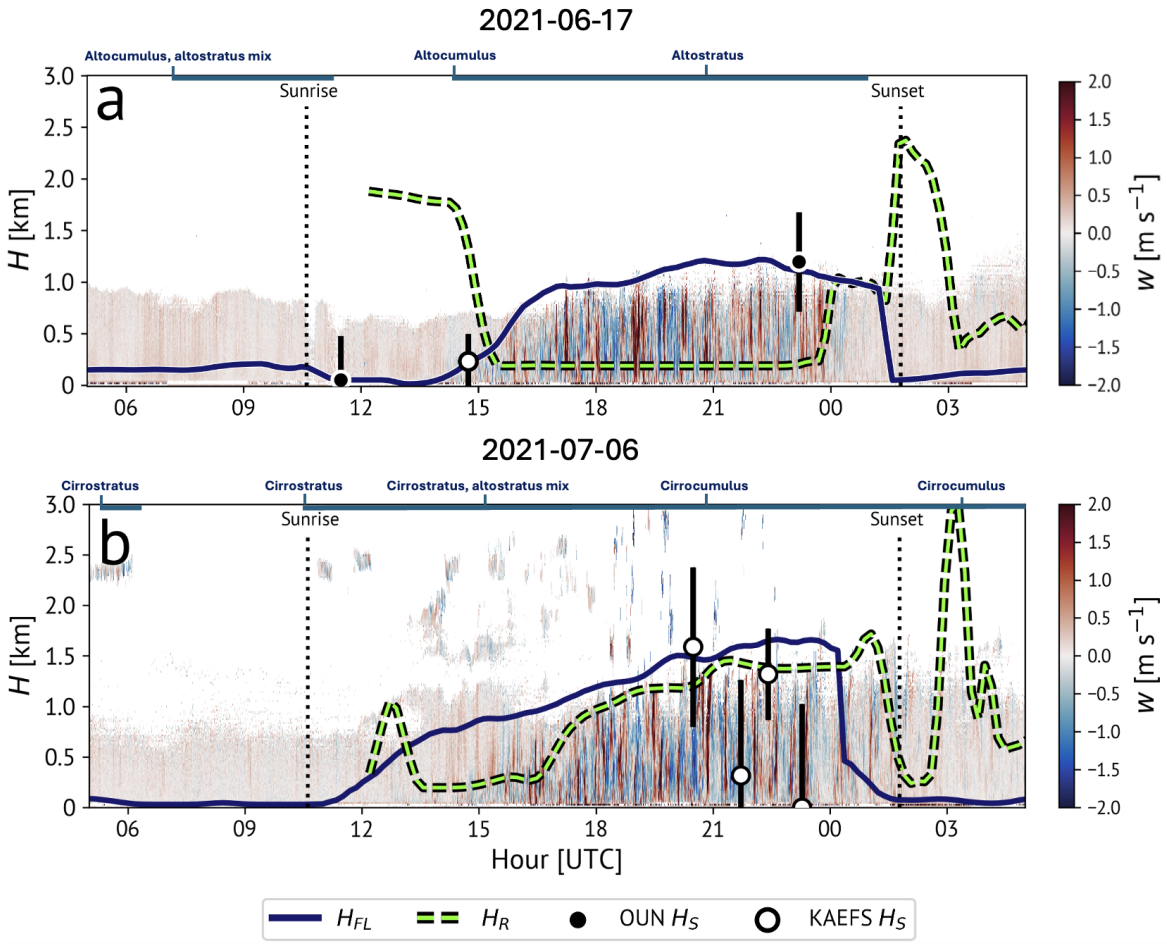


Figure 2.15: As in Figure 13, but for cases with few-partly cloudy conditions.

Further insight on H estimation under different atmospheric conditions can be drawn from cases where few-partly cloudy conditions prevail (Figure 2.15). On 17 June 2021 (Fig. 2.15a), three instances of radiosonde launches were available for analysis: two OUN soundings, and a KAEFS launch at 1446 UTC, presenting an opportunity to compare to the "true" H (i.e., radiosonde-based estimates) during the morning ABL transition. These three H_S estimates at 60, 240, and 1200 m, respectively, matched well with corresponding H_{FL} estimates of 81, 300, and 1036 m. Near 0000 UTC, H_{FL} slightly underestimated relative to the OUN H_S, but the difference was much smaller

than in clear-sky conditions and well within the spread of all radiosonde techniques.

Concurrently, H_R produced a questionable near-constant value around 200 m throughout much of the CBL. This artifact is hypothesized to be related to the H_R filtering thresholds applied here. The thresholds follow the established approach of Banghoff et al. (2018), which offers filtering practices that can serve as a standard for radar-based ABL retrievals. However, it is necessary to recognize that H_R may be subject to error if the filtering values for precipitation ($Z > 0$ dB and $\rho_{hv} > 0.8$) are too aggressive to detect Bragg scatter in some cases (e.g., Carlin et al., 2024; Stouffer et al., 2024). Initial work in Jordan et al. (2026) finds implementing $Z <$ -10 dB and $\rho_{hv} < 0.9$ offers little change to the removal of precipitation impacts on cases it occurred, but indeed better retains Bragg scatter information on days that are clear- to few- clouds. However, defining an optimal approach for H_R surpassed the goals of this work, so in this analysis, we chose to follow the procedures in Banghoff et al. (2018) to characterize H_R with avenues for exploring suitable, case-dependent filtering values in the future.

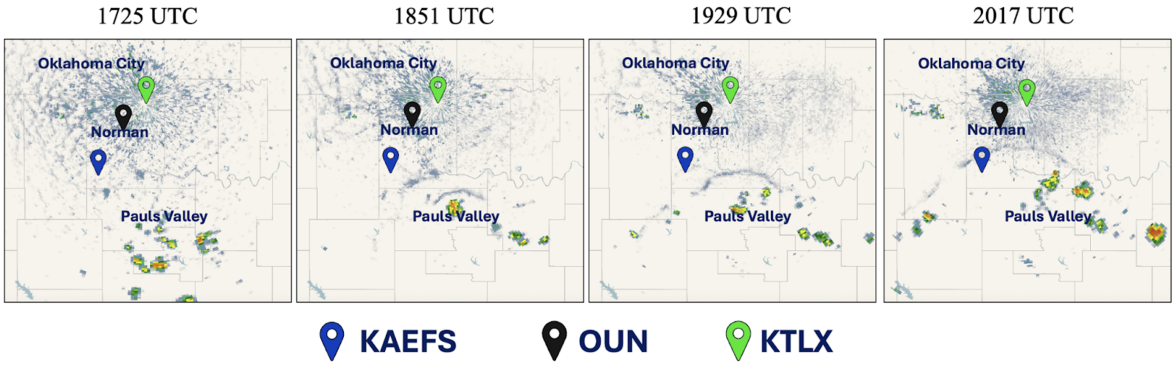


Figure 2.16: Radar imagery detailing the outflow from clustered thunderstorm cells near Pauls Valley, Oklahoma on 6 July 2021.

The second few-partly cloudy case, 6 July 2021 (Fig. 2.15b), provided a couple interesting points of analysis. While there were no high-resolution OUN soundings available

to analyze, there were four radiosondes from KAEFS released between 2000 UTC and 0000 UTC. A weak cluster of thunderstorms was ongoing about 140 km southeast of KAEFS, though they never moved directly over the BLISS-FUL sites. Both the H_S and the individual techniques produced sporadic estimates across the four soundings. The first and third soundings produced the most sensible H_S (based on similar atmospheric conditions from Fig. 2.15a), but H_S drastically dropped in elevation in the second and fourth soundings. Moreover, the spread between the techniques (i.e., the standard deviation) in all four radiosondes was large. Table 2.4 illustrates that large values in h_{θ_v} and $h_{\theta_v+0.6}$ K and small ones in h_θ and h_{BOT} were the culprits (outputs from the other techniques were mixed but overall produced a more consistent H). These variations can be tied to environmental shifts over a short period of time. Figure 2.16 outlines radar imagery of the storm cells, where outflow from the dissipation of at least some of them swept through the area shortly before the first sounding launch. This indicates a complex environment in which several techniques ended up contributing to uncertainty in the median, H_S. However, even in this environment, both H_{FL} and H_R were consistent and reasonable estimates throughout the afternoon.

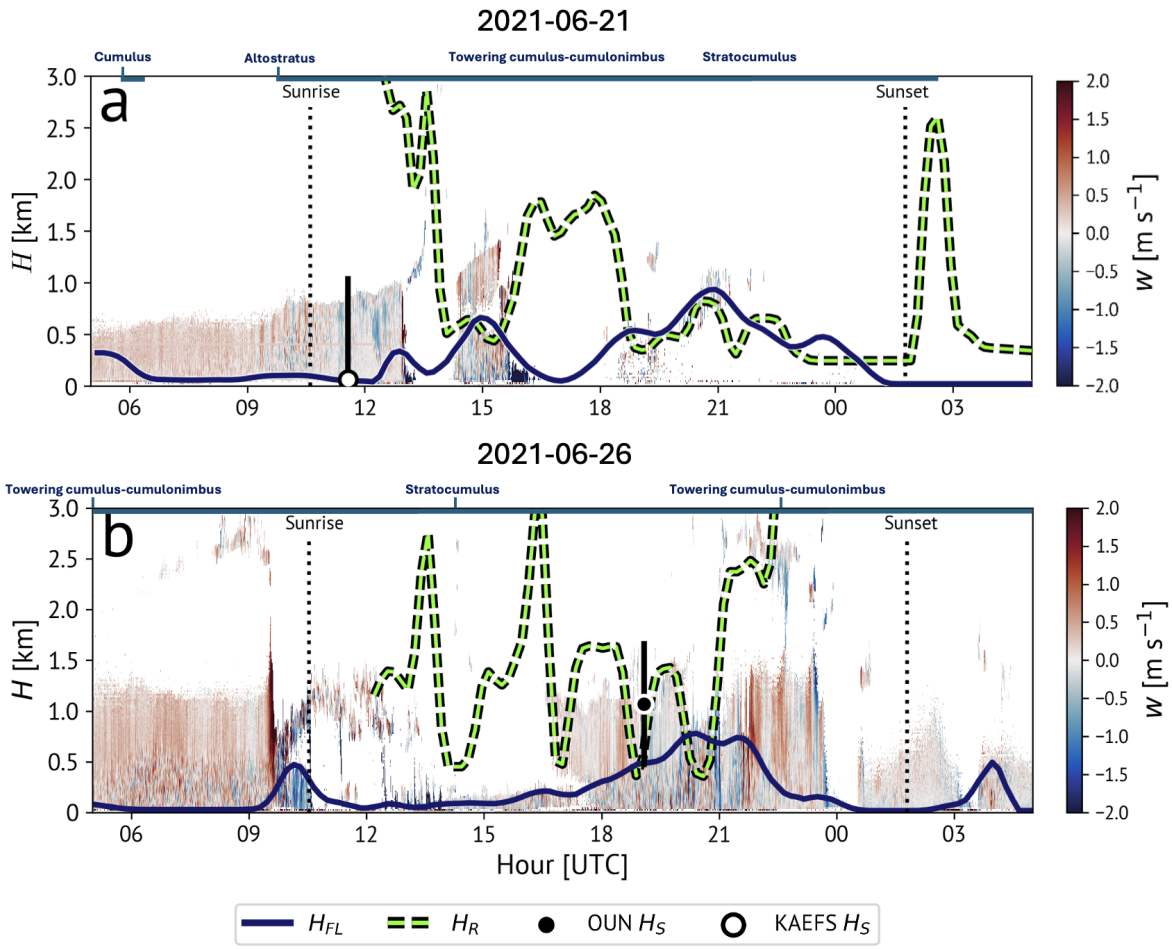


Figure 2.17: As in Fig. 2.13, but for cases with mostly cloudy-overcast conditions.

Given the different behaviors noted during complex conditions, the results from additional complex conditions related to rainfall are shown in Figure 2.17. On 21 June 2021 (Fig. 2.17a), the ABL was mostly clear until morning hours, when a storm system from the north swept into the area around 1200 UTC. The storm stretched completely over all sites (i.e., KAEFS, OUN, and KTLX) by 1500 UTC and remained overhead until roughly 2130 UTC, after which overcast conditions persisted until about 0300 UTC. Station data recorded periodic precipitation throughout the case (which can be inferred from intense downward w motions followed by lack of lidar returns). There was

only one available radiosonde during this time from KAEFS, and it produced a large range of estimates across the techniques with the shifting storm environment. However, the H_S itself aligned with H_{FL} as it had in previous SBL comparisons. Results during the CBL were more variable; between 1600 and 1900 UTC when the storm was active and overhead, H_{FL} decreased towards the surface while H_R peaked at 2 km. Yet, shortly after 1900 UTC, they converged back towards similar estimations. Once the system began moving out of the region, H_R seemingly recovered, at least for a few hours.

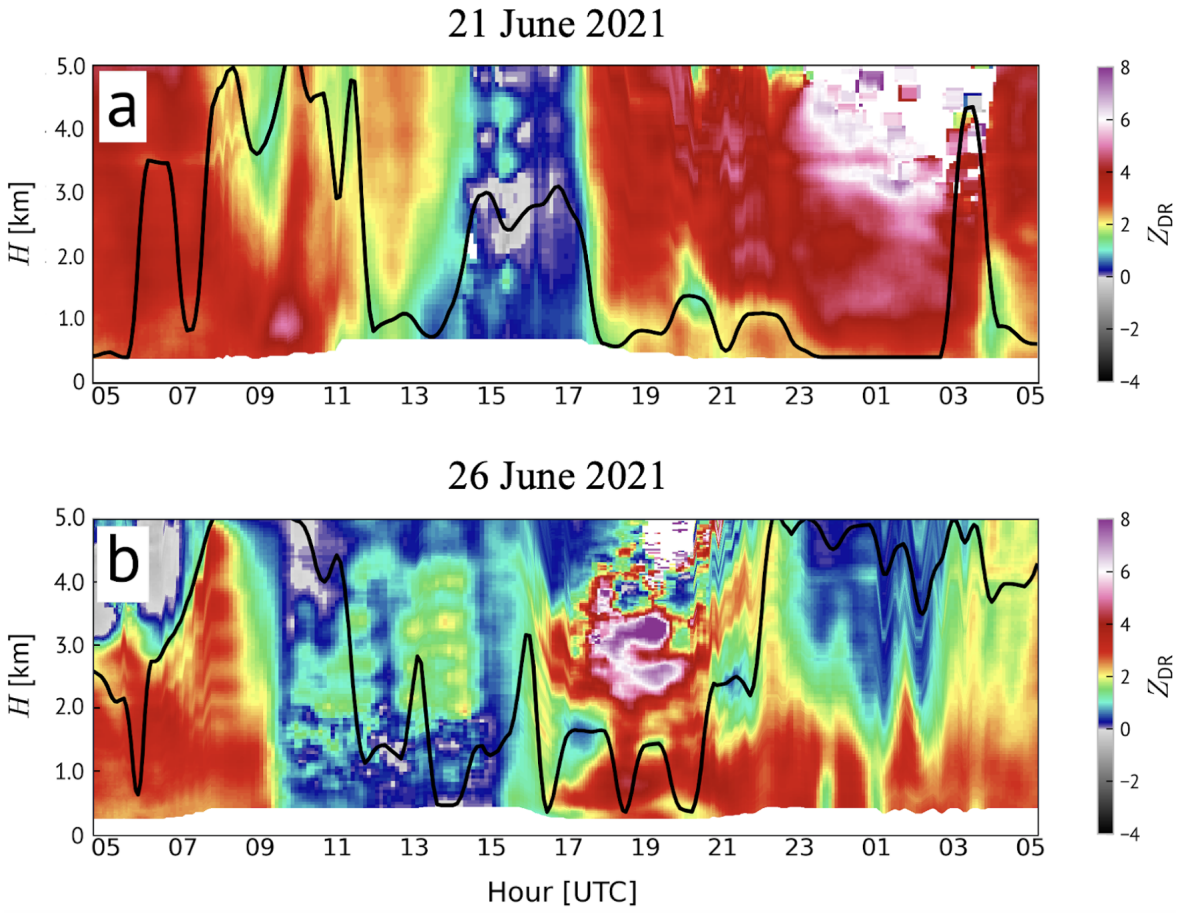


Figure 2.18: Radar QVPs of Z_{DR} values using the same cases from Figure 2.17 (21 June 2021 for Fig. 2.17a and 26 June 2021 for Fig. 2.17b). Note the difference in the y-axis range compared to previous figures to view the extent of the detected H_R, though it does still exceed this larger range at times.

It is impossible to say with certainty that either of the two continuous methods are good representations of H without radiosonde data. Therefore, 26 June 2021 (Fig. 2.17b) was another case that also experienced a storm passage but had an afternoon radiosonde launch available. There were pockets of heavy rain between 0900 and 1300 UTC while a squall line passed through, and the period that followed consisted of occasional periods of light rain. GOES-16 depicted heavy clouds during this time even when rain was not recorded. There was much more divergence in H_R in this case, which estimated abnormal heights near 5 km after 2200 UTC. This vertical extent of H_R during these cases is better seen in Figure 2.18, which shows QVPs of Z_{DR} used in the radar-based H estimation method. Here low, near-zero Z_{DR} indicates precipitation, which is aligned with the erratic H_R estimates.

Even during deep, convective conditions in the summertime, it is widely accepted that H rarely exceeds 3 km, deeming this a vast overestimation that should not be relied upon for fuzzy-logic comparison. However, the afternoon radiosonde matched fairly well with H_R during a brief period of increased Z_{DR} measurements, suggesting potential for the radar method to recover quickly post-precipitation events, with which H_{FL} struggles. Both Fig. 2.17 cases show the H_{FL} was prone to estimating at lower altitudes when precipitation was an occurrence. This discrepancy was not as pronounced on 21 June 2021 due to the agreement with H_R between 1900-0000 UTC. Alternatively, H_{FL} barely reached the height of even the lowest estimates from the afternoon radiosonde techniques on 26 June 2021. The lidar H_{FL} is contaminated by and can even completely vanish in rainfall, and the AERI is also limited in precipitation, meaning the fuzzy-logic algorithm has less input data (or degraded quality data) to rely upon.

The three-method comparisons provided necessary insight into H_{FL} performance across varying environments. The H estimates from all methods were least reliable when precipitation was actively falling, and the fuzzy-logic method, in particular, pro-

duced lower-than-expected estimates in the CBL even well after rainfall had ended (22 June 2021). This indicates that the fuzzy-logic algorithm can take time to recover as aerosol content that diminished from the precipitation had not yet replenished, which reduces the lidar's ability to penetrate high into the ABL. This is notable given that the 22 June 2021 case was otherwise nearly cloud-free, suggesting that sky conditions alone are not a strong controlling factor on fuzzy-logic performance. This is supported by the H_{FL} estimate on the 6 July 2021 case, which did not exhibit the same dampening in the CBL despite periodic clouds and a small decaying storm system nearby. Note that confidence in the 6 July 2021 H_{FL} estimate is somewhat tempered by inconsistencies in the radiosonde method on that day due to storm outflow, but the radar method producing quite agreeable estimates to H_{FL} provides some confidence in the fuzzy-logic estimation. Taken together, these findings suggest that H_{FL} is most reliably applied when precipitation has not occurred recently to the period of interest. Another similar path to be explored going forward is developing a criteria based on the range of w data available, which can also encompass periods of low aerosol content even without precipitation.

In terms of timing, the fuzzy-logic method seemed to falter most during the afternoon where it always underestimated compared to H_S, even if just slightly (the radar method also helped verify this by matching H_S on 22 June 2021), confirming results from Smith and Carlin (2024). Furthermore, the best consistent agreement regardless of sky condition occurred between H_S and H_{FL} during 1200 UTC launches, even if there was notable spread between radiosonde techniques. Coincidentally, the SBL is also when wind farm wake patterns tend to be most pronounced and persistent, so H_{FL} operating efficiently during this time is useful to consider going forward.

These findings illustrate the suitability of the fuzzy-logic method as an H estimator, especially for wind farm research. The in-situ abilities of radiosondes allows them to

capture localized conditions sampled along each flight path, allowing the radiosonde method to effectively serve as a true H measure here, but their rapid ascent and susceptibility to horizontal drift is not ideal for characterizing wind farm wakes. The radar method scans observations from a fixed location and, like the fuzzy-logic method, performed well in the CBL under precipitation-free conditions, but dual polarization scans over such a large domain could compromise finer-scale features like wakes. The fuzzy-logic method can collect high-quality ABL information from stationary instruments, and its demonstrated skill under optimal conditions, combined with these observational characteristics, makes the method a strong candidate for accurately representing wind farm impacts on ABL depth.

2.3.4 Identifying Mixing Signatures in ABL Lidar Profiles

Having established that WINDoe and the fuzzy-logic method can reliably characterize the ABL, a remaining question not yet addressed is how well the underlying ABL profiles used in them can resolve fine-scale mixing associated with wind farm wakes. Datasets of σ_w are central to the upcoming analysis, as they provide a means to identify rotor-layer turbulence enhancements attributable to farm effects. Additionally, the w measurements from which σ_w derives were shown in the previous section to be a key parameter in fuzzy-logic H estimating capabilities. As such, ensuring that the systems we employ can capture mechanically-generated mixing from nearby infrastructure is an important prerequisite for the wind farm analysis to follow. This goal can be accomplished by using CLAMPS data from PBLTops, a campaign where the platforms were deployed in similar rural-like settings close to the instruments but differed substantially spanning out from them.

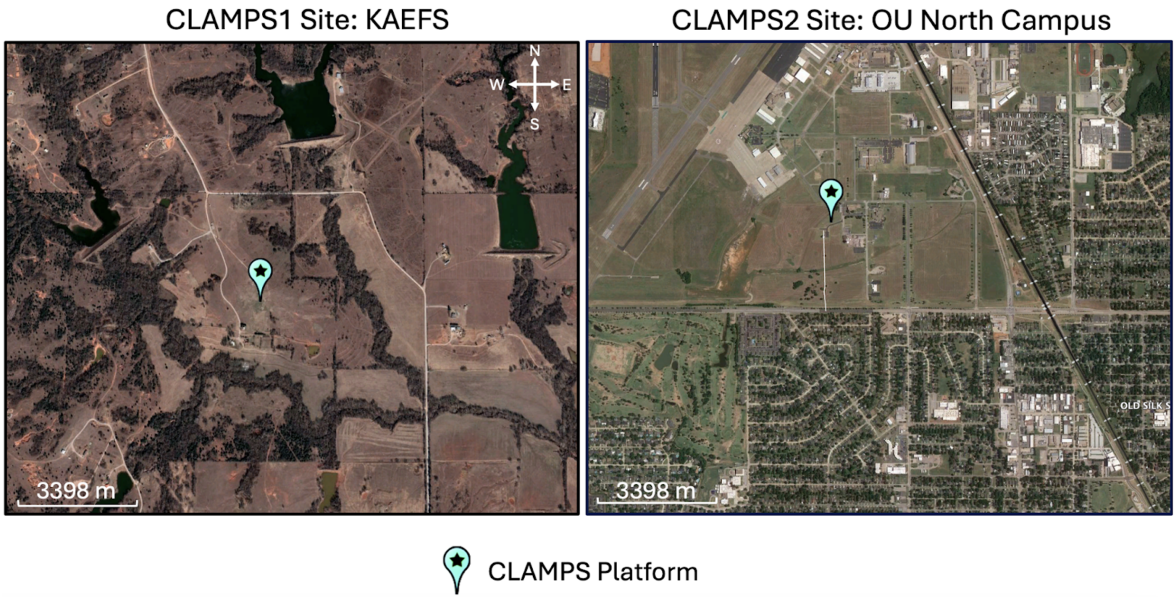


Figure 2.19: Map from Fig. 2.3 KAEFS and OU North Campus maps zoomed out in view to better view the surroundings of the two sites.

During PBLTops, the CLAMPS were positioned approximately 30 km apart, operating with the consistent scanning strategies. CLAMPS1 was placed at KAEFS while CLAMPS2 was deployed at OU's North Campus, which is two miles north of the OU main campus (left and right panels of Figure 2.19, respectively). South of CLAMPS1 at KAEFS, a grove of trees and vegetation runs horizontally across the site, while south of the OU North Campus lies the developed residential infrastructure comprising the north side of Norman, Oklahoma, which goes on to stretch much further south. To the northwest, the OU North Campus faces scattered development associated with the Max Westheimer Airport, whereas the KAEFS northwest sector is comparatively open, with only a small pond directly north of the instrument and little additional terrain complexity. Together, these differences make the town infrastructure south of OU's North Campus the primary source of mechanically-driven mixing in this analysis, serving as a proxy for the rotor-layer mixing that wind farms would provide in

the AWAKEN setting. Under northwesterly flow, neither site is expected to exhibit strong mixing signatures. If that pattern is detectable in σ_w profiles, it would build confidence in the instruments' ability to resolve wind-farm-driven mixing going forward. Note that while the tree grove south of KAEFS in Fig. 2.19's left panel may contribute modestly to turbulence, its effect is expected to be much smaller than that of the urban surroundings at the Norman site.

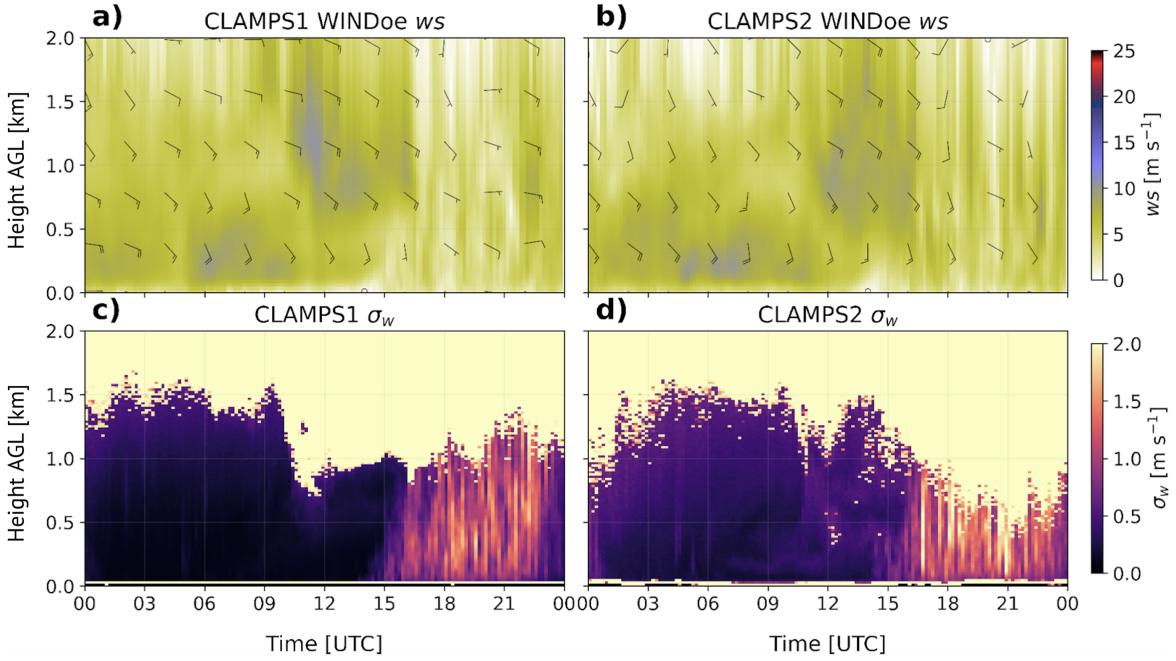


Figure 2.20: Time-height cross-section of CLAMPS1 and CLAMPS2 10-minute WINDoe-derived winds (Figs. 2.20a and 2.20b) and 10-minute σ_w with no SNR-filtering applied (Figs. 2.20c and 2.20d) during the PBLTops campaign on 25 August 2020.

The *wd* was predominantly southerly throughout the period, representative of the winds typically observed in the region. The wind profiles as a whole measured relatively similar over the sites despite a distance of ∼30 km (Figs. 2.20a–b), a useful point of reference for the similar distance of CLAMPS spacing during AWAKEN. Though winds agreed at both sites, the corresponding σ_w revealed notable differences between

the two datasets across the profile depth (Figs. 2.20c and 2.20d). Both lidars captured characteristics that arose from wind-based effects (e.g., strong signatures ∼0500 UTC in the first 500 m when the NLLJ strengthens, or ∼1200 UTC above 500 m where higher ws is measured), but σ_w magnitudes were larger from CLAMPS2. This behavior was consistent across the full 21 August to 3 September 2020 period, even as ws from the two platforms remained in close agreement. Given the site locations, this σ_w discrepancy was expected. For even deeper scrutiny, the full PBLTops dataset was therefore separated by wd and stability regime to determine whether the offset persisted.

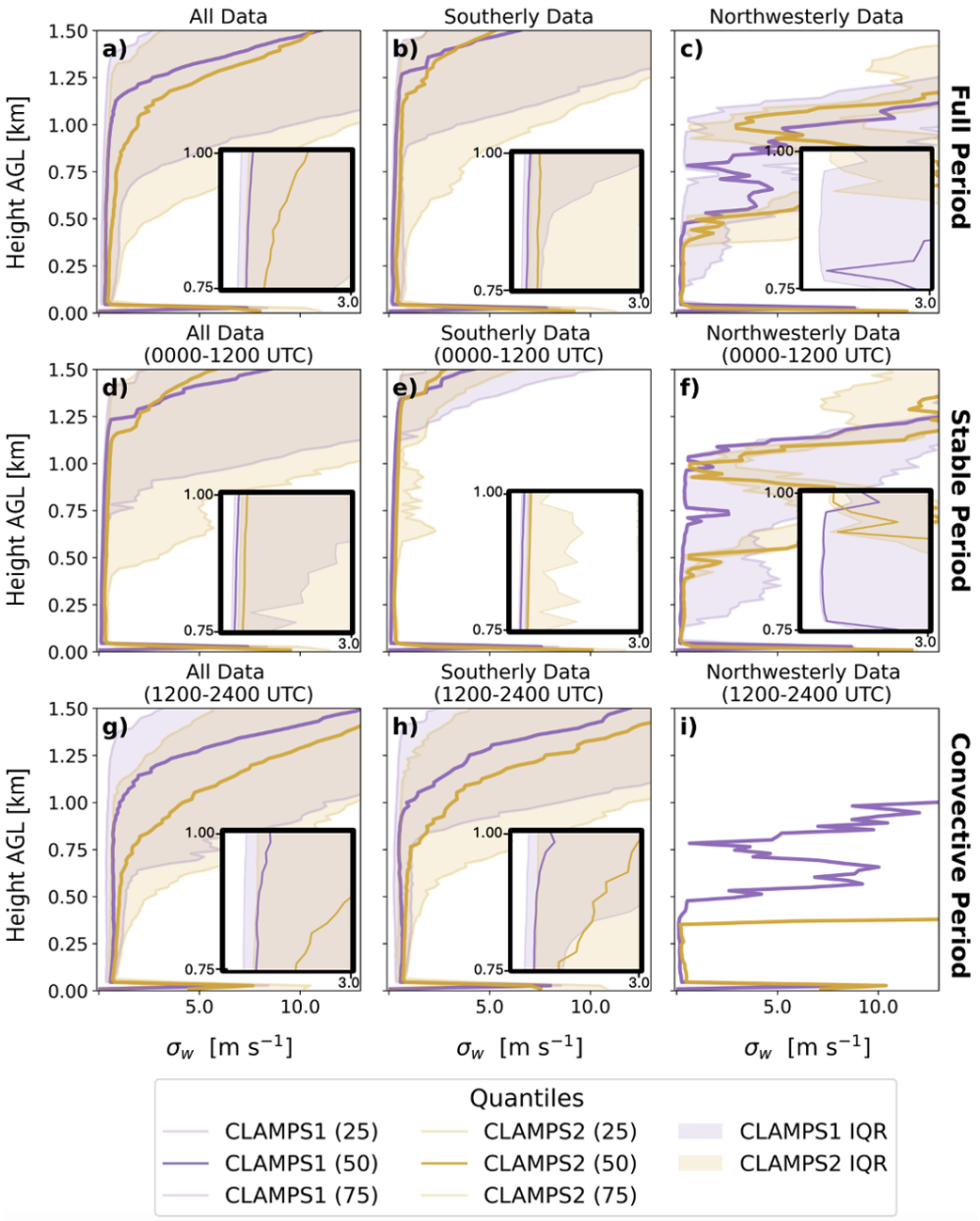


Figure 2.21: PBLTops percentiles of σ_w throughout the full diurnal cycle for all available data (Fig. 2.21a), only southerly data (Fig. 2.21b), and only northwesterly data (Fig. 2.21c). The same approach is employed but only for the SBL (Figs. 2.21d-2.21f) and only for the CBL (Figs. 2.21g - 2.21i). The 50th percentile served as the mean measure, while the 25th and 75th percentile served as left and right outer bounds, respectively. To compare usable measurements not contaminated by noise, zoomed-in versions of each panel from a 0-3 m s^{-1} x-axis and 0.075-1.0 km y-axis are shown at the right of their original version, except for Fig. 2.21i where the data was not within the inset map bounds.

Figure 2.21 shows percentiles of σ_w from the two CLAMPS under different wd and throughout the full 24-hours, stable conditions, and convective conditions. Only timestamps where both w and WINDoe data were available were implemented. When considering all times in the diurnal cycle (Figs. 2.21a-2.21c), the σ_w profiles mimic the behavior as the Fig. 2.20 southerly case, where the CLAMPS2 values were generally larger. This is notable since southerly winds made up the majority of PBLTops (both CLAMPS observed southerly flow at most range gates in the profile approximately 49% of the time). Similar differences could be identified under northerly flow conditions during the full period and stable conditions (Figs. 2.21c and 2.21f), judging by the CLAMPS1 50th percentile briefly exceeded that from CLAMPS2 around 1 km. Data from the northwest was limited during the CBL (Fig. 2.21i) and CLAMPS2 data was not available above 0.75 km, the lowest range of usable data. In fact, northwesterly data only represent 0.3% of the dataset, so we expanded the sector to all northerly data (not shown) and found the difference to decrease but CLAMPS2 σ_w was still stronger. This information supports the notion that the lidar can resolve low-level mixing quantities from adjacent obstacles, even if said obstacles are not in the immediate vicinity.

Though there were not apparent systematic differences in the σ_w quantity itself, it should be noted that lidar data recurring differences in the altitude at which each lidar transitions to noise as SNR decreases, indicated by the abrupt increase of σ_w to $\gtrsim 1.5$. This behavior is consistent with signal degradation at low SNR, where the lidar return becomes sufficiently weak that the velocity estimates are dominated by noise rather than atmospheric signal, and that is interpreted here as a noise floor threshold rather than a physical turbulence feature. The vertical extent of reasonable CLAMPS1 data surpassed those from CLAMPS2 in all Fig. 2.21 panels, with the exception of the northwesterly samples (when including all northerly data, the same pattern as the rest of the samples occurred). This information suggests lower sensitivity from

the CLAMPS2 lidar than CLAMPS1, which can be accounted for in the wind farm analysis by applying stronger SNR filtering on the CLAMPS2 lidar that adequately removes noisy data.

Aside from this difference in returns aloft to consider, distinct surface characteristics associated with Norman's built environment (buildings, roads, and houses) was reflected as enhanced σ_w profiles, demonstrating that the CLAMPS lidars are capable of resolving fine-scale turbulence enhancements from upwind obstacles. This understanding of the lidar capabilities will be carried into the AWAKEN analysis, where the absence of major infrastructure or tall vegetation near either CLAMPS site lends greater confidence that detectable σ_w differences between the platforms reflect genuine wind-farm-driven signals.

2.4 Chapter Summary and Implications

An assessment was conducted into the performance of newly developed algorithms and their input datasets to determine how reliable each is when applied for studying mixing effects from northern Oklahoma wind farms. This was done using high-resolution observations from past field campaigns within the north and central Oklahoma region but in areas free of wind farms to isolate other sources of discrepancies from the algorithms or instruments. Such information revealed favorable scan strategies and instrument diagnostics to consider going forward.

Using LABLE I campaign data from two co-located lidars of different scanning strategies (one from ARM-CF, one from OU that eventually becomes a part of CLAMPS1), the WINDoe algorithm was found to efficiently fill gaps in wind profiles while agreeing well where VAD data was available. This aligned with work from Baidar et al. (2023) and Gebauer and Bell (2024) using only the ARM-CF lidar. There were

more discrepancies between the two methods in the daytime than nighttime; conditions in the CBL often do not adhere to the horizontal homogeneity condition associated with VADs, but the retrieval process of WINDoe limits discrepancies originating from that condition. Furthermore, scan geometry directly shapes WINDoe performance because elevation angle determines the slant range at which the beam intersects a given altitude. Steeper angles reach that level closer to the instrument, preserving SNR but projecting weakly onto the horizontal plane, while shallower angles sample horizontal flow more directly but lose signal at lower absolute altitudes. The OU lidar, scanning the two elevation angles sequentially showed ws uncertainty to emerge at lower altitudes than from the ARM-CF's single 60° elevation angle, a consequence of combining retrievals from two geometrically distinct scan cycles. A single elevation angle near 70° was determined to be the best fit for the application goals of WINDoe to fully resolve the NLLJ.

The second algorithm, the fuzzy-logic H algorithm, was shown to perform best under stable conditions without recent rain or a lot of cloud cover. Nighttime hours were particularly favorable, during which H_{FL} yielded little-to-no difference whether its wind inputs were derived from WINDoe or VADs. The main instance that was found to degrade the quality of H_{FL} was the absence of high temporal resolution w data from the lidar's vertical staring mode. Fortunately, the ARM-CF w datasets are available at a sufficient temporal resolution throughout all the years of interest, and this is a common operating mode for CLAMPS, with AWAKEN being no exception. Given the direct implementation of the vertical stares data for analyzing low-level wind farm mixing, we inspected CLAMPS σ_w as a means to assess the lidar's ability to quantify mechanically-generated turbulent mixing from nearby structures. This was evaluated using data from a campaign setup analogous to where CLAMPS will be positioned in AWAKEN. There were notable enhancements in σ_w collected just north

of Norman, Oklahoma, even when ws were similar at both sites. The CLAMPS2 lidar was found to operate with lower receiver sensitivity (i.e., lower pulse energy) than the CLAMPS1 lidar, measuring a shorter effective range under equivalent atmospheric conditions that necessitates strong SNR filtering going forward. Despite this, the data from both systems below that ceiling remained consistent in capturing the stronger mixing signatures associated with the upwind urban surface roughness of Norman

Results from these comparisons and evaluations establish trust that the algorithms and observations are well-suited for analyzing wind farm effects. These findings offer a baseline reference that will support the analysis to understand how high-quality datasets and newly-developed algorithms together improve the understanding of wind farm impacts on the northern Oklahoma ABL. The outcomes of the tests in this chapter will be referenced as needed moving forward into the wind farm analysis.

Chapter 3

Wind Farm Effects on Low-Level Mixing

The recent and rapid development of several wind farms across northern Oklahoma raises important questions regarding their local environmental impacts in the region. A widely used approach for assessing these impacts involves examining turbulent mixing, or wakes, generated behind and downstream of wind farms as turbines extract kinetic energy from the flow above them (Tennekes and Lumley, 1972; Lissaman, 1979). As demonstrated in studies such as Christiansen and Hasager (2005), Wharton and Lundquist (2011), and Hirth et al. (2013), among others (see Chapter 1), identifying these wakes is generally a straightforward method for linking atmospheric alterations to wind farms. However, the northern Oklahoma ABL contains additional features that can independently drive near-surface mixing, complicating the ability to identify of turbulence driven solely by wind farm activity. Among these is increased nocturnal *ws* associated with the frequently-occurring NLLJ. Although the NLLJ is seen as a rich resource for providing winds from which turbines can extract energy, it is still unclear how variability in NLLJ strength and height influences the production or identifiability of wakes.

To understand how wind farms impact the ABL, it is first necessary to identify low-level mixing within the rotor layer that previous studies have attributed to turbine

activity and to determine whether such signals remain detectable in the presence of a prominent NLLJ. To do this, we compare environments with and without nearby wind farms. During the 2022-2024 AWAKEN campaign, two CLAMPS facilities were deployed to collect observations, with one located near wind farms with dense clustering of turbines and the other situated within the broader domain but well outside the expected influence of turbine-induced mixing. Another source of comparisons originate from the ARM-CF site, which offers data spanning 2011-2023, enabling samples from many years both before and after a nearby wind farm with row-like configurations was built to the south. The site has shown to receive impacts from that farm during southerly flow (Krishnamurthy et al., 2021b; Bodini et al., 2021), but the observations were not tested with considerations of the NLLJ, especially from a seasonal perspective, where the jet can vary drastically.

The goal of this chapter is to explicitly account for the role of the NLLJ when evaluating wind farm-induced mixing in the lower atmosphere, which is required to proceed into an investigation on their effects throughout the full ABL. Given the demonstrated performance of the WINDoe algorithm in fully characterizing NLLJs in Chapter 2, it is applied here to identify NLLJ characteristics across the study periods and to assess how clearly low-level mixing can be detected under different jet strengths. This analysis is further refined by applying a method for determining thresholds of shear-driven turbulence (Bonin et al., 2015), which provides a clear-cut means of distinguishing whether observed low-level mixing originates from wind farms or from external atmospheric drivers.

3.1 Methods

3.1.1 Study Design and Scope

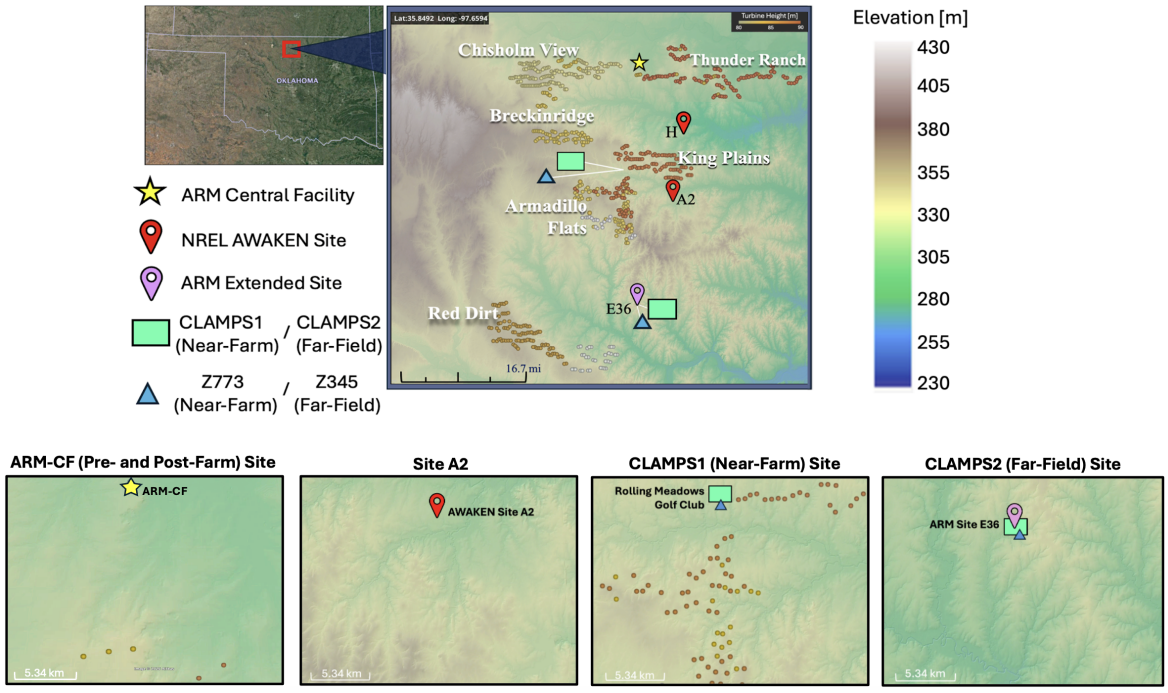


Figure 3.1: Satellite view of Oklahoma (top left; Google Earth) with a zoomed in version of the AWAKEN domain showing terrain elevation information (top right; Google Earth, with elevation information from OpenTopography and turbine latitudes and longitudes from the U.S. Wind Turbine Database). Marked locations represent AWAKEN observation sites referenced in this work. Locations of ZephIR 300 profiling lidars represent only the winter campaign, after which they were relocated elsewhere. Light gray symbols south of E36 mark turbines that were under construction and not yet operational during the deployment of CLAMPS and the profiling lidars. The bottom panels are further zoomed-in maps of the sites of interest for the study.

The AWAKEN domain is mapped out in Figure 3.1, showing wind farm locations, elevation information, and all sites relevant to the science goals going forward. This includes ARM-SGP extended sites and a couple of sites used by NREL during AWAKEN. For

a comprehensive overview of all AWAKEN sites and their deployed instrumentation, see `https://a2e.energy.gov/project/awaken`; of relevance here, sites north of wind farms were prioritized as downwind locations, consistent with the SGP's predominantly southerly climatological flow (Krishnamurthy et al., 2021b).

The ARM-CF analysis was conducted in the context of the nearby Thunder Ranch wind farm, which became operational in December 2017. This allowed ARM-CF during 2011–2017 to serve as the environment without wind farm effects (pre-farm), and within a wind farm regime in 2018–2023 (post-farm). The ARM-CF site is equipped with power access the instruments require, and it is located without complex surfaces or blockages that might obstruct the measurement capability of the instruments. Sites of similar capacity were sought out when designing the deployment strategy for CLAMPS. For situating one of the CLAMPS platforms close to a wind farm (hereafter, the near-farm site), we chose Rolling Meadows Golf Club east of Enid, Oklahoma. This spot was picked because of its downstream proximity to the Armadillo Flats wind farm to the south and King Plains to the north, as well as offering favorable placement for power availability and little vegetation or built structures. The site is located 1.9 km southwest of the closest turbine at King Plains and 2.2 km north of the closest turbine at Armadillo Flats. CLAMPS1 was deployed on the eastern edge of a golf course (36°22'46.7"N 97°31'24.4"W) from 3 October - 21 December 2022. The platform returned to this location to continue a summer deployment of AWAKEN from 1 July - 28 September 2023.

The CLAMPS2 facility was intended to observe undisturbed ABL flow representative of the AWAKEN domain while specifically avoiding wind farm influences. ARM-SGP's extended facility E36 (36°07'01.7"N, 97°26'15.9"W) best suited this goal and provided power supply with little vegetation or structural obstacles as desired. CLAMPS2 was deployed at this site during roughly the same periods as CLAMPS1 (3

October – 28 December 2022 and 23 June – 1 October 2023), enabling direct comparisons between the two systems. E36 is situated approximately 20 km east-northeast of the nearest turbine at the Red Dirt wind farm and 12 km south of the nearest turbine at Armadillo Flats. Another wind farm was under construction southeast of Red Dirt during AWAKEN, denoted by the light gray dots in Fig. 3.1, but it was not operational until 2024 (U.S. Geological Survey, 2026) after both CLAMPS were removed and is therefore assumed not to impact far-field measurements.

The wind farm layouts differ notably between Thunder Ranch south of ARM-CF and Armadillo Flats south of the AWAKEN CLAMPS1 site. The Thunder Ranch turbines near ARM-CF are oriented in a row-like formation. There are three turbines directly south of the site with a hub-height of 80 m (rotor diameter = 116 m, rotor sweep = 22–138.1 m), and the turbines extending further east in the rest of that row are 90 m (rotor diameter = 116 m, rotor sweep = 32–148.1 m). Further south, Armadillo Flats contains a few turbines at 80 m hub-height (rotor diameter = 100 m, rotor sweep = 30.1–130.1 m) but most of the turbines measure hub-heights of 90 m (rotor diameter = 116 m, rotor sweep = 32.1–148.1 m), especially closest to the CLAMPS1 site. Armadillo Flats consists of more densely-grouped turbines than ARM-CF's row design, meaning flow passing through Armadillo Flats encounters multiple turbine wakes before reaching the CLAMPS1 site, whereas waked flow at ARM-CF derives from only a few turbines at most. While a detailed investigation of how wind farm layout influences its produced mixing is beyond the scope of this analysis, these differences are worth keeping in mind: even if both ARM-CF and CLAMPS1 show evidence of wind farm influence, that influence is hypothesized to be considerably larger at the CLAMPS1 near-farm site with more densely-grouped turbines.

3.1.2 Instrument Configuration and Data Availability

Across all three facilities, the ARM-CF, CLAMPS1, and CLAMPS2, operate Halo Streamline model lidars that collect high-resolution 1-second fixed-beam vertical stare data continuously except when PPIs are performed. At ARM-CF, instrument settings evolved during the first few years of operation. During most of 2011, PPI scans were hourly using 72 discrete azimuth angles at an elevation angle of 24° (Newsom, 2012), but the angle increased to 40° in December 2011. By mid-August 2012, the PPI elevation angle increased again to 60° with 8 evenly-spaced azimuths and was scanned every 10-15 minutes (Newsom and Krishnamurthy, 2022). The adjusted lidar configuration also increased the maximum range gate beyond 4 km (compared to 2.5 km prior to 20 August 2012), depending on available targets. These settings remained through the rest of the ARM-CF years analyzed here, but the lidar was upgraded in May 2016 from a Streamline Pro to a Streamline-XR model. This upgrade changed the sensitivity of the lidar system, and to keep data consistent for the entire period of analysis, data collected before the upgrade were processed with a higher SNR limit. When applying the WINDoe method, user settings are configurable in an input file (i.e., a VIP file); for the ARM-CF PPIs, settings are listed in Table A.1 in Appendix A.

The thermodynamic-based optimal estimation algorithm, TROPoe, is routinely applied to ARM-CF AERI observations and the outputs are readily available from ARM-CF's online data archives (`https://adc.arm.gov/discovery/results/instrument_class_code::tropoe`). The retrievals incorporate cloud-base height information from a co-located ceilometer, as well as surface conditions from a co-located 2-m surface meteorological instrumentation. The TROPoe package version used to process the data was updated in October 2017 from v0.11 to v0.9, which mainly consisted of minor bug fixes and streamlined code improvements.

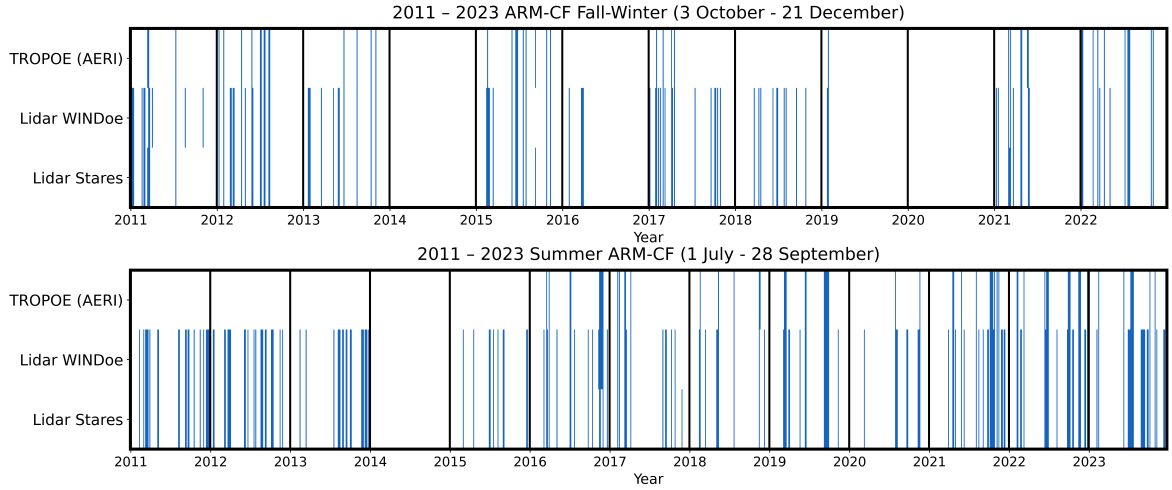


Figure 3.2: Time series of full ARM-CF lidar data 2011-2023 summer and fall-winter periods filtered for data quality. Each bar is representative of a single 24-hour case.

The ARM-CF analysis targeted seasonal periods to inspect results under different ABL regimes over the longer time period (pre- and post-farm). ARM-CF cases from the same months of the 2022 and 2023 AWAKEN CLAMPS deployment were used; specifically, 29 September - 21 December made up the fall-winter period, while 1 July - 28 September represented summer. A timeline of ARM-CF lidar data used for this study is available in Figure 3.2. The data were inspected both through quality control flags available in the files and through manual evaluation of time-height cross-sections. ARM-SGP routinely maintains and quality controls both the lidar (Newsom and Krishnamurthy, 2022) and AERI (Riihimaki et al., 2019), but any additional suspect data were identified and flagged for removal during periods of irregular measurements or contaminated data due to instrument issues.

The AWAKEN data analyzed here came from periods when both CLAMPS operated at their respective sites. Their lidars collected 10-minute PPI scans with 8 azimuth sweeps lasting around 30-35 seconds, operating at an elevation angle of 70° (CLAMPS1 conducted 15-minute PPIs with 10 azimuths during the 2022 fall-winter deployment).

The same WINDoe settings used for the ARM-CF PPIs were also applied to the two CLAMPS platforms. Thermodynamic information was produced with the TROPoe algorithm. Cloud-base height and surface meteorology came from CLAMPS lidar vertical stares and meteorological stations, respectively. Recalling that the CLAMPS platforms contain two thermodynamic profilers, AERI- and MWR-derived retrievals were produced when data from those instruments was available. The resulting TROPoe outputs were similar between the two instruments, except the MWR retrievals had a coarser effective resolution and larger uncertainties due to the reduced information content of passive microwave observations compared to infrared spectroscopy. The CLAMPS data availability is shown in Figure 3.3.

Due in part to delayed CLAMPS maintenance given an atypical string of back-to-back field campaigns due to SARS-COVID-19 delays, there were unfortunately several instrument malfunctions during AWAKEN. During both seasons, the CLAMPS1 MWR did not operate, and the CLAMPS2 AERI experienced several outages. Toward the latter portion of the summer campaign, the CLAMPS2 AERI would occasionally power down automatically near the end of the day and required a manual reboot, and the lack of data from these instances are also reflected in Fig. 3.3. Lidar data availability during the winter campaign was periodically partially-to-fully obstructed due to dew or fog related condensation on lidar lenses and instrument moisture seal issues. During the summer campaign, the CLAMPS1 lidar's azimuthal encoder was unable to detect the scanner's relative position in azimuth and therefore unable to provide wd information (after the summer campaign, this problem was identified as internal lubricant obscuring the home position beacon, which was introduced during manufacturer repairs performed prior to the deployment). As such, wd data at the near-farm site are only directly available during the winter campaign. The issue did not impact the CLAMPS1 ws. With secondary information (i.e, matching to similar observations from

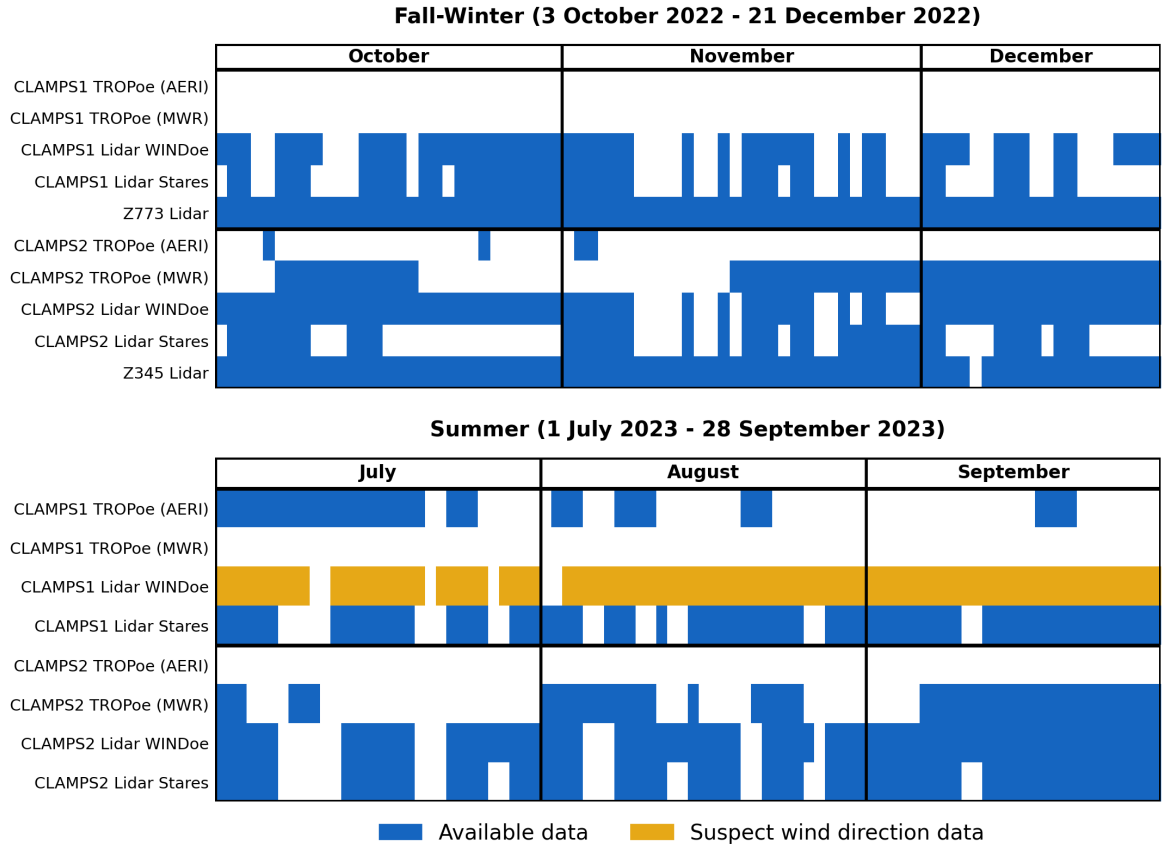


Figure 3.3: As in Figure 25 but for AWAKEN data. Only time ranges where data from both CLAMPS were available are shown. As with the ARM-CF data availability, each bar is representative of a single 24-hour case.

nearby AWAKEN sites), *wd* can be estimated. For the summer campaign, CLAMPS1 *wd* is inferred using CLAMPS2 data. As in ARM-CF data, we removed contaminated measurements, such as periods where condensation formed on the CLAMPS lidar lens, weather conditions like precipitation, or any other suspect data.

Fig. 3.3 also lists the availability for two additional platforms operating at the CLAMPS sites during the 2022 fall-winter. Lawrence Livermore National Laboratory (LLNL), an AWAKEN collaborator, deployed two ZephIR 300 profiling lidars to measure 1-second *ws* in the lowest 200 m. One (lidar number 773, Z773 in Fig. 3.3)

was positioned alongside CLAMPS1 at the near-farm site, and another (lidar number 345, Z345) was located with CLAMPS2 at the far-field site. The high-resolution profiling capabilities of Z773 and Z345 allowed LLNL to target high frequency statistical observations encompassing the full rotor disk height of targeted wind farms (data specifics available in B.1 in Appendix B). After 2022, the lidars were moved to different AWAKEN sites to support a dedicated wake study enacted for the King Plains wind farm, but their placement alongside CLAMPS complemented the VAD retrievals. Since PPIs produce a blind zone effect in the lidar's lowest range gates, the profiling lidars helped fill this gap by resolving *ws* near the surface (see Figure B.1 in Appendix B).

More recently, WINDoe processing has been applied to the CLAMPS lidar PPIs, providing extended coverage. However, the performance of WINDoe remains uncertain without comparison to independent observations. Such evaluations were conducted at several heights throughout the ABL in Chapter 2, but in the absence of direct measurements within the lowest range gates, WINDoe relies primarily on layer-to-layer correlations and information from the climatological prior.

Technically, the ZephIR systems could be assimilated into WINDoe alongside CLAMPS to produce a combined output and fill the near-surface data gap, but this was not pursued here due to large uncertainty up to 180° *wd* measurements from the ZephIRs. Typically the *wd* from the meteorological station attached to each ZephIR unit is used to constrain the estimate of flow direction; however, the proximity of these stations to the CLAMPS trailers meant that the trailers themselves obstructed airflow whenever winds approached from the CLAMPS side — an issue that was particularly pronounced during weak wind conditions. Initial tests determined that the potential benefit of incorporating the ZephIR data into WINDoe did not outweigh the associated data quality concerns. Furthermore, WINDoe uses layer-to-layer correlations to spread

information from above through the low-level data gap. Since this chapter's analysis focuses on or relationship between ws and low-level mixing, it is worthwhile to assess the WINDoe output in this layer using ZephIR observations available during their period of concurrent operation.

Jordan et al. (2024)'s Figure 6 (reproduced as Figure 3.4 here) showed a comparison between ZephIR and WINDoe data computing the root mean squared error (RMSE) and bias profiles between WINDoe and ZephIR winds. The same comparison was enacted between the ZephIR data and VAD retrievals starting at 60 m (where VAD data become available). As a whole, WINDoe-ZephIR comparisons at both sites yielded slightly lower RMSE than ZephIR-VAD comparisons (Fig. 3.4a) while the bias profiles (Fig. 3.4b) all maintained values near 0 $\mathrm{m\,s^{-1}}$. Though minor, the largest disagreements as indicated by RMSE and bias originated from the lowest levels, and they were consistent with Gebauer and Bell (2024), who found a similar features when validating WINDoe at the ARM-CF site. The general agreement across both sites and both retrieval approaches supports the reliability of the WINDoe ws profiles through the rotor layer, providing confidence in their use for characterizing NLLJ structure in subsequent analyses.

3.1.3 Data Selection Criteria

The ARM-CF and AWAKEN sites all have similar surface characteristics, with grassland pastures and cultivated fields on-site and to their south. For ARM-CF data, clear-sky conditions were prioritized to isolate cases where differences in cloud radiative effects and convective mixing would not confound investigation of wind farm-induced turbulence. Also, it provided the opportunity to identify wakes under pristine atmospheric conditions that were not as easily measured with CLAMPS and their associated data malfunctions during AWAKEN. Using satellite imagery and lidar backscatter

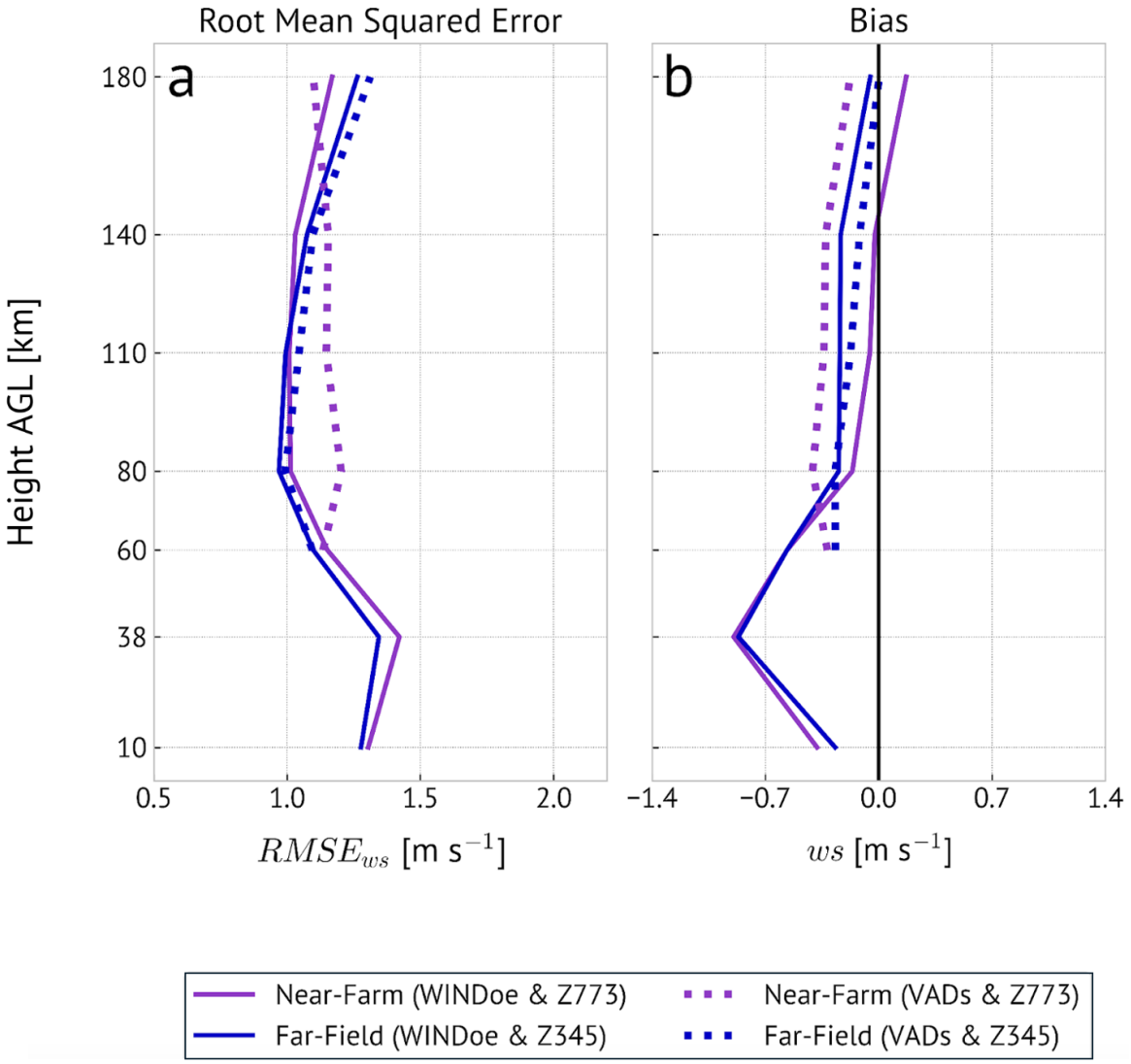


Figure 3.4: Root mean squared error of the ws between WINDoe and ZephIR data (Fig. 3.4a, solid lines) and the ZephIR and CLAMPS scanning lidar VAD retrievals (Fig. 3.4a, dotted lines) during the 2022 fall-winter campaign. Fig. 3.4b shows the same dataset comparisons but with mean bias calculations. WINDoe data were matched to the nearest ZephIR and VAD data heights. The ZephIR-VAD comparisons start at roughly 60 m where observations from the CLAMPS lidars begin.

data, periods with clouds or fog were removed, with the exception of clouds that were thin (i.e., the sites were visible through them), lasted less than an hour, or only appeared at the very end or very beginning of the case. While clear-sky conditions were

similarly preferred for AWAKEN, the limited duration of the CLAMPS deployments and requiring concurrent data from both units made strict sky condition filtering less feasible. The criterion was therefore loosened for AWAKEN data to include non-precipitating days, justified by the differing roles of each dataset: AWAKEN provides a direct same-time, same-day comparison between wind farm and non-wind-farm sites, while ARM-CF serves as a long-term statistical baseline for characterizing the broader northern Oklahoma wind environment.

Turbulent motions in the ABL are inferred by high-resolution measurements of w, which can be post-processed into σ_w to study mixing in the ABL. That was done here using 10-minute averages (5-minute centered windows). SNR filtering thresholds for the w observations were determined from Chapter 2 systematic tests and examining time-height profiles: ARM-CF and CLAMPS1 both achieved a good balance between noise removal and data retention at a threshold of 0.013, while CLAMPS2's lower sensitivity required a stricter threshold application of 0.017. This study utilizes rotor-disk-averaged σ_w to represent mixing over hub-height and encompass the differing turbine heights across the wind farms as much as possible. That said, the computed rotor-disk averaged σ_w values refer mainly to the upper portion of the rotor disks, as the averages were computed over 75–135 m beginning at the first usable level where σ_w is uncompromised by noisy returns. WINDoe retrievals span a slightly broader range of 60-135 m. We also filter out periods when turbines were unlikely to be operating by excluding cases where rotor-averaged wind speeds fell below 3 $\mathrm{m\,s^{-1}}$ or exceeded 25 $\mathrm{m\,s^{-1}}$ (Bodini et al., 2021).

Data collected from other ARM-SGP or AWAKEN sites are incorporated as relevant. Approximately 12 km east-southeast of CLAMPS1 was NREL's AWAKEN site A2 (36°31'81.98"N 97°40'90.79"W; Fig. 3.1c). Under southerly flow, CLAMPS1 and A2 share relatively similar terrain characteristics, especially direct southwest flow

(∼190°-210°). This allows an additional comparison of CLAMPS1 with a non-waked site, but one that more closely resembles its surrounding surface characteristics those south of the CLAMPS2.

Note that the A2 lidar was a Halo XR scanning lidar like those deployed at ARM-CF and on CLAMPS, but at this site the scan routine consisted of 20-minute vertical wind profiling via the six-beam scanning technique (Sathe et al., 2015) and 10-minute vertical staring, rather than VADs that have served as the the standard processed scanning strategy on ARM-CF and CLAMPS lidars (VADs were adopted following scanning strategy assessments during LABLE; see Newman et al. (2016) for more information). This means the σ_w was sampled differently than CLAMPS, as the six-beam scanning strategy at A2 introduced 20-minute gaps in σ_w measurements during each scan cycle. While WINDoe can make use of information from different scanning strategies across sites (i.e, VADs and six-beam), resolving these gaps in σ_w required additional measures: The A2 σ_w was resampled to 30-minute aggregations, as were the CLAMPS σ_w datasets only when they are compared with A2. SNR-filtering was applied to the A2 as was done with the CLAMPS data; the A2 lidar displayed similar levels of sensitivity as CLAMPS2, so it was filtered at the same 0.017 threshold. The A2 lidar was only deployed for July and August 2023, so only those periods during the CLAMPS deployment were able to be compared to A2 data.

3.2 Low-level Mixing Results

3.2.1 Initial Evidence of Wind Farm Mixing

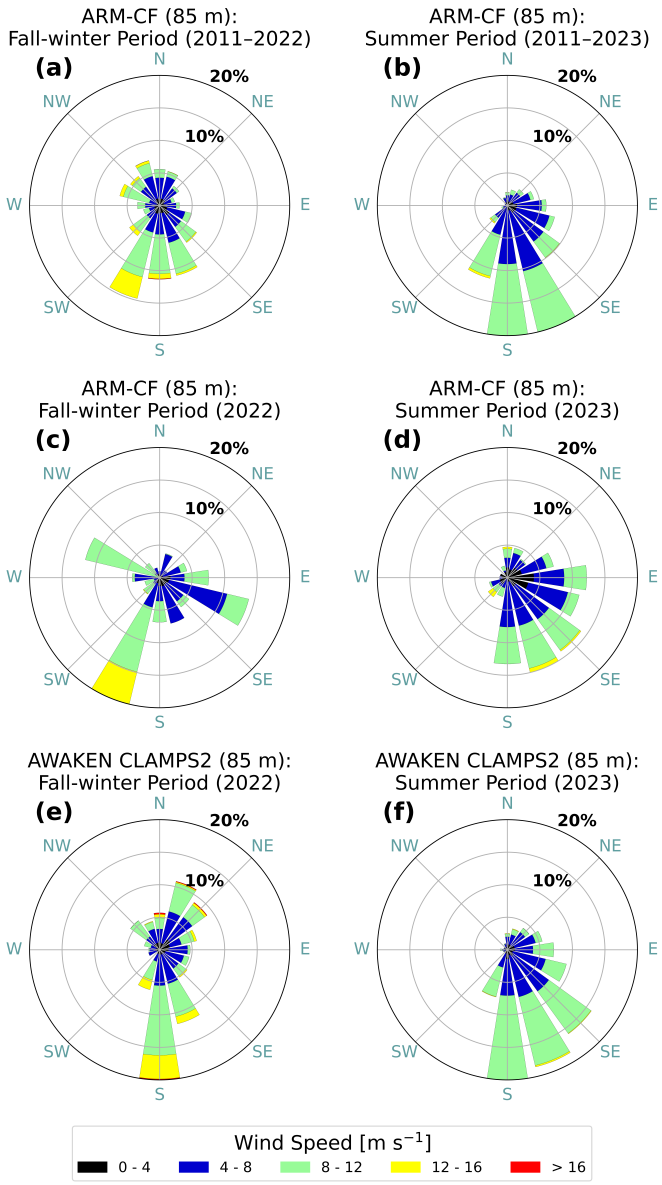


Figure 3.5: Wind roses of using WINDoe data of the analysis periods of interest during the fall-winter and summer seasons from the ARM-CF lidar (Figs. 3.5a-3.5b) and the CLAMPS2 lidar. Only CLAMPS2 data from the far-field site is shown since, unlike CLAMPS1, had correct *wd* during the summer.

The downwind extent of wind farm mixing depends on the prevailing regional flow patterns occurring in the region. Figure 3.5 shows wind roses for ARM-CF during the fall-winter (Fig. 3.5a) and summer (Fig. 3.5b) for the pre-farm and post-farm periods together. Fig. 3.5c-d shows data from the same ARM-CF site only including data from the 2022 and 2023 CLAMPS AWAKEN deployment periods, and Figs. 3.5e-f show the wind roses from the far-field CLAMPS2 site (CLAMPS1 is omitted from this analysis due to the erroneous wd). The multi-year ARM-CF data can serve to represent winds typical to the area. A similar ARM-CF climatology was presented across all seasons in Krishnamurthy et al. (2021b) and the Fig. 3.5a-b results are consistent with their Figure 27 with winds predominantly southerly in both seasons but with more frequent and stronger southwesterly and northerly flow during the colder months and weaker southeasterly flow in summer.

The ARM-CF period was then isolated to the AWAKEN periods to determine how well those periods matched with the overall climatology. ARM-CF AWAKEN fall-winter ws in Fig. 3.5c showed southerly flow was again the most common flow direction, but westerly and east-southeasterly winds occurred more frequently than the climatological mean for that season. AWAKEN summer winds (Fig. 3.5d) aligned more closely with typical ARM-CF summer conditions, though with a somewhat greater easterly component than climatology. Over the same periods, CLAMPS2 at the E36 far-field site showed a greater emphasis on directly southerly flow in the fall-winter relative to the southwesterly predominance at ARM-CF, along with less frequent but stronger northerly flow. The summer period at CLAMPS2, however, matched ARM-CF closely and aligned even more strongly with the summertime climatology. Since turbines extract energy from the wind Tennekes and Lumley (1972); Lissaman (1979), these differences in winds across sites and seasons have important implications for how well the downwind fetch of wind farm mixing can be resolved. Bodini et al. (2021)

examined turbulent kinetic energy at ARM-CF, finding that it increases during stable conditions in post-farm years; we hypothesize that similar increases are present in both the ARM-CF and AWAKEN records examined here.

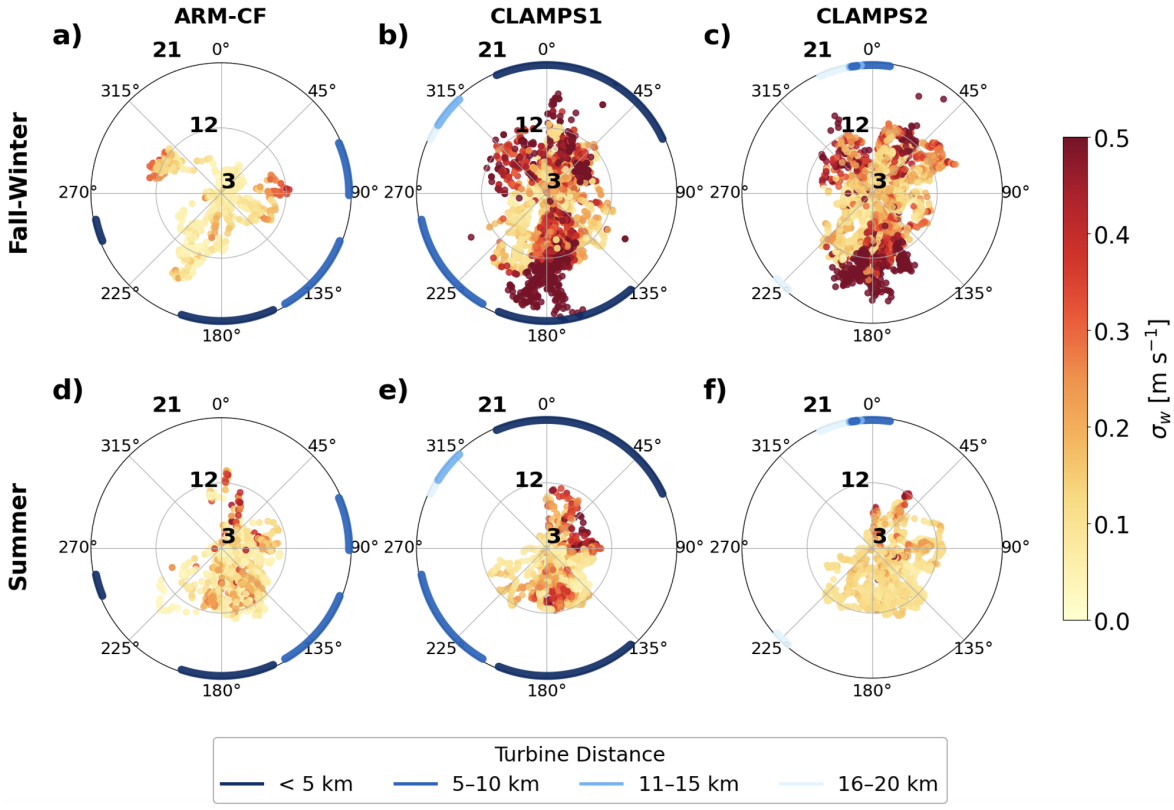


Figure 3.6: Polar plots containing rotor-layer averaged σ_w as a function of ws from all directions between 0000-1200 UTC. Blue outlines that appear on the polar region correspond to the sectors wind farms less than 10 km are located. Any ws below 3 m s^{-1} was discarded, aligning with the filtering rules that turbines are not expected to be operating below this threshold. All data available from each individual site is shown and there are not common timestamps between the sites. As in the wind roses, CLAMPS2 wd in the summer was used for the CLAMPS1 summer results.

Figure 3.6 examines rotor-layer σ_w as a function of wd for ARM-CF, CLAMPS1, and CLAMPS2 during the AWAKEN 2022 fall-winter (Figs 3.6a-c) and 2023 summer (Figs 3.6d-f), with arc overlays indicating the distance to the nearest turbines. During fall-winter, enhancements in ARM-CF σ_w values were modest relative to the

CLAMPS sites during AWAKEN, which both exhibited strong mixing from the north and south. As seen in the wind roses, ARM-CF during 2022 fall–winter was dominated by southwesterly flow, a direction with little-to-no turbine exposure. However, the other predominant directional flow during fall-winter (northwesterly and southeasterly) placed turbine rows from Chisholm View and Thunder Ranch within the upwind fetch, and notable mixing signatures were visible at ARM-CF from those directions. Further south, CLAMPS1 sat between the Armadillo Flats and King Plains wind farms, considerably closer to both than ARM-CF is to Thunder Ranch in any direction. Moreover, those two farms consist of large, dense turbine clusters rather than the row-like configurations upwind of ARM-CF, making CLAMPS1 subject to greater cumulative turbulent mixing, which is supported by the spatial pattern and magnitude differences in σ_w between the two sites primarily to wind farm effects.

Still, CLAMPS2 measured σ_w magnitudes from southerly directions comparable to those at CLAMPS1, despite being sited specifically to avoid wind farm influence from that sector. Unlike the northerly sector which comprises the south end of the Armadillo Flats farm, these mixing increases were unexpected from the south. Near-surface inhomogeneities from subtle terrain was one consideration; if this was the case, similar strong σ_w from both CLAMPS would be expected in the summer too, as the terrain itself does not vary seasonally. However, the summer period in Figs. 3.6e–f instead depicted the anticipated σ_w signals found in Bodini et al. (2021) based on wind farm direction. That said, their analysis did not include a seasonal breakdown. To this end, Fig. 3.6 suggests that wind farm mixing signatures are much more discernible in the summer.

The suspected primary driver of obscuration of wind farm mixing signatures in the fall-winter is the prominent SGP NLLJ, which can provoke near-surface bulk-shear turbulence when strong enough (Bonin et al., 2015), and NLLJs are typically stronger

during fall-winter (Krishnamurthy et al., 2021b). In addition to its seasonal variability, the NLLJ also varies diurnally, so a time series can be used to determine how rotor-layer mixing varies during typical NLLJ hours. Figure 3.7 illustrates daily-averaged σ_w between the non-waked and waked regimes: ARM-CF pre-farm and post-farm periods and AWAKEN far-field and near-farm sites. Here, only the nighttime period and southerly NLLJs were considered.

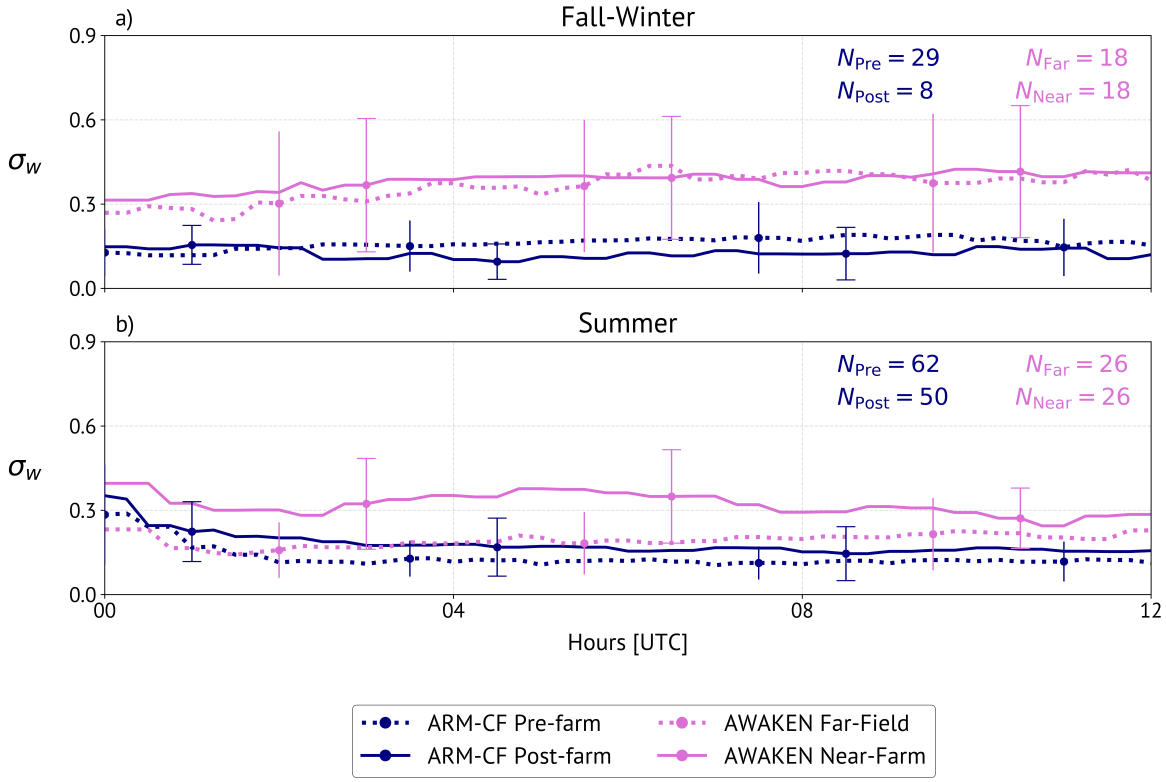


Figure 3.7: Comparison of averaged σ_w levels between environments with and without nearby wind farms from the southerly sector between 0000-1200 UTC. Fig. 3.7a corresponds to the fall-winter periods from ARM-CF pre-farm (blue dashed line), ARM-CF post-farm (blue solid line), AWAKEN far-field (pink dashed line), and AWAKEN near-farm (pink solid line). Fig. 3.7b shows the same but during the summer periods.

In both seasons, the AWAKEN time-series mirrored the patterns of the polar plots. The ARM-CF comparisons followed a similar pattern to the CLAMPS outputs. Dur-

ing fall-winter, there was no substantial difference in σ_w between pre- and post-farm environments, with pre-farm values frequently exceeding those from post-farm across much of the diurnal cycle. During summer, however, neither the ARM-CF pre-farm nor the AWAKEN far-field surpassed their post-farm and near-farm counterparts at any point during the 12-hour period. Both ARM-CF and AWAKEN showed considerably stronger σ_w enhancements near wind farms relative to non-waked environments. At times, σ_w differences in the AWAKEN comparisons were nearly twice those seen in the ARM-CF comparisons, furthering evidence that the dense turbine layout from Armadillo Flats strengthens mixing signals compared to the turbine rows from Thunder Ranch.

In the SGP, NLLJs often develop within a few hours after the evening ABL transition is complete. During the 0000–0300 UTC window, post-farm σ_w exceeded pre-farm values for the only time throughout the fall-winter 0000-1200 UTC period. If near-surface mixing is indeed driven by strong NLLJs, it follows that the fall-winter NLLJ, which is climatologically stronger than in summer, could obscure wind farm wake signatures at ARM-CF. The NLLJ-driven obscuration occurs at the CLAMPS sites during AWAKEN too, but because CLAMPS1 is downwind of a larger collective of turbines, wakes are still discernible throughout a good part of the period. In the summer, the NLLJ is climatologically weaker (Krishnamurthy et al., 2021b) and is less likely to generate as much turbulence, allowing wind farm effects to be more readily discernible. Taken together, these findings across sites, seasons, and wind farm regimes underscore the importance of accounting for the NLLJ when interpreting wind farm observational research.

While wind farm mixing can persist or even be enhanced alongside the NLLJ, the extent to which jet-driven turbulence obscures that mixing remains unclear. Using WINDoe, which was shown in Chapter 2 to successfully resolve the full NLLJ struc-

ture, NLLJ characteristics can be characterized to understand wind farm impacts in a location with a frequently-occurring NLLJ. Accordingly, we examine the NLLJ occurrences across pre- and post-farm periods at ARM-CF and across the AWAKEN deployment sites to better understand the conditions under which wind farm effects are detectable.

In addition to the data selection criteria outlined in Section 3.1.3, the analysis hereafter targets the 135°–225° southerly wind sector unless otherwise stated, requiring at least 90% of rotor-averaged winds to fall within those bounds for a case to be retained. CLAMPS2 cases falling within the Red Dirt wind farm regime were excluded. Also, to improve comparability between the ARM-CF pre- and post-farm datasets despite their non-concurrent sampling, a surface T filter was applied to ARM-CF data using climatological records from the Regional Climate Center, the National Centers for Environmental Information, and the NWS, retaining only cases in which the daily minimum T remained within 5°C of the climatological average (the pre-farm period includes 2011, which was a record breaking drought year with extreme heat). When applied to the Fig. 3.7 results (not shown), pre- and post-farm σ_w profiles closely matched their AWAKEN counterparts. Note that this filter substantially reduced the number of available ARM-CF cases, particularly in fall-winter; therefore, ARM-CF fall-winter results are treated hereafter as a preliminary assessment rather than a definitive climatological reference.

3.2.2 NLLJ Considerations

To contextualize how external mixing sources like NLLJs influence mixing generated by nearby wind farms, we must understand the characteristics of the NLLJs occurring during the analysis periods. Figure 3.8 shows ARM-CF hourly mean composites of the maximum ws at a given time, as well as the altitude at which that maximum occurs.

These composites were extracted from the NLLJ classification algorithm, which assigns jet classes based on the altitude where the nose *ws* peaks, and all wind results were derived using WINDoe data.

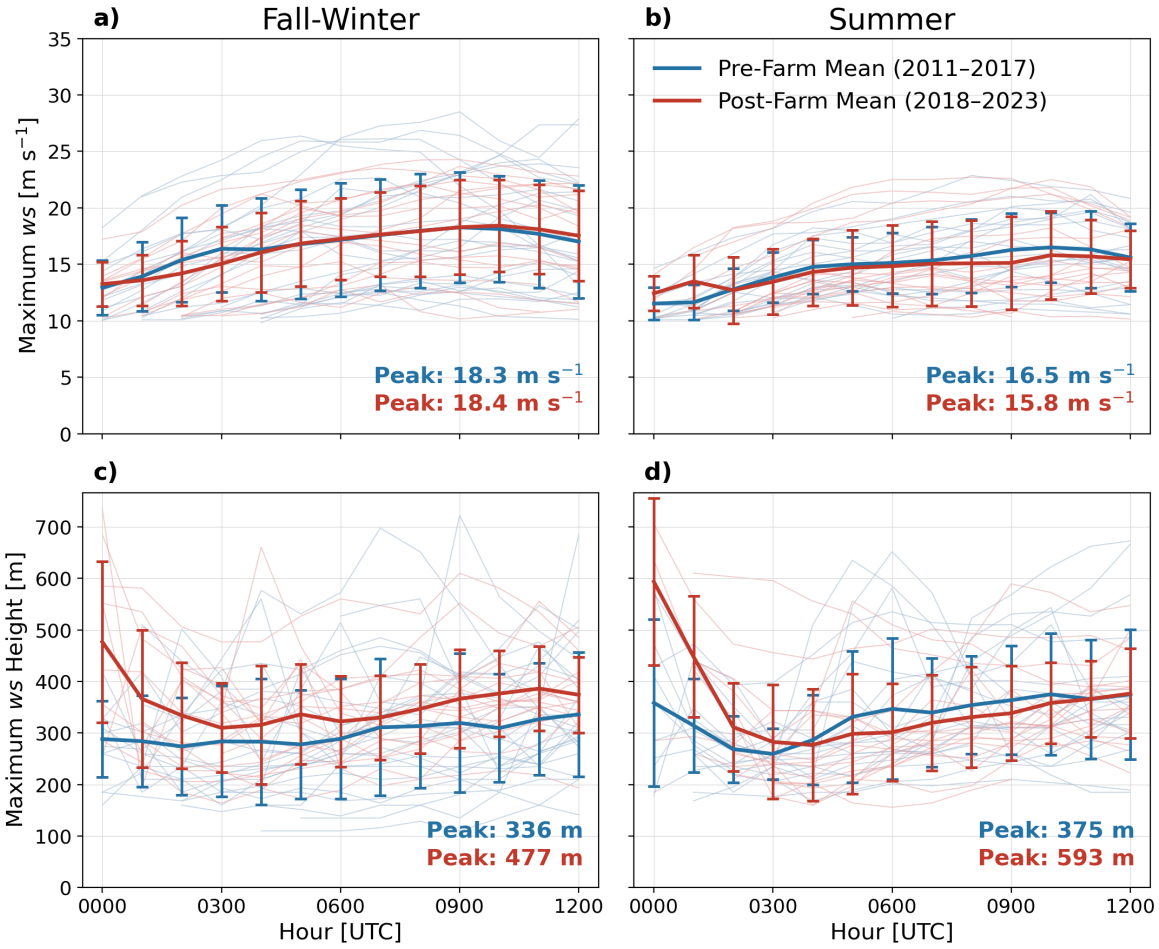


Figure 3.8: Hourly means showing NLLJ characteristics through maximum *ws* (Fig. 3.8a-b) and the altitude it occurs at (Fig. 3.8c-d) as measured by ARM-CF pre-farm (first column) and post-farm (second column).

For the most part, there was not a substantial difference in the maximum *ws* between pre- and post-farm environments (Figs. 3.8a-b), but fall-winter, on average, did produce stronger NLLJ than summer, matching the Krishnamurthy et al. (2021b) climatology. The altitude of the *ws* maximum, including the NLLJ nose, was more

elevated in post-farm conditions. A recent publication using AWAKEN datasets asserts that wind farms have the capability of elevating the NLLJ downstream, especially if it was originally below 250 m (Krishnamurthy et al., 2025); from their findings, the post-farm levels were expected to be higher, though there was also considerable spread in the individual cases. To deduce if lower NLLJs in waked environments during the summer were a recurrent feature, Figure 3.9 presents a similar analysis of maximum ws and its corresponding height focused on the AWAKEN period. As expected, Figs. 3.9c-d shows that post-farm heights exceed pre-farm as in Krishnamurthy et al. (2025). However, strong scatter continued to be associated with the individual cases; ws also displayed large case-by-case differences in the fall-winter period (Fig. 3.9a) that do not occur in the summer period (Fig. 3.9b). These presentations of the NLLJ characteristics provide a useful foundation for understanding how NLLJs generally behave across the periods. However, substantial scatter in the data limits the ability to draw definitive conclusions regarding wind farm impacts. One way to address this is to further refine the analysis by stratifying NLLJs according to their strength.

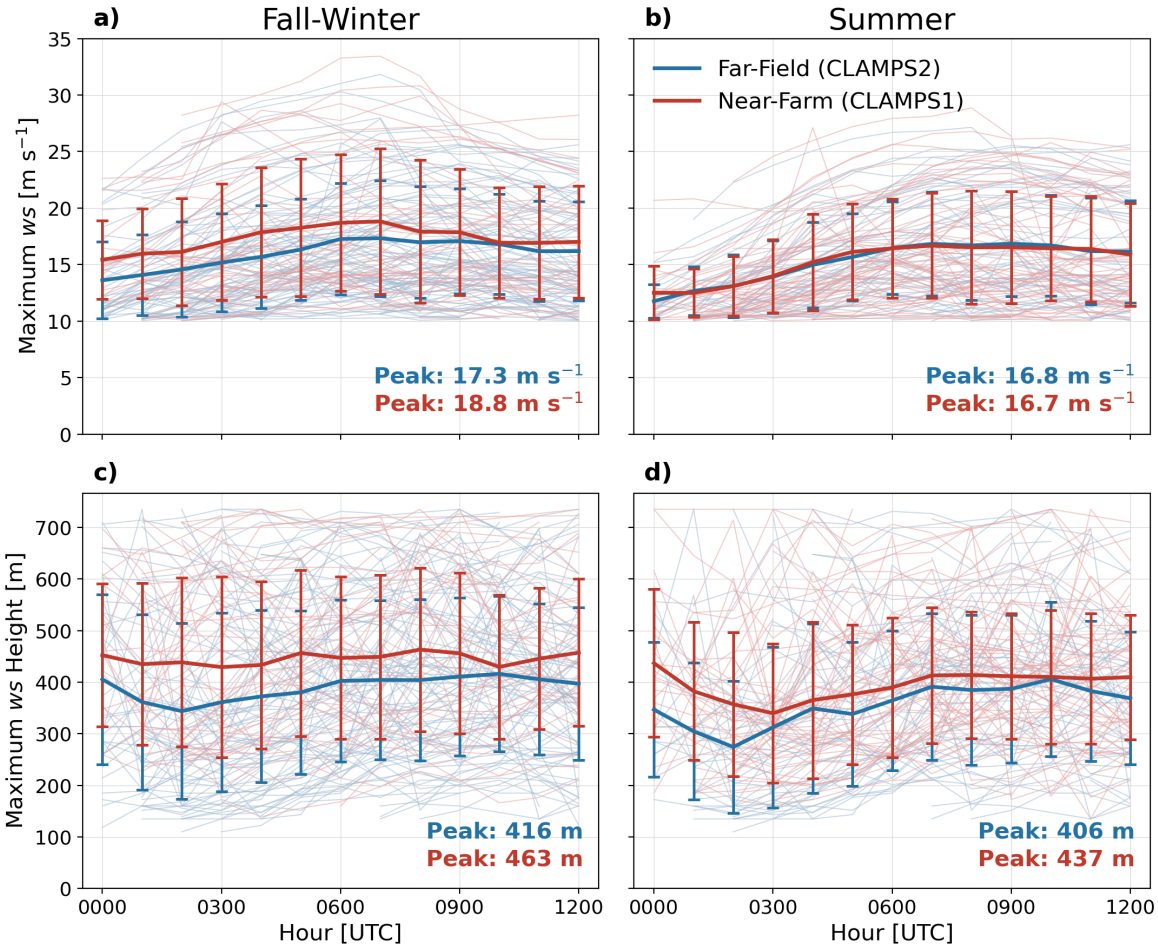
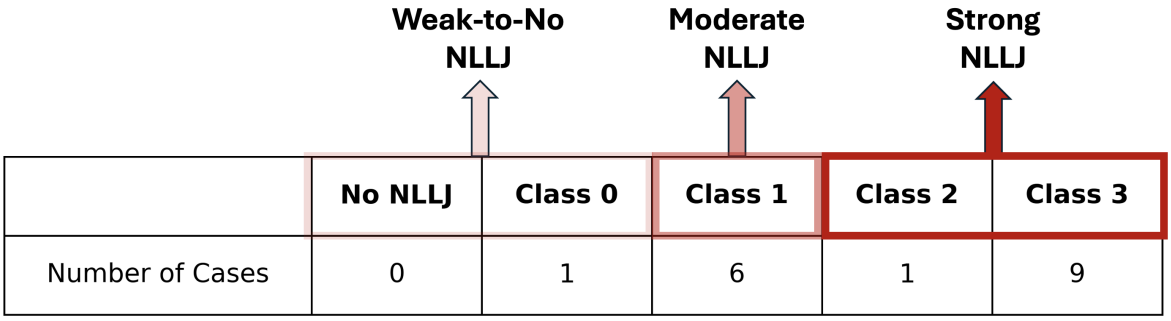


Figure 3.9: As in Figure 3.8, but in place of ARM-CF pre-farm are results from AWAKEN far-field (first column), and in place of ARM-CF post-farm are results from AWAKEN near-farm (second column).

This separation is achieved by employing the NLLJ strength classification algorithm described in Section 2.2.1. That section included a description of defined classes and their corresponding strength ranges from classes 0 (no NLLJ) to class 3 (very strong NLLJ). For simplicity and to increase sample size per bin, No NLLJ and Class 0 are combined into a weak-to-no NLLJ category, class 1 represents moderate NLLJs, and classes 2 and 3 correspond to strong and very strong NLLJs. The classification framework is also applied to AWAKEN site A2, providing an additional non-waked

reference from a location with terrain to its south resembling the terrain south of CLAMPS1.

Table 3.1: The number of cases within each of the five NLLJ classes as categorized by Whiteman et al. (1997): "no NLLJ", "Class 0" corresponding to weak NLLJs, "Class 1" to moderate NLLJs, "Class 2" to strong NLLJs, and "Class 3" to very strong NLLJs. Going forward, these five regimes get further binned into 3 groups: weak-to-no NLLJs consisting of no NLLJ and class 0, moderate NLLJs consisting of class 1, and strong NLLJs.



Time-height cross-sections of ws, σ_w and rotor-layer-averaged σ_w time series were constructed for CLAMPS1, CLAMPS2, and A2 during periods when all three sites had concurrent data. Table 3.1 shows the number of cases per individual class used in this analysis. Since cases were limited they were combined into three regimes: weak-to no NLLJs, moderate NLLJs, and strong NLLJs. Profiles were composited within the moderate and strong NLLJ bins (moderate: 6 cases; strong: 10 cases) and Gaussian-smoothed. Only a single case was available in the weak-to-no NLLJ bin, so that event is presented individually rather than as a composite. ARM-CF was not included to avoid limiting the observations further. Note that CLAMPS2 wind speeds fell below 3 $\mathrm{m\,s^{-1}}$ after 0915 UTC in this case; while such conditions exclude it from the 0000–1200 UTC daily mean analysis, the case is retained here for the purpose of cross-site comparison.

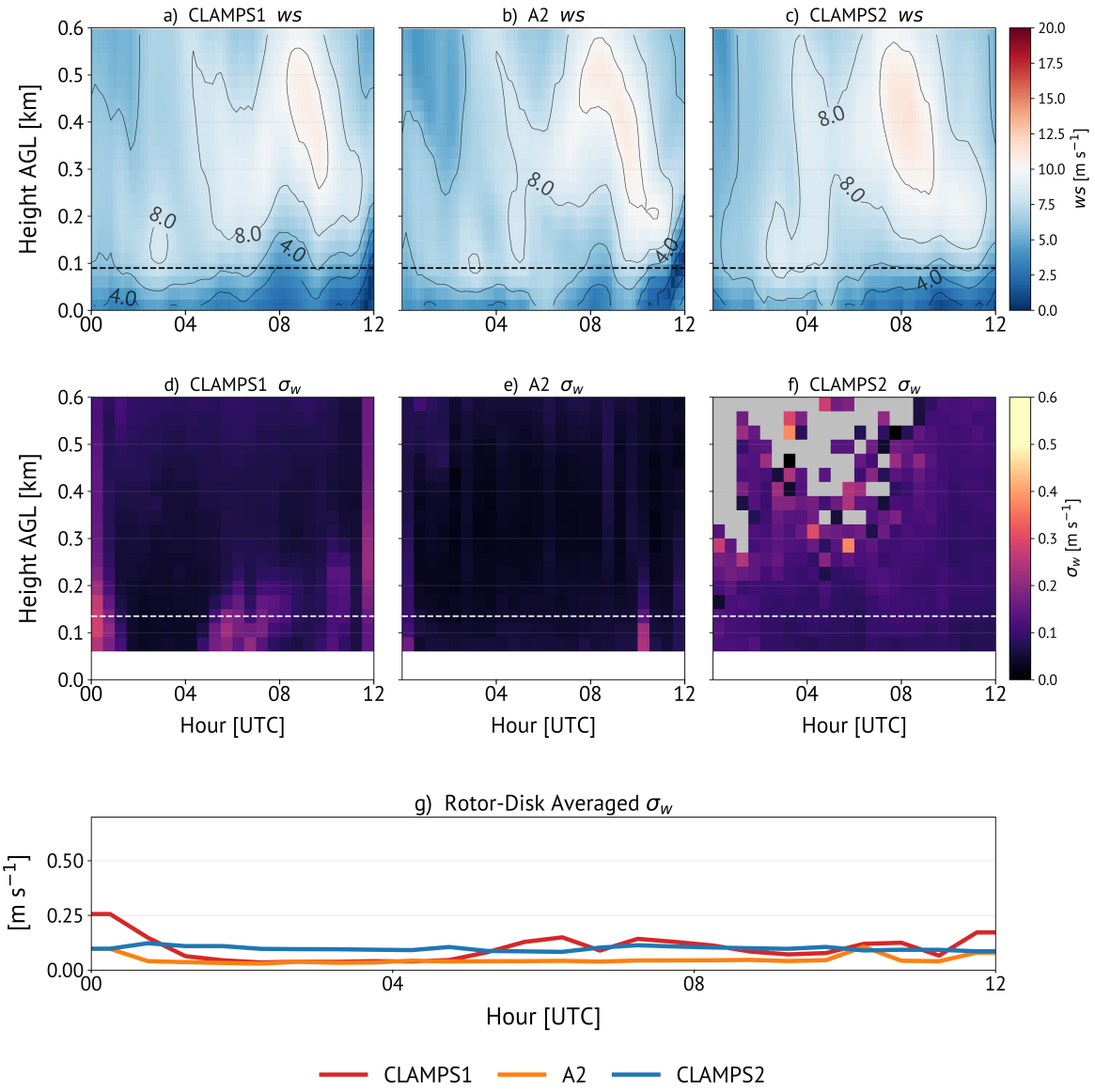


Figure 3.10: Profiles of ABL ws (Fig. 3.10a-d) and σ_w (Fig. 3.10e-h), and time-series of rotor-averaged σ_w (Fig. 3.10g) for a weak-to-no NLLJ case. Horizontal black dashed lines in the ws represent hub height, and the white dashed lines indicate the height of the rotor tip.

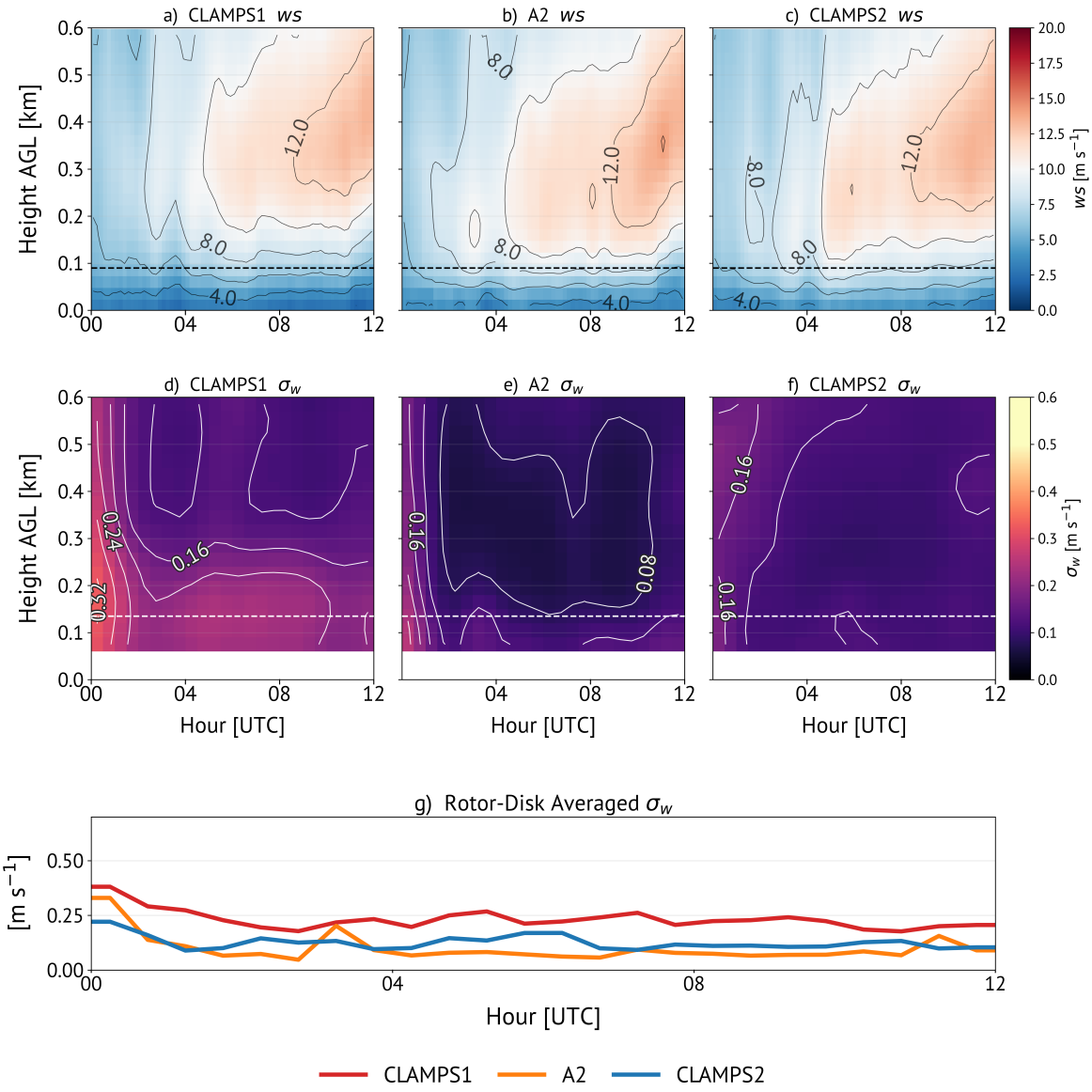


Figure 3.11: As in Fig. 3.10, but as composites for moderate NLLJ cases.

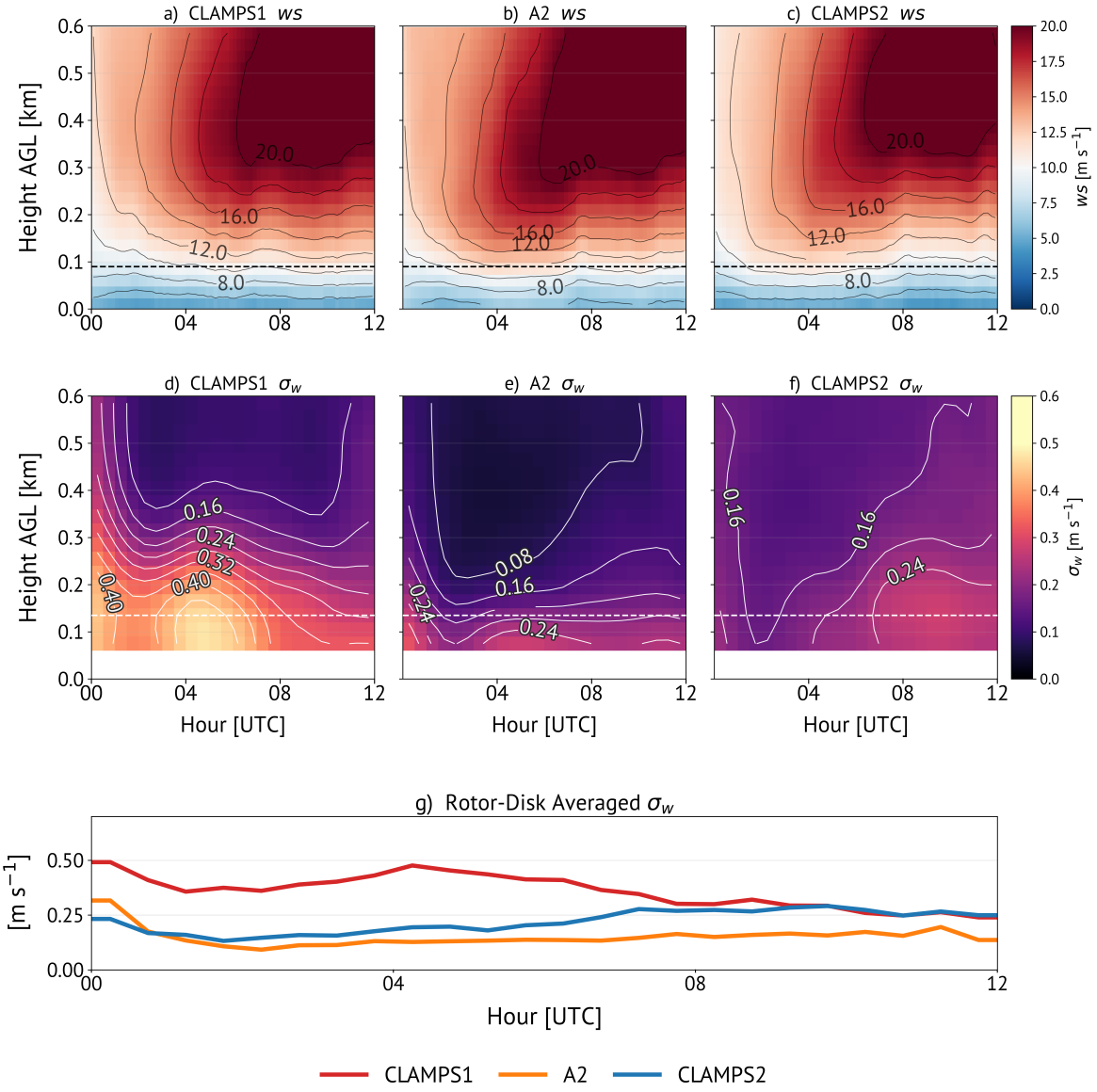


Figure 3.12: As in Fig. 3.10, but for composited strong NLLJ case.

Figures 3.10-3.12 present ws and σ_w variables from the weak-to-no, moderate, and strong NLLJ regimes, respectively. The weak NLLJ developed around 0400 UTC at all three sites (Figs. 3.10a–3.10c); since only a single case was used, it showed stark variations in jet shape and core structure across locations compared to the other NLLJ classes. Near hub heights (indicated by the black dashed lines on ws panels), ws was

typically near 6 $\mathrm{m\,s^{-1}}$. Under these weak flow conditions, there was generally limited turbulent mixing in the rotor layer (Figs. 3.10d-g), though modest σ_w enhancements within the rotor layer (the top of which indicated by the white dashed lines on σ_w panels) were evident at CLAMPS1 and, to a lesser extent, at A2.

It was under moderate NLLJ conditions (Figs. 3.11a-c) that strong and persistent σ_w signatures emerged at the CLAMPS1 site (Figs. 3.11d). Across the sites, the ws around hub-height was around 8 $\mathrm{m\,s^{-1}}$. There were also some instances of minor σ_w increases at the other sites (Figs. 3.11e-f), but Fig. 3.11g confirms that, within the rotor-layer, the most intense mixing was concentrated at the CLAMPS1 site. This CLAMPS1 mixing is consistent with wind farm effects given that turbines extract kinetic energy from the wind above rotor tips, which, unlike in the weak NLLJ case, is strong enough throughout the period to supply energy from which turbines can extract. Further proof of wind farm-induced mixing can be drawn from the high σ_w during the evening and morning ABL transitions, pointing to a delayed decay of convective mixing in the evening and an earlier onset in the morning relative to the other sites. That behavior aligns with previous findings (Fitch et al., 2013; Rajewski et al., 2020), which demonstrated that wind farms can extend transition periods.

If wind farms gain their energy from NLLJ winds, then it is safe to presume that even stronger NLLJ cases would lead to stronger mixing. When strong NLLJ composites are presented in Fig. 3.12a-c, high values of σ_w within the rotor layer were indeed present and strongest at CLAMPS1 (nearing values of 0.5), which could possibly reflect more turbine power outputs (at least until winds are too strong for the turbine to operate in). However, it is difficult to determine if the mixing from CLAMPS1 is driven by wind farm effects, the NLLJ, or a combination of both. In general, powerful NLLJs can compromise the identification of wind farm mixing because they can induce their own turbulent motions (Banta, 2008; Klein et al., 2015), which is seen by

the intense σ_w signals at A2 and CLAMPS2 throughout the period (mainly when the jet nose peaked) that did not appear prior.

That information helps to reveal a clear pattern: NLLJs can provide energy for wind farms but they also generate their own turbulence and can mask any wind farm-induced mixing that may be present. This masking effect leads to difficulties in truly quantifying wind farm impacts on the ABL, so additional analysis is required to identify the point at which wind farm mixing is likely to be dominated by NLLJ-driven mixing.

3.2.3 Wind Threshold Method

As discussed in the introduction to this chapter, identifying wind farm effects in an environment where NLLJ-driven mixing can be strong is a challenging concept. We hypothesized that previous findings about relationships between NLLJ speed and turbulent mixing developed by Bonin et al. (2015) (hereafter, B15) can be used to better isolate wind farm effects: B15 used lidar observations to identify a threshold ws (V_T) at which nocturnal turbulence typically develops in southerly flow conditions near ARM-CF during the LABLE campaign. In basic terms, horizontal ws that exceeds that V_T at a certain height is deemed sufficient to generate bulk-shear turbulence at that height. This method was adapted from Sun (2011), which used sonic anemometers, but incorporating lidar data allowed more coverage of heights in the ABL, including the NLLJ, and allowed B15 to understand the depth of the generated turbulent mixing. They also addressed how the relationship between ws and σ_w at any given height is affected by winds above and below their measured height, rather than just that height alone, finding that the V_T near the surface must be surpassed for significant mixing to be generated above it. This offers important information for understanding SBLs as a whole, but it is also useful for the wind farm study herein. By determining when and at what level winds are strong enough to drive mechanical mixing (e.g., NLLJs), periods

can be selected that allow us to determine if wind turbine effects can be isolated. The method from B15 is replicated here with few changes to enable a wind farm focus.

B15 computed 30-minute ws bins in increments of 1 $\mathrm{m\,s^{-1}}$ (e.g., 0–1, 1–2, 2–3, and so forth) until 25 $\mathrm{m\,s^{-1}}$ was reached. These ws values were paired with σ_w that occurred at the same time and height. The median and standard deviation were computed within each bin. The V_T is determined as the point at which the slope of $\mathrm{d}(\sigma_w)/\mathrm{d}(ws)$ sharply increases. The B15 study only used data between 0200-1200 UTC, where periods with clouds below 3 km were eliminated and the influences of fronts were filtered out by excluding time periods with rapid changes in surface conditions. These methods are followed here for ARM-CF and AWAKEN non-wind-farm and wind-farm environments. Since CLAMPS1 did not have a meteorological station or AERI operating in 2022 fall-winter, frontal boundaries were inferred from synoptic surface maps from the Weather Prediction Center.

There are a few differences in this study's method compared to B15. That study used purely southerly flow whereas here, we continue using cases that have at least 90% southerly conditions. Instead of 30-minute ws bins (which B15 used to align with sonic anemometer data), 10-minute bins were used here, requiring at least 9 valid 10-minute intervals per ws bin. This allows more samples to be included in the analysis, though higher temporal resolution may also capture shorter-scale variability, which can increase noise in the output. Lastly, B15 computed σ_w with the Lenschow et al. (2000) noise-removal method with 1-4 lags. The Lenshow method is applied later in this work as part of the H_{FL} algorithmic computation, but in this analysis we use the centered-moment σ_w to show how it performs with the easiest, most standard method of computing σ_w, which avoids the stationarity assumptions required by the Lenschow method that may be violated in the shear-driven, intermittently turbulent nocturnal environments examined here.

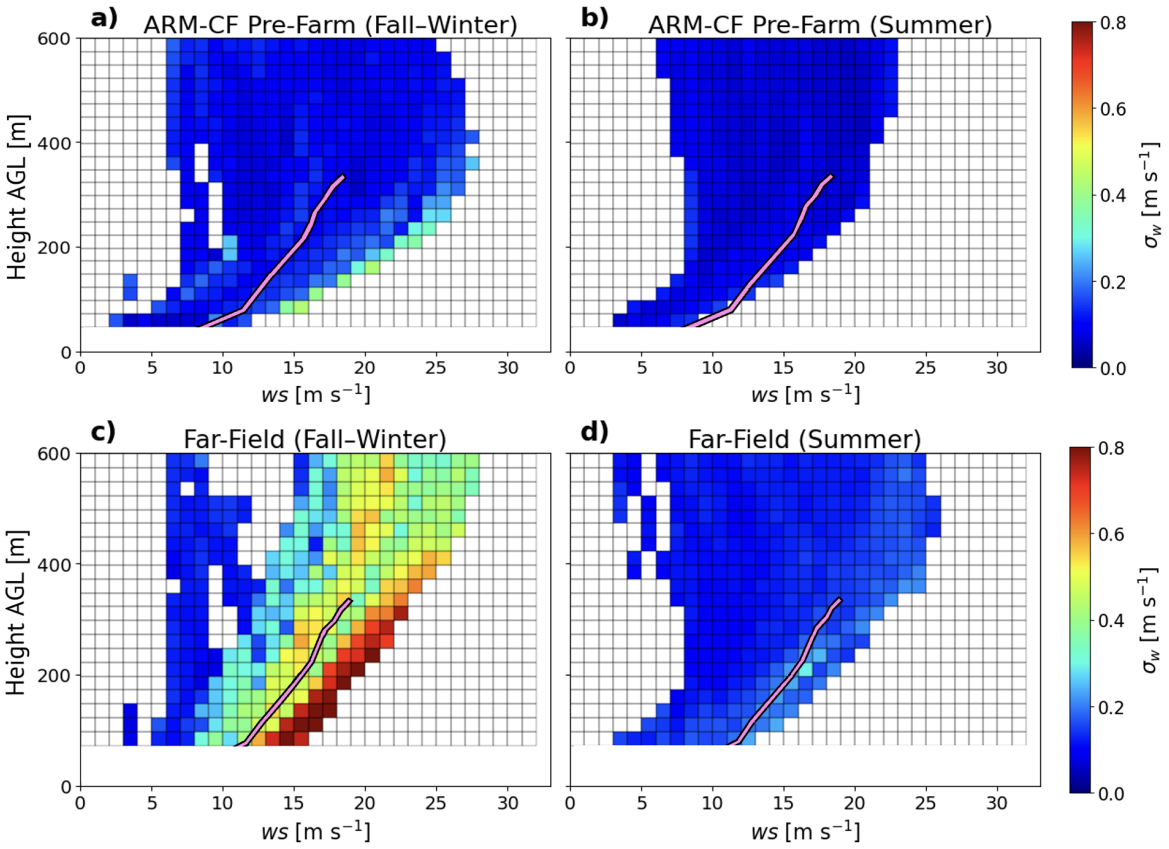


Figure 3.13: Profiles of median σ_w from environments without nearby wind farms during the ARM-CF and AWAKEN fall-winter (Figs. 3.13a and 3.13c) and summer (Figs. 3.13b and 3.13d). The pink line denoting V_T as computed from B15.

B15 computed V_T from ARM-CF and OU lidar data during the LABLE campaign (2012-2013), establishing the expected thresholds of turbulence generation when wind farms are not considered. Building on their analysis (see B15 Figure 4), the B15 V_T thresholds are shown as pink lines in Figure 3.13 overlaid on the σ_w medians from the current study's ARM-CF pre-farm and AWAKEN far-field periods, providing a basis for evaluating how well the current datasets align with predetermined thresholds derived from B15's sample. The ARM-CF σ_w background medians Figs. 3.13a-b did not increase appreciably until ws reached 14 m s^{-1} whereas B15 observed strong σ_w-ws relationships emerging at weaker ws. This discrepancy primarily reflects differences in

dataset composition: the ARM-CF cases here include a T-filter intended to suppress the influence of ABL extremes, thereby likely reducing the prevalence of shear-driven turbulence associated with the strongest NLLJs. The LABLE data used to compute the B15 V_T were derived from fall-winter cases; using that same threshold as an overlay during the ARM-CF pre-farm summer, when σ_w medians were weak at best (Fig. 3.13b), further underscores the extent to which strong NLLJs can reduce V_T values.

The AWAKEN CLAMPS2 data did not undergo the T-filtering applied to ARM-CF data, and the σ_w and ws showed a much stronger relationship (Figs. 3.13c-d). As a result, the V_T for both fall-winter and summer better reflected the thresholds produced by B15. Comparing the B15 V_T with AWAKEN σ_w medians shows the V_T does reliably identify conditions with shear-driven turbulence. On the other hand, the comparison of ARM-CF σ_w medians and B15 V_T suggest that a single predetermined threshold may not represent the variability introduced by using data with differing sample sizes, seasonal compositions, and observational periods.

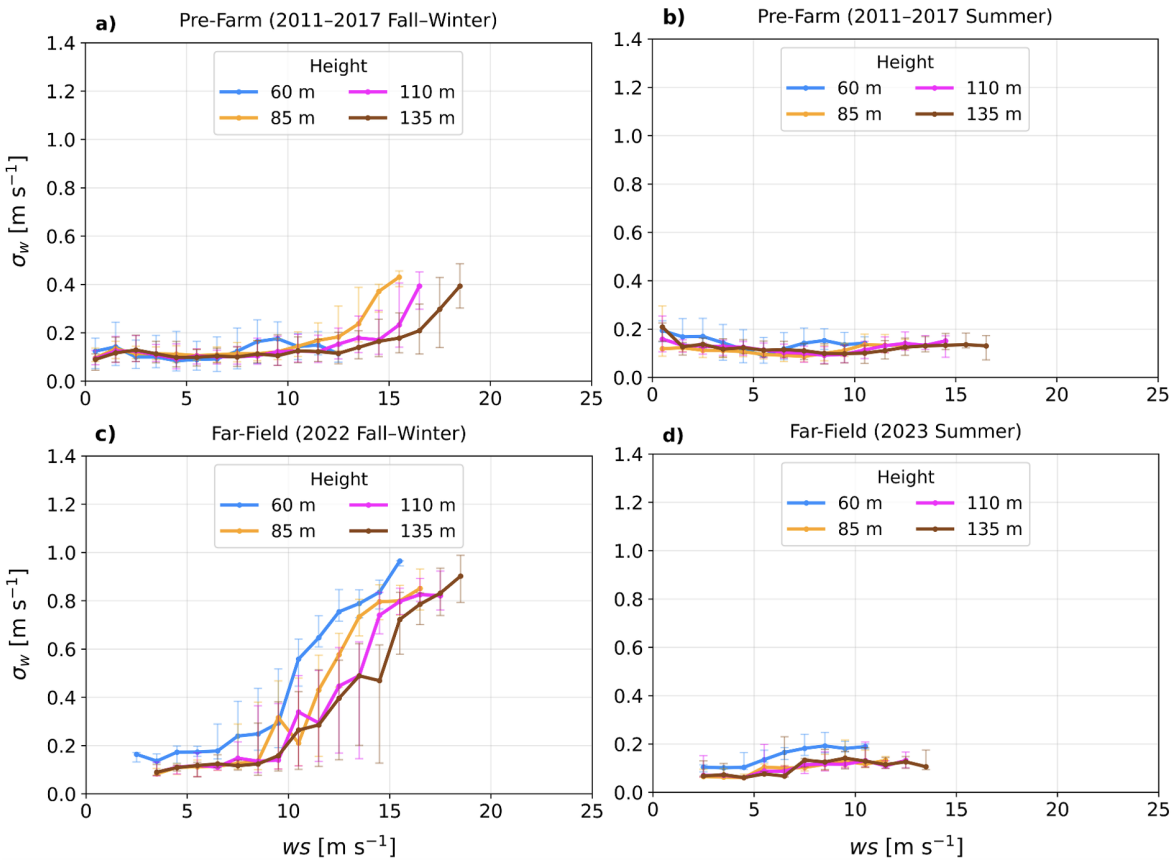


Figure 3.14: The V_T from non-waked environments as calculated from ARM-CF and AWAKEN fall-winter (Figs. 3.14a and 3.14c) and ARM-CF and AWAKEN summer (Figs. 3.14b and 3.14d) at rotor layer heights (60, 85, 110, and 135 m).

To more closely examine the similarities and differences between the ARM-CF and AWAKEN datasets, V_T was computed across the two seasons. Following another approach from B15 (see their Figure 3), we considered only heights within the rotor layer (60, 85, 110, and 135 m), and only periods or sites without wind farms, helping to ensure the thresholds represent turbulence related to shear, not turbine effects. A relevant finding from B15 is that turbulence production at a given layer required V_T to be exceeded at or below that height, meaning these rotor-layer thresholds carry information about NLLJ effects below the level where the peak winds usually occur. Consistent with Fig. 3.13, the summer seasons (Fig. 3.14b and 3.14d) exhibited no

strong dependence of σ_w on ws. Conversely, the fall-winter seasons in both datasets (Figs 40a and c) showed an increase in $\mathrm{d}(\sigma_w)/\mathrm{d}(ws)$ at all rotor levels when ws reached 8 - 10 $\mathrm{m\,s^{-1}}$. This indicates that ws exceeding 8 - 10 $\mathrm{m\,s^{-1}}$ can mask wakes produced by wind farms. In the composite strong NLLJ analysis in Fig. 3.12, NLLJ peak winds occurred above 300 m, but the shear layer below the nose of moderate NLLJs commonly result in ws of 8-10 $\mathrm{m\,s^{-1}}$ at or near hub-height. The moderate NLLJ composite (Fig. 3.11) shows that the rotor layer ws typically remained weaker than 8-10 $\mathrm{m\,s^{-1}}$ or only surpassed that speed in the upper portion of the rotor layer. While most of the rotor layer has ws weaker than 8 $\mathrm{m\,s^{-1}}$, it was still strong enough for turbines to operate (i.e., stronger than 3 $\mathrm{m\,s^{-1}}$). This confirms what was suspected based on the composites: moderate NLLJs supply enough flow for the turbines to extract energy from while not obscuring their wakes.

Given that moderate NLLJs provide more ideal conditions for detecting wind farm signatures, screening the data to focus on this regime formed the final analysis step in establishing low-level mixing from wind farms. In addition to considering only moderate jets, we also normalized the datasets by dividing σ_w at all heights by rotor-layer-averaged ws to reduce the influence of any other anomalies in the profiles and make values more comparable across cases. Figure 3.15 reintroduces comparisons between non-waked and waked regimes by comparing averaged percentile σ_w profiles. The case filtering eliminates all data from the AWAKEN fall-winter period, so only summer from AWAKEN is shown, a period that also includes the A2 site. Recalling that A2 possesses similar surrounding terrain CLAMPS1 has to its south but without wind farms, A2 was shown using the same cases from CLAMPS data for an added comparison of non-waked and waked environments. The case filtering applied here led to limited numbers of cases, which means these findings should be treated as preliminary case studies rather than statistically robust results, as was the case for ARM-CF

fall-winter analysis earlier in the chapter.

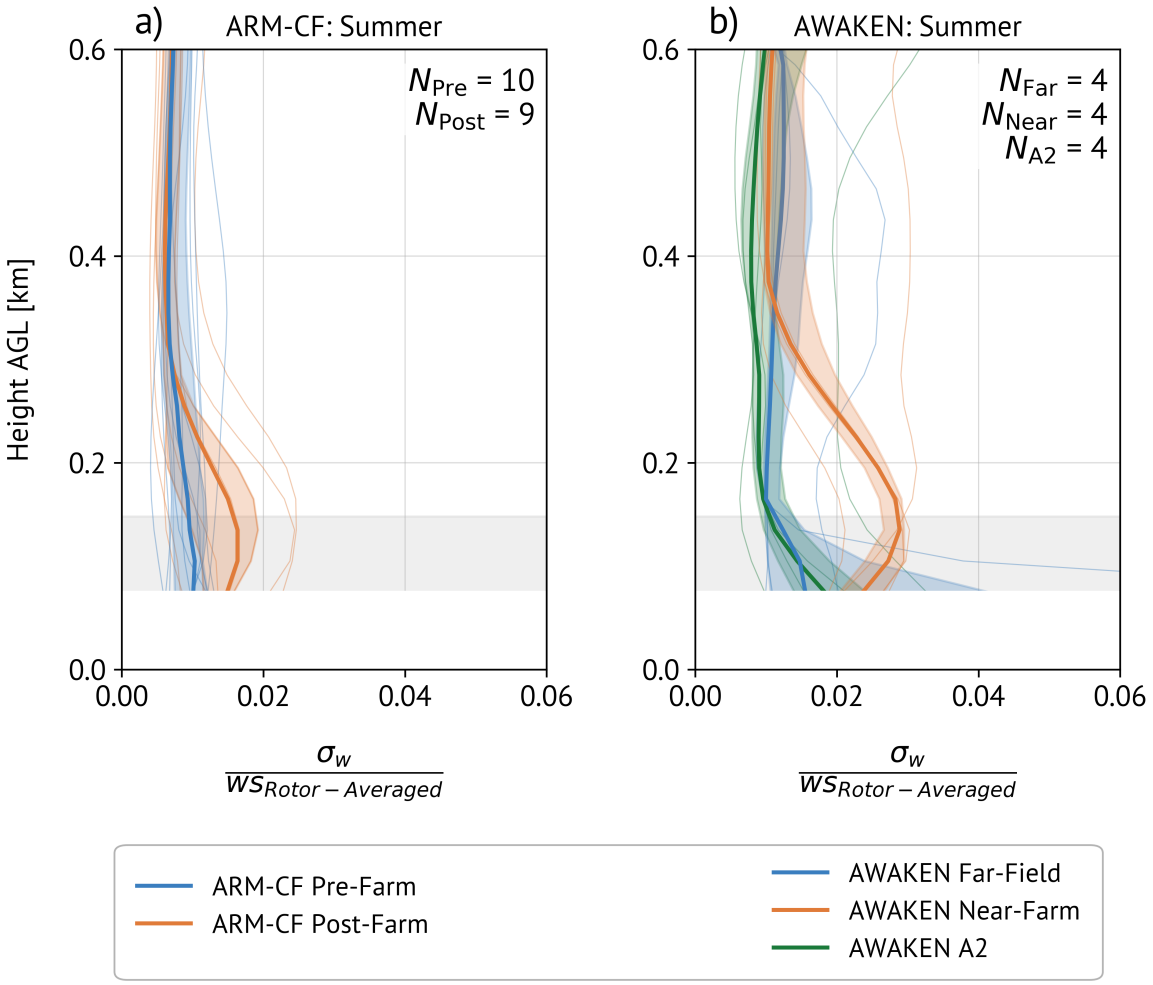


Figure 3.15: Vertical percentiles of normalized σ_w starting at 75m from cases that only contained moderate NLLJs. The median, or 50th percentile, is plotted with outer bounds making up the the 25th and 75 percentiles. Individual profiles that made up the percentiles were shown as thin lines. Gaussian smoothing was applied to reduce noisy returns. The gray horizontal bar represents rotor layer heights.

In Fig. 3.15, all the normalized σ_w profiles showed enhanced σ_w around rotor-layer heights within environments near wind farms (i.e., near-farm and post-farm). Interestingly, this enhancement occurred around rotor levels even when the pre-farm and far-field regimes yielded stronger σ_w aloft. The AWAKEN summertime comparisons in

Fig. 3.15b demonstrated the most pronounced σ_w increases; again, this is hypothesized to be a result of the dense turbine layout of Armadillo Flats leading to stronger mixing signals. Notably, both the A2 and CLAMPS2 profiles increase in the first few range gates before declining to low values σ_w aloft. Although northern Oklahoma is void of rigorous topographical features, flow over even the simple terrain features has been shown capable of helping to induce turbulent mixing in stable nocturnal environments (e.g., Poulos et al. (2002) during CASES-99).

Without observations below 75 m, where measurement noise precludes reliable retrievals, and without collocated surface flux measurements, attributing this near-surface enhancement definitively to terrain effects can only be accomplished with surface-based observations, and even with that information, terrain effects can only be truly eliminated through numerical modeling (see Radünz et al. (2025)). Nonetheless, the enhancements from the non-wakes sites offer a starting point for motivating the design of future observational studies (i.e., the inclusion of surface flux stations that were not available at either CLAMPS site). For now, understanding which NLLJ conditions yield discernible wind farm mixing advances the broader goal of describing when and how wind farms impact the ABL, but such observations in the future could advance understanding of the interplay among shear-driven mixing, wind-turbine-induced turbulence, and the role of surface heterogeneity in shaping the nocturnal ABL.

3.3 Chapter Summary and Implications

The goal of Chapter 3 was to determine if low-level mixing, widely thought to occur from wind farm wakes, remains detectable in the presence of other external sources characteristic to northern Oklahoma, specifically the NLLJ. This was investigated through seasonal comparisons of 1) a single site, ARM-CF, including periods before and

after a wind farm with rows of turbines was operating to the south; and 2) same-day measurements from two different sites during AWAKEN, CLAMPS1 and CLAMPS2, where one was near wind farms with densely clustered turbines while the other was far from any wind farms, assuming southerly flow. From these datasets, we determine how low-level mixing between non-waked and waked environments differ, information that represents a step toward quantifying the broader impacts of wind farms on the ABL. In the summer months, there was stronger low-level mixing from the regimes with nearby wind farms, as anticipated, but the fall-winter periods showed little difference between waked and non-waked conditions in either ARM-CF or AWAKEN datasets.

The NLLJ, which is ubiquitous in the SGP region, was the primary suspect responsible for these seasonal differences, warranting a deeper analysis into its properties during the selected analysis periods. The recently-developed WINDoe algorithm was deemed a reliable application in Chapter 2 for resolving the NLLJ through its full vertical extent, enabling characterization even for elevated jets that have historically been difficult to fully capture from lidar-based VAD-based wind retrievals. Using the information collected from this NLLJ characterization, it was determined that strong NLLJs were a common trait of ABLs during the cooler months, aligning with typical climatological conditions and implying that intense NLLJs cause near-surface mixing even in non-waked environments, which may mask wind farm mixing in the waked ones.

To further evaluate this hypothesis, the strength of each NLLJ in the datasets were classified to compare conditions across sites and assess implications for low-level mixing within and around wind farms. The results indicate limited mixing at all sites under weak or absent NLLJs, but substantial mixing at all sites during strong NLLJ events. Wind farm signals appear most distinct under moderate NLLJ conditions, when enhanced σ_w is identifiable primarily at sites located near wind farms. To investigate

this behavior more quantitatively, a method for determining the ws threshold, or V_T, for shear-driven turbulence was adapted from B15. That study derived V_T using LABLE data (that campaign is described in Chapter 2), which provided a regionally relevant framework. However, their V_T was only representative of AWAKEN datasets and not directly applicable to the broader ARM-CF dataset likely due to differences in seasonal flow characteristics.

Accordingly, seasonal σ_w were computed here from the non-waked regimes of ARM-CF and AWAKEN data. In both datasets, the summertime did not exhibit a strong relationship between σ_w and ws, whereas the fall-winter seasons portrayed a clear σ_w-ws connection, which became the strongest across all rotor heights in the 8-10 $\mathrm{m\,s^{-1}}$ range. The previously analyzed moderate NLLJ classifications aligned closely with this threshold regime, despite being derived solely from summer data. This shows that, although the behavior of V_T is sensitive to environmental conditions, data sampling, and filtering choices, the thresholds derived here can provide an effective indicator for when NLLJ-driven shear is likely to mask wind farm-induced mixing, regardless of the season they occur in. When the analysis was restricted to moderate NLLJ conditions and normalized by rotor-disk averaged ws to remove any other confounding influences, σ_w was consistently enhanced within the rotor-disk regions in both ARM-CF and AWAKEN datasets.

The optimal estimation capabilities of the WINDoe algorithm were shown to effectively characterize the NLLJ and its strength, enabling identification of periods when wind farm effects are most detectable. By furthering those findings to specify threshold ws before wake detection may be obscured by shear effects, this work establishes a framework for future studies to move beyond simple seasonal averages and instead isolate the meteorological conditions under which turbine-induced atmospheric changes are most pronounced. These results also highlight the added complexity that ABL

features like the NLLJ introduce when interpreting wind farm impacts. This is an important consideration given that wind farm-induced mixing is a persistent feature of the nighttime ABL in the regions surrounding wind farms, even if obscured by turbulence from other sources. The relevant NLLJ regimes and associated ws thresholds defined here provide a first step towards contextualizing how wind farms modify the ABL, advancing the field toward more nuanced, regime-based assessments.

Chapter 4

Wind Farm Effects on ABL Height

In the previous chapter, classifying WINDoe-resolved NLLJs by strength helped isolate wind-farm-driven mixing in the lower ABL. Given that turbulent mixing is closely tied to ABL growth, these findings raise the question of whether wind farm effects extend throughout the full depth of the ABL. It is therefore of interest to determine whether wind farms affect the depth of the ABL, H, a parameter widely used to characterize the ABL as it is itself a product of the mixing and thermodynamic processes occurring within it (Stull, 1988; Seibert et al., 2000). As demonstrated in Section 2.3.3, the fuzzy-logic H method performs best when high-resolution w data within the ABL are available, making it well-suited for this purpose. As such, the final goal of this work is to diagnose whether H is influenced by wind farms by applying the comparative framework used in previous chapters (contrasting ARM-CF pre- and post-construction periods and near-farm versus far-field AWAKEN sites) but for the H estimated via fuzzy logic: H_{FL}.

Abraham et al. (2025), hereafter A25, analyzed H during AWAKEN using two approaches. The first, referred to as the turbulence-based method, identified H as the height where vertical velocity variance reached a minimum, drawing from Tucker et al. (2009). The second, referred to as the thermodynamic-based method, followed Heffter (1980) in identifying inversion layers from θ gradients and the magnitude of θ differences across them. Both methods were applied across varying stability conditions, wind directions, and operational states of the wind farms, including curtailed turbine periods

when the power output is deliberately reduced. Under stable conditions typically associated with the nocturnal period, H estimates from both methods were found to be elevated downwind of wind farms in southerly and northerly flow, exceeding 140% above upstream values in the turbulence-based method and 30% in the thermodynamic-based method. These increases were evident during normal turbine operations, whereas H was significantly reduced during curtailed periods, suggesting that surface-based processes can modulate H but that wind farm operation is the primary driver of its most pronounced increases.

These findings provide important insight for understanding wind farm effects on ABL depth in the northern Oklahoma region. However, the two methods employed by A25 remain subject to instrument and processing limitations inherent to their respective data sources. For instance, the turbulence-based method is difficult to reliably interpret in the SBL, where the absence of convectively-generated turbulence complicates H detection, and mixing that is not tied to ABL growth can be detected, leading to erroneous estimates unrelated to true ABL growth. Meanwhile, the thermodynamic-based method becomes ambiguous on nights when inversions are absent or poorly defined. Estimating H in the context of wind farm impacts can be strengthened by collectively harnessing the complementary advantages of Doppler lidar and thermodynamic profiler instrumentation within a single synergistic framework (Kotthaus et al., 2023). The fuzzy-logic H algorithm achieves this by integrating both datastreams and was found to perform well under stable conditions during the 2021 BLISS-FUL campaign, so long as sufficient aerosol loads supporting reliable lidar measurements were present.

To this end, the fuzzy-logic method was applied to evaluate wind farm impacts across the full ABL. Since the fuzzy-logic method integrates the complementary strengths of the instruments underlying both methods in A25, it is hypothesized that

H will similarly be elevated at sites near wind farms, but with more robust estimates than either method alone. The σ_w levels were weaker from ARM-CF than the AWAKEN near-farm site due to the difference in wind farm layouts, therefore H_{FL} is not expected to increase as much near the ARM-CF as by the CLAMPS1 near-farm site. Building on the low-level mixing results of Chapter 3, the current chapter examines whether wind farm impacts extend through the full depth of the ABL, using this fuzzy-logic method as a metric for quantifying those impacts. Should the method prove useful, it offers a practical basis for assessing wind farm impacts accessible to ABL and wind farm researchers since both kinematic and thermodynamic inputs, when available, are more straightforward to obtain and interpret than the complex, research-grade datasets often used to measure wind farm impacts.

4.1 Data and Methods

As detailed in Section 2.2.2 and Smith and Carlin (2024), the fuzzy-logic method estimates H_{FL} by ingesting kinematic inputs, such as w, σ_w, and temporally-weighted inversion height, in a first-generation aggregation step, followed by a second-generation step that incorporates thermodynamic and lidar backscatter measurements as indicators that mixing has occurred. All these types of measurements were available from ARM-CF and AWAKEN sites explored in the previous chapter with 10-minute vertical stares and WINDoe datasets from the Doppler scanning lidars serving as the kinematic inputs, and AERI retrievals processed using TROPoe providing the thermodynamic datastreams (ARM-CF TROPoe retrievals were averaged from a 5-minute cadence to 10 minutes to match the previously used 10-minute lidar timesteps). At times AERI data was not available from CLAMPS, the TROPoe algorithm ingested MWR data instead. Once H_{FL} was processed, composites for southerly wind directions

were computed to compare between non-wind-farm and wind farm regimes.

Note that the requirement for coincident TROPoe retrievals, alongside the existing filtering from Chapter 3, significantly reduced the number of data available to produce HFL estimation compared to the σ_w analysis, particularly during fall-winter. As a result, only summer periods are considered here (ARM-CF post-farm will just be referred to as ARM-CF in this chapter). To help retain data, the clear-sky and T filtering conditions applied at ARM-CF in Chapter 3 were removed, which is justifiable by the BLISS-FUL analysis in Section 2.3.3 indicating H_{FL} aligned well with radiosondes during stable periods regardless of sky conditions, provided that w data quality and vertical coverage in w was abundant.

For the incorporation of inversion height into the fuzzy-logic algorithm, Smith and Carlin (2024) used a time-variable weighting function, which allows the inversion height to have an effect on the algorithm overnight; the ABL evening transition consists of sloped increasing weights while the morning transition consists of sloped decreasing weights. However, implementing inversion height led to AWAKEN and ARM-CF datasets detecting abnormally elevated inversions at times nearing 1 km, a sensitivity that was not present during the summer BLISS-FUL analysis. This occurred whether or not inversions were clearly defined in profiles. When the inversion height consideration in the algorithm was removed, the issue was eliminated. It is possible that version differences between BLISS-FUL TROPoe and AWAKEN TROPoe may be leading to this effect which warrants further investigation, but for the analysis at hand, we simply apply all TROPoe inputs except inversion height into the algorithm.

In addition to H_{FL} averages, we also examined single-day studies to determine how H_{FL} compared with A25 methods and to compare H_{FL} performance between southerly and northerly cases. The same quality controlled steps from A25 were applied to the turbulence- and thermodynamic-based methods here, with a few exceptions. First, A25

produced the turbulence-based method from lidar data collected using six-beam scans. The ARM-CF and AWAKEN lidars performed PPI scans with fewer interruptions in the vertical stares, and these were all processed at the same 10-minute resolution applied for low-level mixing. The second difference is that data quality control here relies on a fixed SNR threshold rather than the dynamic filtering method of Beck and Kühn (2017) implemented in A25.

The H_S radiosonde method from Chapter 2 method was also revisited for the case study comparing H_{FL} and A25 findings. For the ARM-CF site, radiosondes were directly available on-site. Their routine launches span the 0000-1200 UTC window of interest at 0530, 0830, and 1130 UTC, and they are available at a high vertical resolution (Keeler, 2025). There were additional high-resolution Vaisala radiosondes specific to the AWAKEN project launched from site H during limited periods in summer 2023. Since that site was located just north of the King Plains wind farm and closer to the CLAMPS sites (see the map in Fig. 3.1), the site H radiosondes were used as the radiosonde reference for both CLAMPS. However, as denoted in A25, the site H radiosondes traveled an average horizontal distance of 3 km, keeping them well away from turbines under southerly flow; the same considerations apply for ARM-CF radiosondes. Consequently, comparing the radiosondes as a truth measure with the other methods is best served for non-wind-farm environments.

4.2 Results

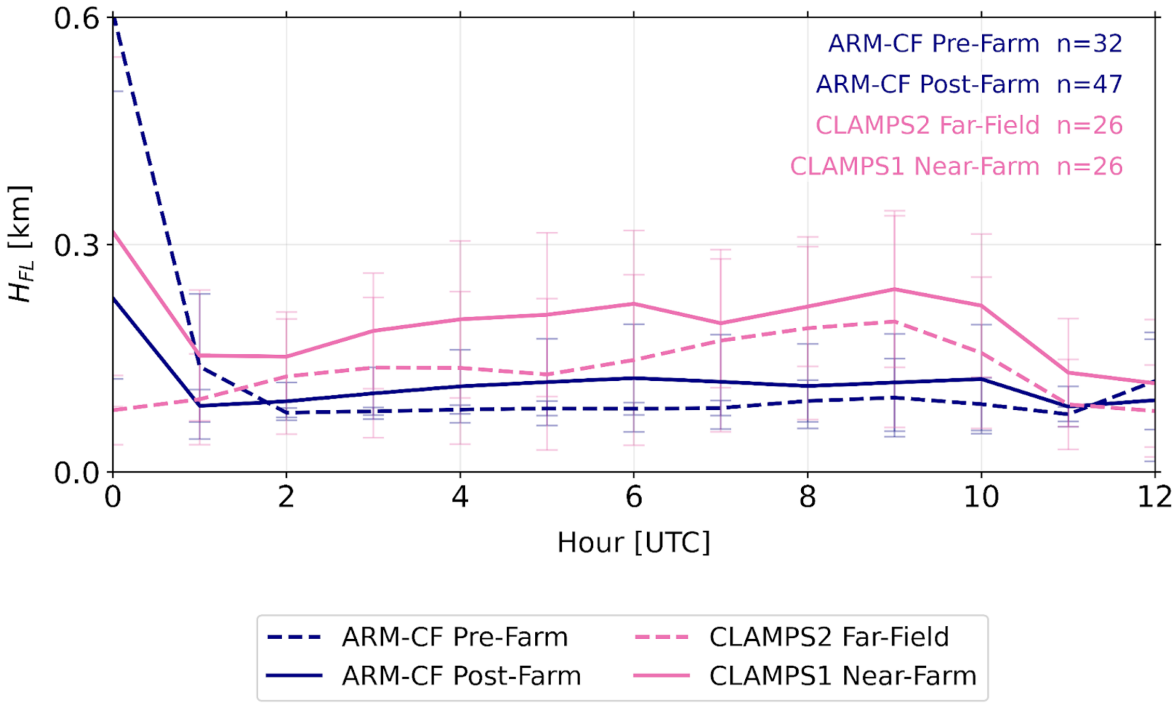


Figure 4.1: Averages from second-generation output of H_{FL} runs for ARM-CF (pre-farm, dashed blue line; post-farm, solid blue line) and CLAMPS (far-field, dashed pink line; near-farm solid pink line) data from the summer periods. At the top right of the panel, the number of samples from each of the plotted averages is listed.

Figure 4.1 shows H_{FL} averaged across all available ARM-CF and CLAMPS cases grouped into wind-farm and non-wind-farm regimes. The clear takeaway is that wind-farm environments produced deeper H than non-wind-farm environments, consistent with the low-level mixing increases shown in Chapter 3. Further evidence of wake-driven deepening is the larger separation between near-farm and far-field H_{FL} relative to the pre- and post-farm H_{FL}, consistent with CLAMPS1 being positioned downwind of a greater number of turbines than ARM-CF. The only exceptions of non-wind-farm H_{FL} surpassing those from wind-farm regimes were during ARM-CF pre-farm periods

in the ABL transitions before 0200 UTC and after 1100 UTC. Wind farms are expected to delay the evening transition and advance the morning transition, which is only reflected in AWAKEN results. Two factors likely explain why this pattern does not emerge at ARM-CF. First, the row-like layout and sparse turbine numbers from Thunder Ranch in the sectors of interest produces wind farm effects detectable during stable nocturnal conditions but are probably insufficient to produce a discernible signal during the convective and transition periods (see Thunder Ranch turbine distance from ARM-CF Fig. 3.6d compared to Armadillo Flats turbine distance to CLAMPS1 near-farm Figs. 3.6e and 3.6f). Second, recall that the T filter applied to the ARM-CF low-level mixing analysis was removed here, which was initially applied to remove cases with extreme conditions disproportionately represented in one set of ARM-CF data but not the other, which could otherwise inflate differences unrelated to wind farm impacts. Without the filter here, extreme conditions in T and other meteorological variables are present and could lead to deeper pre-farm ABLs, as they led to stronger low-level mixing in Fig. 3.7.

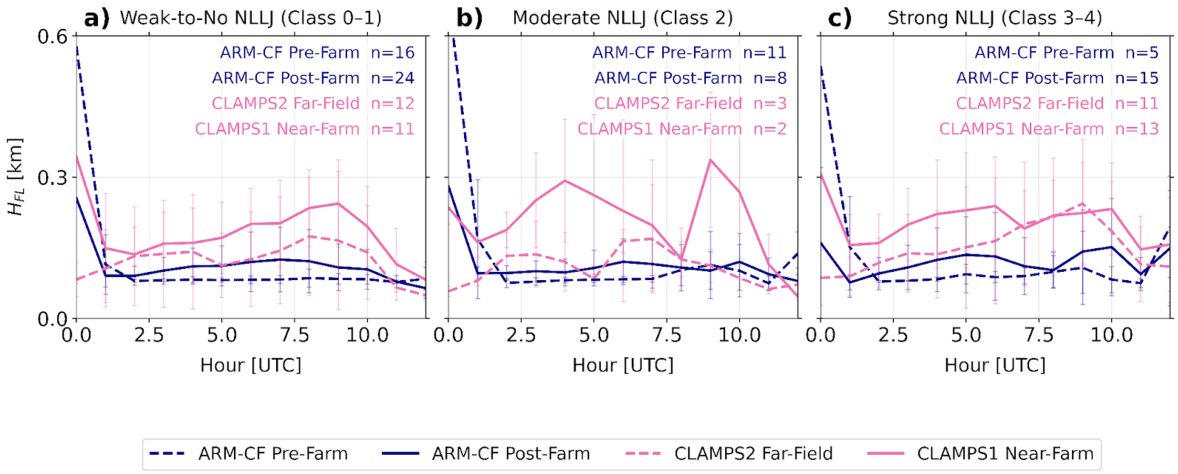


Figure 4.2: As in Fig. 4.1, but categorized by different NLLJ regimes: weak-to no (Fig. 4.2a), moderate (Fig. 4.2b), and strong (Fig. 4.2c).

The same patterns from Fig. 4.1 can be seen in Figure 4.2 across different NLLJ regimes, with only a couple brief exceptions (Fig. 4.2b: ARM-CF at 0900 UTC and Fig. 4.2c: CLAMPS between 0700-0900 UTC). The largest separation between non-wind-farm and wind-farm regimes was between AWAKEN's near-farm and far-field during moderate NLLJs in Fig. 4.2b. This is broadly consistent with the previous chapter's findings of wind farm effects being subdued if the NLLJ is too weak or too strong, which is further speculated with both AWAKEN environments measuring similarly in strong jets between 0700 and 0900 UTC. Still, moderate regimes produced the fewest cases from AWAKEN, and the ARM-CF results do not change much depending on NLLJ strength, limiting confidence in this hypothesis. As a whole, it is determined that the NLLJ still influences H_{FL} to some degree, but extending the analysis beyond rotor levels and incorporating thermodynamic profiles helps suppress direct dynamical influences from the jet that are seen in low-level mixing alone.

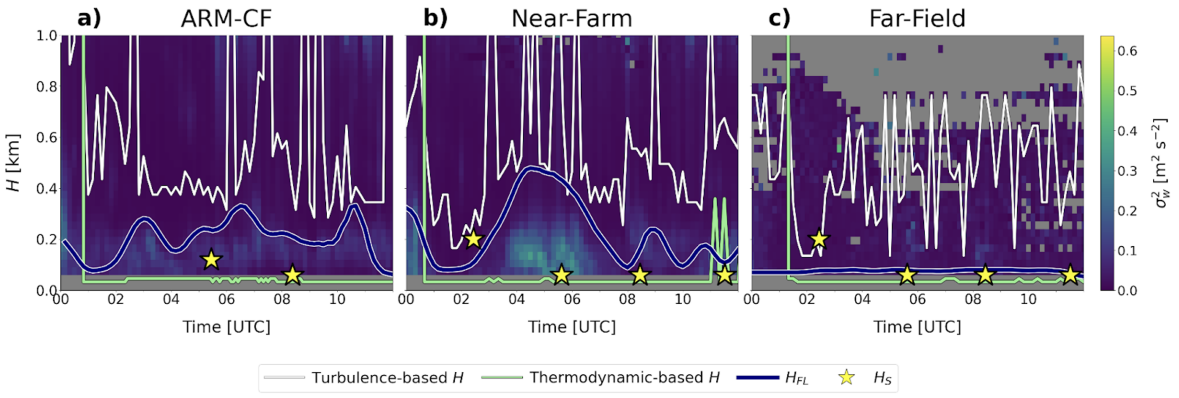


Figure 4.3: Comparisons on 2023-08-17 between ARM-CF, near-farm, and far-field of four H methods: H_S (yellow star), H_{FL} (blue line), the turbulence-based method (white line), and the thermodynamic-based method (green line). Radiosondes originating from the ARM-CF site were displayed alongside with the three H methods from ARM-CF, and radiosondes originating from AWAKEN's site H were displayed with the near-farm and far-field H methods.

The Fig. 4.1-4.2 H_{FL} averages aligned with results from A25, where H from the

thermodynamic-based method and especially the turbulence-based method also increased near wind farms. Figure 4.3 shows H_{FL} alongside the turbulence-based and thermodynamic-based methods in A25 and the H_S for a single case where all methods were available. Though the clear-sky condition was lifted, this case also happened to be cloudless at each site. The background field shows σ_w^2 rather than σ_w to visually amplify mixing signatures among the multiple methods. A consistent finding across each site is that H_S generally struggled to identify the mixing caused by wind farms as expected with the little time radiosondes stayed within the vicinity of the farms. Some of the radiosonde techniques (not shown) measured near H_{FL} levels at 0530 UTC, such as h_θ and h_q in Fig. 4.3a and h_{TOP} and h_q in Fig. 4.3b, but otherwise, none of the techniques posed significant patterns relating to measuring wind farm effects. As a whole, H_S was confined to the near-surface other than during the evening transition, measuring similarly at the three sites.

On the contrary, H_{FL} performs as expected at all sites, increasing in near-farm environments where σ_w^2 alone was strong at rotor levels. In Fig. 4.3a, there were notable enhancements in σ_w^2 not only at rotor levels but also near 1 km, reflecting non-wake sources of mixing aloft. The turbulence-based method tracked these upper-level enhancements and estimated erroneously large H as a result, whereas H_{FL} avoided such extreme values by integrating thermodynamic information to mitigate the influence of kinematic signals not tied to ABL depth. The turbulence-based method did not present much of a difference in H between Figs. 4.3a and 4.3b despite the wind farms near ARM-CF and CLAMPS1 being vastly different in turbine arrangement, but the method at the far-field site (Fig. 4.3c) showed a lower H consistent with its greater distance from wind farm influence.

This shows that the turbulence-based method can be useful to an extent in identifying wind farm impacts on H, but it is also more vulnerable to other sources

of mixing. Meanwhile, the thermodynamic-based method showed little response in wind farm environments overall, with only a marginal increase at ARM-CF during wake-driven periods. These difference in heights between the turbulence-based and thermodynamic-based methods match A25 (see their Figure 7), as do their findings comparing sites upstream and downstream wind farms: they found that when the median H is ≤ 0.25 upstream (here, the far-field site), downstream (the near-farm site), the thermodynamic-based method typically increased only 35-39% compared to the turbulence-based method increase of 143%, which aligns with the Fig. 4.3 findings. The H_{FL} measurements typically traces the background σ_w^2 enhancements well without measuring unrealistically high values from the turbulence-based method, demonstrating the value of integrating multiple kinematic and thermodynamic data it ingests for wind farm analysis.

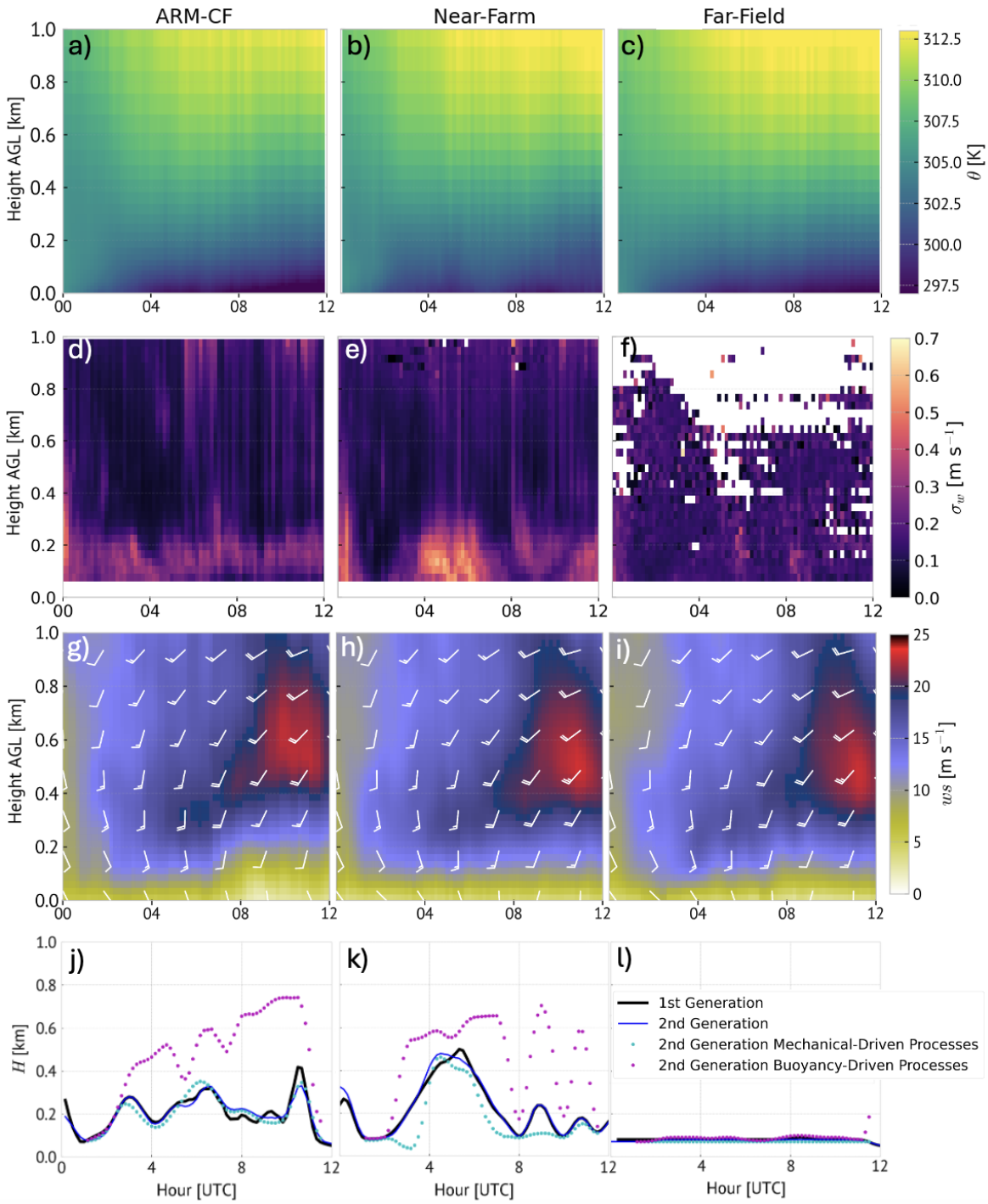


Figure 4.4: The same same 2023-08-17 case used in Fig. 4.3 for ARM-CF, CLAMPS1, and CLAMPS2 and their θ (first row), ws (second row), σ_w (third row), and the first and second generation H_{FL} along with second-generation mechanical- and buoyancy-based drivers (fourth row).

To further diagnose the behavior of the variables governing the turbulence- and thermodynamic-based methods and H_{FL}, Figure 4.4 compares different time-height profiles of key variables from each site. Profiles of θ (Figs. 4.4a-c) are directly used to obtain the thermodynamic-based method. The characteristics of an inversion can be identified in the lowest 0.1 km from all sites, but cool air also extends close to 1 km at all the sites, making a clean inversion top difficult to define. The cool layer near the surface was the least pronounced from the near-farm site of the three sites. This can be explained by mixing from the turbines inducing warming within the rotor layer by entraining warmer air from aloft, eroding the near-surface cool layer.

Yet, this warming effect was minimal or absent from the ARM-CF site despite notable low-level mixing, especially at a site receiving effects from fewer turbines and being further away from them. The ARM-CF site had the strongest cool layer at the surface of the three sites (at 1000 UTC when each had cooling near the surface, the first TROPoe gate showed ARM-CF, near-farm, and far-field measure 295, 298, and 297 K, respectively), which would make warming via mechanical mixing more difficult than at a site with slightly warmer T in the surface layer. That said, it is unknown for sure what the cool layer at the near-farm would look like without the wind farm mixing and only the far-field site can serve as this reference. Altogether, the θ profiles show that the thermodynamic-based method can capture wind farm impacts to some degree, but the magnitude of that signal depends strongly on the specific farm geometry and its influence on the local θ structure.

Figs. 4.4d-f shows σ_w time-height cross-sections (as opposed to σ_w^2 in Fig. 4.3), from which the turbulence-based method originates. These profiles can be compared alongside ws profiles (Figs. 4.4g-i), where a strong NLLJ was measured. Low-level mixing from the two sites close to wind farms was evident even before the NLLJ nose was measured. Fig. 4.4e nicely illustrates differences in near-surface mixing at the near-

farm site primarily caused by 1) decaying convection (before 0100 UTC), 2) wind farms before the NLLJ peaked (0330-0730 UTC), and 3) the NLLJ (0800-1200 UTC). Before, Fig. 4.3 showed the turbulence-based method had evolved linearly with the continuous wind farm mixing signatures throughout the period, however, it also had a tendency to measure elevated mixing near the residual layer. This mainly occurred at the far-field site where heavy filtering on CLAMPS2 lidar data was required to remove noisy returns (see Chapter 2), meaning the turbulence-based method can become compromised when SNR-filtering is applied. Overall, the method can efficiently capture wind farm effects, but it is strongly sensitive to upper-ABL mixing and the choice of lidar noise filtering.

Lastly, Figs. 4.4j-l depict the first and second generation outputs of H_{FL}, as well as the respective contributions of mechanical- and buoyancy-driven effects to formulate its second generation estimate. The H estimated using only buoyancy-related processes in the algorithm was high in comparison to the H produced from mechanically-related processes at the wind farm sites, which was related to deeper cool air. Despite this, the mechanically-generated mixing processes played a large role in shaping the resulting near-farm H_{FL}, and the lack of mechanical mixing from the far-field site supports the hypothesis of the effect of wind farms on H. All in all, the limitations seen in the turbulence- and thermodynamic methods were avoided by H_{FL} and its ability to both kinematic and thermodynamic changes for a more complete characterization of wind farm mixing.

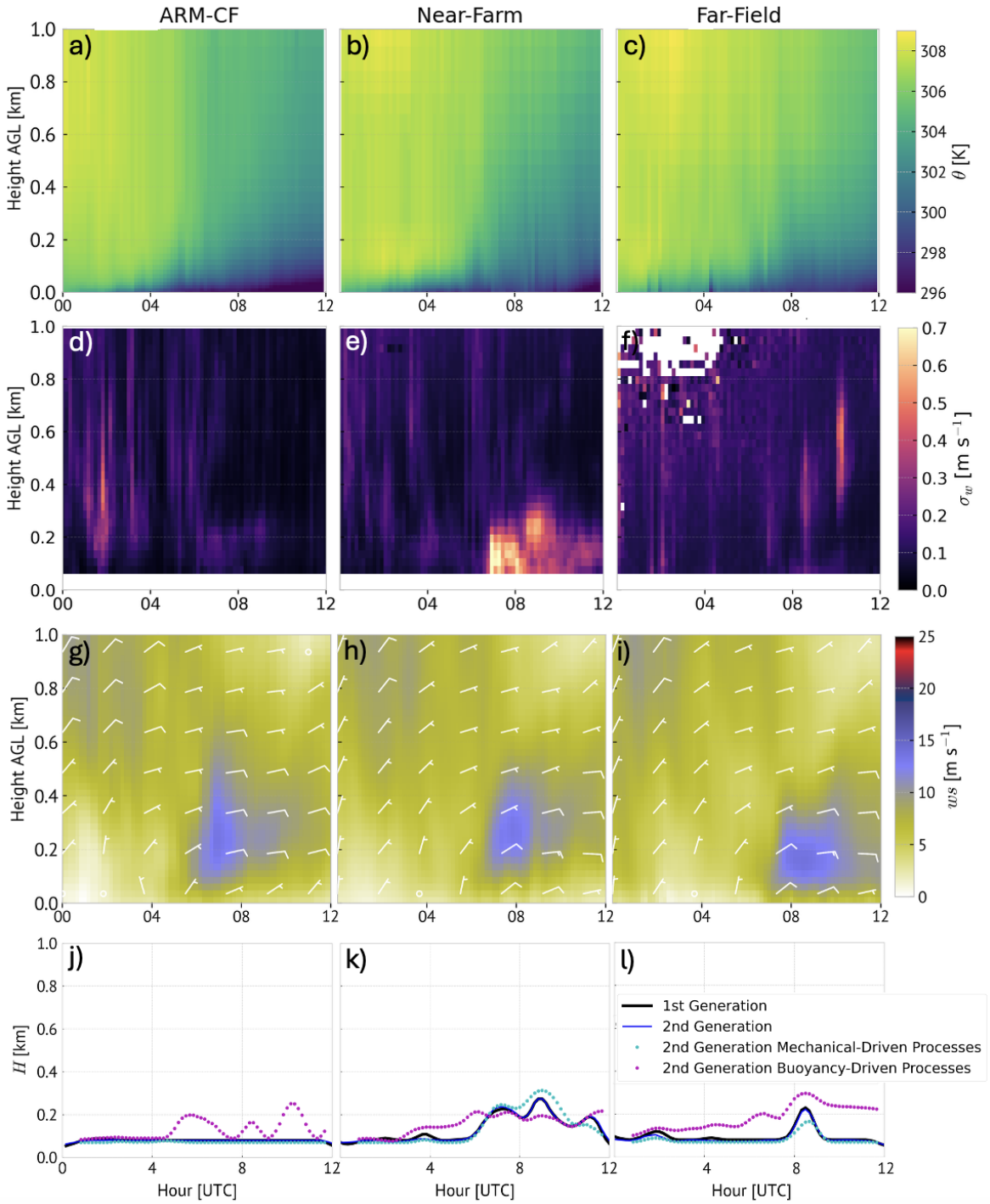


Figure 4.5: As in Fig. 4.4, but for the northerly case of 2023-08-30.

As done in A25, a northerly case was explored in Figure 4.5 as a final confirmation

of increased H_{FL} stemming from wind farms and not simply terrain. With this shift, ARM-CF was no longer downstream of any nearby wind farms (the closest turbine directly north was ∼29 km north from a wind farm called Blackwell), near-farm was downstream of King Plains under north-north-easterly flow. Under flow from the north-north-easterly direction, the far-field site is located 13 km downstream of Armadillo Flats; A25 used the CLAMPS2 data at that far-field site and found the H has begun to recover from wind farm impacts at 13 km downstream but may not be fully recovered at this distance, so it is of interest to note potential far-wake effects. The turbulence- and thermodynamic-based methods are not shown for this case, but they presented similar tendencies as the southerly case.

The θ profiles in Fig. 4.5 depicted a more clearly defined inversion than the southerly case (Figs. 4.5a-c). This helped the buoyancy-related effects in the resulting H_{FL} outputs (Figs. 4.5j-l) to better constrain the ABL top estimate, producing cleaner and more physically consistent H_{FL} retrievals. In the σ_w profiles (Figs. 4.5d-f), ARM-CF measured notable mixing spikes throughout the lower ABL but only after ∼0600 UTC were the increases concentrated at rotor level. This occurred the same time a weak NLLJ developed at all the sites (Figs. 4.5g-i), and it helped induce intense rotor-layer mixing from the near-farm site that was not nearly as strong hours earlier. The wd indicates that the flow was predominantly northerly but shifted to be more northeasterly where the site would be in the direct path of the King Plains turbines. Despite being a weaker NLLJ, the associated flow was strong enough to support the production of turbine-generated wakes that increased mixing, leading to H_{FL} surpassing 0.2 km. In fact, this case resembles Fig. 3.10 from Chapter 3, where even a weak NLLJ could induce weak mixing near the surface.

The far-field H_{FL} was mainly stagnant near the surface, but the site measured brief increases of mixing with height (Fig. 4.5i), specifically when the NLLJ developed.

Similar periodic streaks of high σ_w occur in varying intensities between 0000-0600 UTC at all the sites: those look to be a product of mesoscale-driven events. However, the sporadic instances of enhanced mixing around NLLJ timing appear more structured and less variable than those at earlier times. Many studies have denoted that large-scale, low-frequency oscillations called wake meandering occur downstream of wind farms if there are large turbulent eddies (e.g., Ainslie, 1988; España et al., 2012; Porté-Agel et al., 2020; Brugger et al., 2022). For this reason, we hypothesize that these periodic motions are wake remnants originating from Armadillo Flats that are captured during an amplification phase of wake meandering. Note that the H_{FL} jumped to the level of the second σ_w increase around 0830 UTC, but not the third enhancement, which was stronger and more elongated. In that regard, the behavior of H_{FL} sufficiently captures mixing effects from wind farms as was done using southerly wd, showing the algorithm is a capable metric for H_{FL} estimation among wind farms. However, its performance for sites far downstream like where CLAMPS2 was stationed remains questionable and should be explored in studies yielding more northerly cases and higher data availability within them.

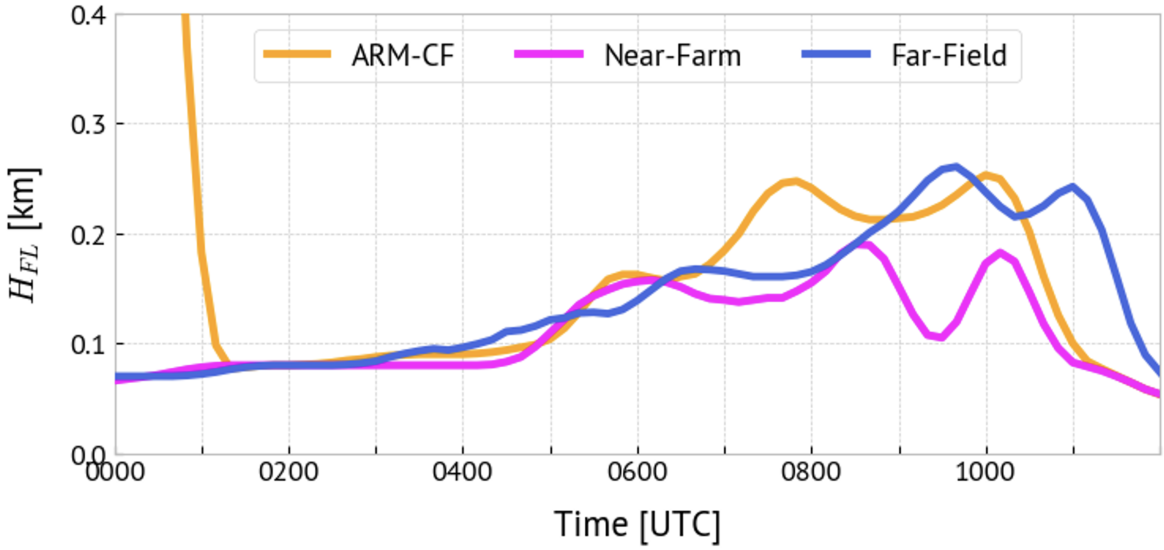


Figure 4.6: Outputs from the second-generation fuzzy-logic algorithm for ARM-CF (yellow line), near-farm (pink line), and far-field (blue line) on 2023-08-16 when turbines are not expected to be operating because rotor-layer winds were less than 3 $\mathrm{m\,s^{-1}}$ throughout the period.

Although we have a good understanding of how the sites compare, factors beyond wind farm operation can influence H between sites, including soil T, soil moisture, surface roughness, and spatial heterogeneity arising from varying crop types across the region (Krishnamurthy et al., 2021b). To determine how these types of features contribute to H results, A25 explored periods during wind farm curtailment, which refers to periods where turbine power generation is deliberately reduced as opposed to normal operations. They found that while other factors do influence H, wind farms remained the dominant driver of H increase. Turbine power output data were not available for the current study; however, 3 $\mathrm{m\,s^{-1}}$ is widely accepted as the cut-in wind speed below which turbines do not generate power (Bodini et al., 2021; Abraham et al., 2025). It is worth examining H_{FL} here for periods without wind farms, where similar findings to A25 helps solidify H_{FL} as a reliable metric for H estimation where factors other than wind farms contribute.

Figure 53 shows H_{FL} from the ARM-CF, the near-farm, and the far-field sites for a case when winds at the rotor layer were less than 3 $\mathrm{m\,s^{-1}}$ throughout the period. During the first few hours, all sites measured similar H_{FL}, aside from the ARM-CF site which showed a delayed evening transition. As the night progressed, the near-farm site consistently produced the lowest measurements, while ARM-CF and the far-field sites produced the highest estimates at different times. Krishnamurthy et al. (2021b) demonstrated that increases in surface and soil T leads to deeper H, and surface composition helps explain the site differences seen here. The ARM-CF sits on sandy soil, which readily absorbs and retains heat; this accounts for both its delayed evening transition and its relatively low morning H_{FL}, as sand is slow to reheat after cooling overnight. By contrast, the near-farm site is adjacent to a golf course where regular irrigation and maintained turf promote cooler, moister surface and soil conditions, consistent with its persistently low H_{FL}. Many ARM-SGP extended sites, including the far-field site, are composed of grassland pasture. These surfaces are expected to have warmer surface temperatures than the irrigated golf course area but cooler than the sandy surface at ARM-CF, which is seen much of the time from the far-field H_{FL}.

The surface characteristics broadly explains the differences in the H_{FL} behavior at the three sites, but one note of interest is the change in patterns between 0800-1000 UTC. There was no NLLJ for this case, but at that time, ABL winds above the rotor layer increased a few $\mathrm{m\,s^{-1}}$ and shifted from southwest to southerly (not shown). This change would not be enough to generate mixing from nearby wind farms (as evidenced by the sharp near-farm H_{FL} decrease). However, the wind shift may have introduced influences from more local surroundings, such as mild terrain effects or advection of air over cropland that gets carried to the site under specific *wd*. The exact timing of crop growth and harvesting at each site is unavailable, but Bagley et al. (2017) detailed how crop type in the SGP modulated surface T, fluxes, and moisture properties that

ultimately contribute to H; the same effect could be present here, but warrants a deeper investigation.

Overall, the findings of our study show that wind farms produce the most substantial increases in ABL depth, especially at the near-farm site. These findings match A25 results, but measurement quantities from H_{FL} were shown to present more realistic H estimates than the turbulence- or thermodynamic-based methods alone, matching the expected ABL altitudes and evolution based on Stull (1988). The information presented in this chapter underscore the impacts of wind farms on the ABL. Our study also highlights the importance of integrating accurate and high-resolution measurements of thermodynamic and kinematic ABL properties, which is accomplished by using the fuzzy-logic algorithm H_{FL}.

4.3 Chapter Summary and Implications

In the Chapter 3, enhanced low-level mixing downwind of wind farms was confirmed near rotor level at two different sites. This provided clear evidence of ABL alterations caused by wind farms near the surface, but it was still an open question whether those effects extended through the entire ABL. Building on the evaluation from BLISS-FUL data in Chapter 2, the novel fuzzy-logic algorithm was employed to compute H_{FL} as a parameter for characterizing the entire ABL and to determine if the fuzzy-logic algorithm is a suitable metric for measuring wind-farm impacts.

Both composited and case study results confirm wind-farm effects in the same environments where low-level mixing was enhanced in Chapter 3, but here there was not as strong of a dependence on NLLJ strength when considering the entire ABL compared to the impacts on σ_w at rotor-disk levels. Methods from A25 (one based on turbulence and thermodynamic) were explored in a southerly case study to compare

with H_{FL}. Radiosondes could not capture wind-farm effects well due to winds carrying them away from wind farms immediately after launch. The H estimated with the turbulence-based method increased around wind-farm environments as in A25, but the method was also extremely sensitive to filtering by SNR and upper-ABL mixing not necessarily related to wind farms. The thermodynamic-based method also reflected A25 results, displaying increases within wind farm environments but still measuring shallow H even during those increases.

The newly-developed fuzzy-logic method consistently captured wind farm effects without ever producing uncharacteristically high values like the turbulence-based method or extremely low values like the thermodynamic-based method. Even when assessing a northerly case when wind farm effects would no longer be present at ARM-CF, the H_{FL} at the near-farm site where effects are expected does suggest the presence of such effects. This shows its utility as a proxy for H estimation near and away from wind farms, again, provided w data is not inhibited by systematic or external effects.

The findings from this chapter showcase the value of leveraging a synergistic approach which combines multiple high-resolution datastreams rather than relying on a single indicator. While H_{FL} shows strong promise as a quasi-measure of wind farm impacts on the ABL when the measurements occur close enough to fully capture wake effects, there was more ambiguity from the fuzzy-logic algorithm when measuring what was suspected to be wake remnants at a location far downstream from the farms. Future work should investigate how far downstream the algorithm can successfully capture wake effects as part of ABL growth. The novelty of the method also offers other avenues for exploration, including the full 24-hour cycle, different stability conditions, or testing around offshore wind farms or within rigorous topography whenever high-resolution datasets needed in the algorithm are available. Overall, the results highlight the strong relationship between coupled kinematic-thermodynamic properties within

the ABL and how human-made structures like wind farms can measurably disrupt the layer's overall structure and depth.

Chapter 5

Conclusions and Future Work

The ABL is a complex and highly variable part of the atmosphere that is closely linked to surface processes and therefore susceptible to changes caused by human activities. Wind farms, for example, have been shown in numerous observational, wind tunnel, and modeling studies to influence their surrounding local meteorology. Yet, observing their effects on the ABL is challenging to rectify due to gaps in observational coverage, despite being vital information for forecasting, numerical modeling, and fieldwork planning as wind farms rapidly expand. Additionally, ABL characteristics vary across different regions, raising questions about how specific ABLs respond to wind farm activity and how such responses can be identified despite observational gaps.

Recent advances in ABL research techniques, including observing system and data retrieval algorithms, provide researchers with new methods to better characterize the ABL and its features. These newly-developed tools offer an innovative framework for studying the impacts of wind farms throughout the boundary layer. One novel algorithm extends vertical ABL winds using an optimal estimation approach (Gebauer and Bell, 2024), which can be applied to recover NLLJs that traditional lidar-based retrieval approaches can not fully resolve. The second approach ingests kinematic and thermodynamic ABL profiles to produce a temporally-continuous H (Smith and Carlin, 2024), a parameter that directly depends on ABL turbulent processes and can therefore be utilized to characterize the evolution of the ABL (Stull, 1988; Seibert et al., 2000). Both algorithms have shown promising results on datasets collected in the SGP, as

these new approaches have not been previously applied to analyze wind-farms-ABL interactions. With the availability of high-resolution observations from both a long-term climatological facility and a specially-targeted wind-farm-based field campaign, this dissertation aimed to apply these algorithms to gain new insight into wind farm impacts, specifically turbulent wakes, on ABL properties.

Before examining wind farms and their associated mixing properties, the initial objective of this work was to evaluate the performance of the two newly developed algorithms using high-resolution datasets from field campaigns conducted in Oklahoma, within or near the same domains targeted for wind farm analysis. When applied to co-located lidars and compared to traditional VAD retrievals, the optimal estimation wind algorithm, WINDoe, produces favorable increases in wind coverage, particularly overnight. As with VADs, the WINDoe retrievals were subject to greater uncertainty deep in the ABL when the lidar scanned at a low elevation angle. The primary motivation for employing WINDoe in this study was its ability to resolve the vertical extent of NLLJs that are not always fully captured by VAD retrievals alone. WINDoe was found to best achieve that using a high elevation angle at 70° compared to a lower, 40° angle, where observations extend deeper in the ABL. This shows that WINDoe prioritizes observational constraints where they exist and propagates toward prior uncertainty where they do not; to this end, the 70° configuration was determined to best support accurate NLLJ resolution and was therefore employed in all subsequent analyses. WINDoe achieves extending wind profiles through its optimal estimation framework, using layer-to-layer correlations to distribute information content throughout the retrieved profile. Also, since the upper portion of the NLLJ is typically not far above the levels where VAD observations terminate, WINDoe is not simply reverting to the prior climatology in this critical layer. Rather, it produces physically constrained retrievals that reflect the information content carried by the available observations. ABL researchers

interested in other deep layer phenomena like the NLLJ, including storm systems or high-altitude gravity waves, can leverage this knowledge, both in terms of wind farm implications or general ABL analysis.

The second algorithm considered in this work was a fuzzy-logic based H retrieval method. This algorithm was found to also demonstrate promising performance when compared to radiosonde-derived H serving as reference "truth" measures. Using a range of observational datasets with varying operating strategies, this dissertation assessed how sensitive the fuzzy-logic algorithm is to the characteristics of its input data. The results show that high-temporal-resolution w measurements, such as 1-second vertical stare observations, yield more accurate fuzzy-logic method estimates compared to coarser resolutions (e.g., 10-seconds or longer). In contrast, the algorithm exhibited relatively low sensitivity to the temporal resolution of horizontal wind measurements from PPI scans, with increased sampling frequency producing little change in the resulting estimates. While ws and thermodynamic variables remain important inputs, coarser temporal resolution has a relatively minor impact on algorithm outputs compared to vertical resolution. Agreement between H_{FL} and radiosonde H_S estimates was strongest during periods with abundant aerosol loading to enhance lidar signal quality, which motivated the exclusion of cases within 24 hours of precipitation events later in the study. Relying on high aerosol loads suggests H_{FL} has reduced applicability in environments with persistently low aerosol concentrations, such as mountainous regions. Future work should aim to define a more precise relationship between the vertical extent of vertical stares data availability and performance of the fuzzy-logic method, including long-term testing across diverse atmospheric conditions. The H_{FL} also showed the best agreement with radiosonde estimates under stable conditions; during daytime periods it occasionally estimated lower altitudes. This behavior is also reported by Smith and Carlin (2024), who attribute it to the tendency of ground-based remote sensing

instruments to favor the lowest detectable estimate of H (e.g., the bottom of an entrainment layer), especially when the H extends deep into the ABL during convective conditions. This indicates that caution is warranted when interpreting the output under convective conditions, however, the present work focuses on the 0000-1200 UTC period (overnight) in which wind farm wakes are expected to be most persistent and easier to identify. Overall, the fuzzy-logic algorithm, together with WINDoe, provides reliable and physically consistent outputs suitable for analyzing wind farm impacts on the ABL in northern Oklahoma.

After determining that the algorithms are well suited for the purposes of this dissertation, we set off analyzing wind farm modifications by starting with low-level mixing, a widely used method to measure wake effects from operating wind farms. Comparisons were conducted between environments expected to be influenced by wind farms and environments where influences are not expected using two observational frameworks: one based on ARM-CF measurements collected before and after the construction of a wind farm with turbines arranged in a row-like configuration, and another from the AWAKEN campaign, where the two OU–NSSL CLAMPS platforms were deployed far from wind farms and near a site with densely clustered turbines. Locations nearby wind farms had profound increases in low-level mixing during warmer months, but in the colder months there was virtually no difference between the waked and non-waked environments. In some cases, non-waked environments even showed stronger mixing during colder months.

In the SGP region, the NLLJ is a frequently occurring phenomenon, and climatology suggests that the NLLJ has pronounced seasonal variability. To understand if the NLLJ may be related to some of the differences noted in waked and non-waked environment comparisons, this work included an inspection of WINDoe-derived NLLJs to characterize their behavior during the periods of interest. Stronger NLLJs occurred

in the colder seasons as is climatologically typical, which could be important for the identification of the wind farm signal. When investigated across AWAKEN sites, it was shown that NLLJs serve as an energy resource for wind farm operation, but exceptionally strong NLLJs appear to suppress or obscure the expected wind farm signal (i.e., downstream turbulent mixing). To identify the ws regime at which shear-driven turbulence becomes significant in the environment and would therefore confound identification of wind-farm driven turbulence, we applied a critical wind speed threshold approach following Bonin et al. (2015) to the datasets. The resulting thresholds define representative ws at rotor levels at which shear effects become prominent, regardless of the season. These results indicate that moderate-strength NLLJs provide flow conditions sufficient to sustain turbine operation, while remaining below the threshold where shear-generated turbulence begins to dominate and obscure wind farm mixing signals. It is within this moderate regime that wind turbines emerge as the primary driver of enhanced rotor-layer mixing, as their mechanical and wake-induced turbulence operates against a background that would otherwise remain relatively quiescent. Recognizing this regime therefore provides a physically grounded framework for isolating wind farm mixing signals in future observational studies targeting the SGP, where NLLJ variability would otherwise complicate this understanding.

With confirmation of wind farm effects in the lower levels, the impact of wind farms on the entire ABL was quantified based on H_{FL}. A similar approach was employed by Abraham et al. (2025), who reported increases in H downstream of wind farms, but relied on separate turbulence-based and thermodynamic-based estimates as H definitions. Applying the fuzzy logic approach described earlier in the dissertation ingests multiple datasets into a unified framework, avoiding limitations of kinematic- or thermodynamic-only H estimation methods. The resulting H_{FL} estimates showed deeper boundary layers in environments near wind-farms. Despite the importance of

NLLJ strength in modulating low-level wind farm mixing signals, H_{FL} showed limited variation both across NLLJ regimes and between near-farm and far-field environments. This finding differs from the low-level mixing results where determining wind farm effects was closely tied to the strength of the NLLJ; it suggests that the ABL-scale response to wind farm activity is not solely dependent on NLLJ-driven rotor-layer mixing and that H_{FL} integrates contributions across a broader range of conditions, such as radiative cooling, than NLLJ-driven effects alone would indicate. Taken together, these results support the fuzzy-logic method as a reliable proxy for H estimation across wind farm and non-wind farm environments alike, and its ability to consistently distinguish near-farm from far-field conditions positions it as a useful tool for future wind farm impact studies.

One area requiring further investigation is the spatial extent that wind farm wakes can be detected based on H. This notion became evident when analyzing cases with different wd, in which a site typically located outside wind farm influence was positioned downwind of more distant turbines. In these situations, H_{FL} did not consistently show a response above the rotor layer, which likely reflects the nature of the wakes themselves rather than a limitation of the algorithm. Elevated, dissipating wakes at greater distances from the farm are expected to produce weaker and more diffuse turbulence and thermodynamic signatures than near-field wakes, and it is not clear that such signatures would be expected to manifest as a detectable change in H regardless of the estimation approach employed. This raises an open physical question about the conditions under which extended (and elevated) wakes produce ABL-scale responses, and motivates future work examining the fuzzy-logic algorithm across a range of downwind distances to better characterize how, and at what scales, wind farm signals manifest in H. Additional work should also examine the sensitivity of H_{FL} to internal algorithm settings, including the weights applied to the inversion height and the 0.5 aggregation

threshold, as either could influence how subtle or diffuse wind farm signatures are represented in the resulting output. Different versions of TROPoe, particularly those that represent inversion heights differently, may interact with these sensitivities in ways that are not yet fully understood. A dedicated analysis into how the fuzzy-logic algorithm behaves under certain settings and across different retrieval configurations would provide necessary insight into the conditions under which the fuzzy-logic method can be most confidently applied and interpreted in wind farm environments.

The work presented here incorporates rich observations with high temporal and vertical resolution that are rare to obtain. While the algorithms themselves were shown to be useful and are in many ways flexible to apply, the minimum data required to apply the algorithms are typically not available in most locations worldwide, making wind farm effects in some areas difficult to determine. In general, Oklahoma is a popular testbed for many research applications for its severe weather occurrences alone; as such, it supplies a wealth of information from ARM-SGP, the NWC, and the many field campaigns that routinely take place in the area. Plus, even using such observations, cases became limited due to continuous data availability limitations and the limitations of the observations themselves (i.e., WINDoe is most efficient when it ingests a climatological prior consisting of several years of past observations) can be challenging.). In general, the availability of such specialized observation datasets is growing, but these findings affirm their necessity in meteorology and wind farm research. Given the novel nature of these algorithms, there is plenty of room for expansion and updates that may assist in these caveats, but for now, these considerations should be kept in mind when seeking their application. In general, quantifying the relationship between wind farm driven effects and the evolution of H can provide a pathway to determine the impacts of wind farms in regions with less specialized observing systems.

There are additional opportunities to refine the present study. For example, turbine

operation was inferred in a manner similar to Bodini et al. (2021), but incorporating actual turbine power output data would provide a more direct assessment. Moreover, separating cases by atmospheric stability at ARM-CF, rather than by time period alone, could also improve interpretation. In this study, the lack of flux data and episodic thermodynamic profiling data made this difficult to achieve at all sites. Given that Oklahoma is frequently impacted by extreme weather, extending this analysis to examine how wind farm-induced modifications to the ABL influence such events (and vice versa) is a natural next step. Another area that would benefit by more targeted investigation is the impact of wind farm layout orientation, which was shown here to possibly produce different low-level mixing responses at ARM-CF compared to CLAMPS1, particularly under varying NLLJ regimes. It would also be useful to investigate evolution of the ABL throughout the full ABL cycle of evolution, particularly during evening and morning transition periods, as the few results on the topic thus far are consistent with findings from Fitch et al. (2013) and Rajewski et al. (2020). In addition, numerical model simulations could extend these results beyond observational limitations, providing a more comprehensive understanding of the processes involved across time and space.

Overall, this work exemplified the importance of accounting for wind farm effects on the ABL, the atmospheric layer in which weather and life occur. Wind farms continue to expand in both number and rotor-disk size, reinforcing the need for studies to explicitly consider their influence. Improved understanding of wind farm-ABL interactions provide beneficial information to both wind energy and atmospheric science communities. For wind energy applications, it helps identify where and when turbines can most effectively harness features such as the NLLJ. For ABL research, it provides valuable insight for forecasting and field campaign planning. The findings revealed here show these traditionally separate areas of study and interest to be closely con-

nected and should be treated in tandem. Once a more integrated, interdisciplinary step is achieved, researchers can progress towards the comprehensive network of high-resolution, long-term observations that will strengthen ABL and wind farm analyses moving forward.

Appendix A

Table A.1: ARM-CF instrument configuration settings used across the analysis period.

Settings	Summer 2011 – Summer 2012	Summer 2012 – Fall 2015	Summer 2016 – Summer 2023
AERI			
TROPoe Retrieval Temporal Resolution	5 min	5 min	5 min
TROPoe Upper-Level Model	RAP 4–20 km	RAP 4–20 km	RAP 4–20 km
TROPoe Version	0.11 up until fall 2017	Fall 2017 Oct. 16th onward: 0.9	0.9
TROPoe Prior (First Guess)	ARM-CF Radiosondes	ARM-CF Radiosondes	ARM-CF Radiosondes
Lidar			
Vertical Staring Temporal Resolution	Continuously except during PPIs	Continuously except during PPIs	Continuously except during PPIs
Vertical Staring Sampling Frequency	1 sec	1 sec	1 sec
PPI Cadence	Hourly	10–15 min	10–15 min
PPI Azimuths	72	8	8
PPI Elevation	24° until Dec. 2011; then 40°	60°	60°
PPI Scan Duration	∼2.5 min	∼0.5–1 min	∼0.5–1 min
WINDoe Retrieval Temporal Resolution	10 min	10 min	10 min
WINDoe Prior (First Guess)	ARM-CF Radiosondes	ARM-CF Radiosondes	ARM-CF Radiosondes
WINDoe SNR Minimum (dB)	−20	−20	−50
WINDoe SNR Maximum (dB)	10	10	10
WINDoe Time Window per Retrieval	30 min	30 min	30 min
WINDoe N (Number of Samples for Calculating Lidar Error; -1 is Actual N)	−1	−1	−1 (actual N)
WINDoe Sigma Value to Filter Noise from Profile Estimate	4	4	4
WINDoe Range of Lidar Observations Used	0.1–5 km	0.1–5 km	0.1–5 km

Table A.2: CLAMPS instrument configuration settings used across the analysis period.

Settings	Fall-Winter 2022	Summer 2023
AERI or MWR		
Retrieval Cadence	10 min	10 min
Upper-level Model	RAP 4–18 km	RAP 4–18 km
TROPoe Version	0.6	0.6
TROPoe Prior (First Guess)	OUN Radiosondes	OUN Radiosondes
Lidar		
Vertical Staring Cadence	Continuously except during PPIs	Continuously except during PPIs
Vertical Staring Temporal Resolution	1 sec	1 sec
PPI Cadence	15 min (CLAMPS1), 10 min (CLAMPS2)	10 min
PPI Azimuths	10 (CLAMPS1), 8 (CLAMPS2)	8
PPI Elevation	70°	70°
PPI Scan Duration	∼0.5 min	∼0.5 min
WINDoe Retrieval Temporal Resolution	10 min	10 min
WINDoe Prior (First Guess)	ARM-CF Radiosondes	ARM-CF Radiosondes
WINDoe SNR Minimum (dB)	−50	−50
WINDoe SNR Maximum (dB)	10	10
WINDoe Time Window per Retrieval	30 min	30 min
WINDoe N (Number of Samples for Calculating Lidar Error; -1 is Actual N)	−1	−1
WINDoe Sigma Value to Filter Noise from Profile Estimate	4	4
WINDoe Range of Lidar Observations Used	0.1–5 km	0.1–5 km

Appendix B

Table B.1: ZephIR-300 lidar configuration settings used during the Fall-Winter 2022 deployment.

Settings	Fall-Winter 2022
Lidar	
Wind Temporal Resolution	15 sec (10-minute Averages Available)
Wind Range of Observations	10, 20, 30, 38, 50, 60, 70, 80, 110, 140, and 180 m

Combining Z773 and Z345 observations with CLAMPS VADs was useful to early AWAKEN analyses to extend wind coverage near the surface. To understand the utility of the co-located datasets, we investigated the value of using 2022 fall-winter data from ZephIR 300 profiling lidars and CLAMPS SNR-filtered scanning lidars together (Figure B.1). Since the scanning and profiling lidars are different platforms with different configurations and operating techniques, measurement levels do not necessarily match, but it is still worth comparing the closest overlapping heights between the CLAMPS and ZephIR observations (180 m for the ZephIR 300 lidars and 183 m for the CLAMPS lidars; Figs. B.1c-B.1d) and a visual of how the combined time-height cross-sections appear (Figs. B.1e-B.1f). The data used here is quality controlled, but not filtered by southerly or nocturnal conditions. With all this under consideration, observations were overall well-matched throughout the campaign and in the chosen case. Later in the analysis period, WINDoe was published Gebauer and Bell (2024) and applied

to the AWAKEN datasets. While it was determined that including the ZephIR lidar data in WINDoe alongside CLAMPS lidar data was not advantageous (Section 3.1.2), confidence in the ZephIR data quality is important to be able to use them as verification of the WINDoe profiles derived from CLAMPS lidar data.

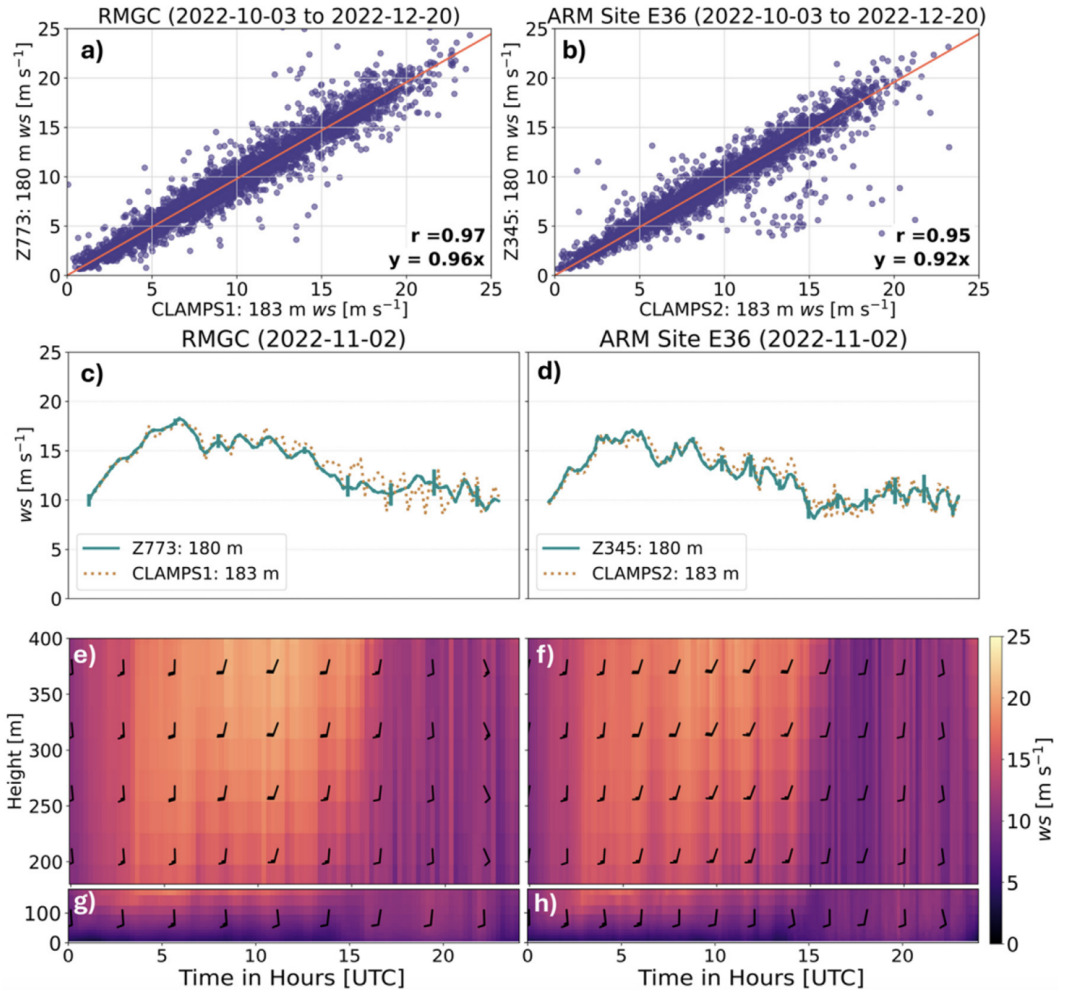


Figure B.1: Evaluation and combination of *ws* data from the ZephIR and CLAMPS lidars. The left column shows data from the near-field site, Rolling Meadows Golf Club (RMGC), collected by CLAMPS1 and Z773. The right column shows data from the far-field site of E36, collected by CLAMPS2 and Z345. Panels B.1a and B.1b show for each site, respectively, a scatterplot of winds at the measurement height closest to 180 m (exact for ZephIR, 183 m for CLAMPS) from the entire winter campaign. Panels B.1c and B.1d show a time series of winds at the same measurement heights on 2 November 2022 with error bars corresponding to the standard deviation of averaged ZephIR data. Finally, panels B.1e and B.1f are time-height cross sections of CLAMPS wind speed observations with wind barbs overlaid, also for 2 November 2022. Panels B.1g and B.1h, showing the ZephIR lidar wind speed observations in a similar way, are meant to combine with panels B.1e and B.1f above to demonstrate the two lidars as a complementary profile.

Reference List

Abkar, M., and F. Porté-Agel, 2013: The effect of free-atmosphere stratification on boundary-layer flow and power output from very large wind farms. *Energies*, **6 (5)**, 2338–2361, https://doi.org/10.3390/en6052338.

Abkar, M., A. Sharifi, and F. Porté-Agel, 2016: Wake flow in a wind farm during a diurnal cycle. *Journal of Turbulence*, **17 (4)**, 420–441, https://doi.org/10.1080/14685248.2015.1127379.

Abraham, A., and Coauthors, 2025: Operational wind plants increase planetary boundary layer height: an observational study. *Wind Energy Science*, **10 (8)**, 1681–1705, https://doi.org/10.5194/wes-10-1681-2025.

Acevedo, O. C., and D. R. Fitzjarrald, 2001: The early evening surface-layer transition: Temporal and spatial variability. *Journal of the Atmospheric Sciences*, **58 (17)**, 2650–2667.

Ahsbahs, T., A. Peña, A. N. Hahmann, and R. J. Barthelmie, 2020: Offshore wind farm wake interactions observed with lidar measurements. *Wind Energy Science*, **5 (2)**, 411–428, https://doi.org/10.5194/wes-5-411-2020.

Ainslie, J. F., 1988: Calculating the flowfield in the wake of wind turbines. *Journal of Wind Engineering and Industrial Aerodynamics*, **27**, 213–224, https://doi.org/10.1016/0167-6105(88)90037-2.

Allaerts, D., and J. Meyers, 2019: Sensitivity and feedback of wind-farm-induced gravity waves. *Journal of Fluid Mechanics*, **862**, 990–1028, https://doi.org/10.1017/jfm.2018.969.

Ao, C. O., T. K. Chan, B. A. Iijima, J.-L. Li, A. J. Mannucci, J. Teixeira, B. Tian, and D. E. Waliser, 2008: Planetary boundary layer information from gps radio occultation measurements. *GRAS SAF Workshop on Applications of GPSRO Measurements, 16–18 June 2008*, 123–131.

Ao, C. O., D. E. Waliser, S. K. Chan, J.-L. Li, B. Tian, F. Xie, and A. J. Mannucci, 2012: Planetary boundary layer heights from gps radio occultation refractivity and humidity profiles. *Journal of Geophysical Research: Atmospheres*, **117 (D16)**.

Astling, E. G., J. Paegle, E. Miller, and C. J. O'Brien, 1985: Boundary layer control of nocturnal convection associated with a synoptic scale system. *Monthly Weather*

Review, **113 (4)**, 540–552, https://doi.org/10.1175/1520-0493(1985)113⟨0540:BLCONC⟩2.0.CO;2.

Atmospheric Radiation Measurement (ARM) Climate Research Facility, 2022: Arm-sgp's central facility (arm-cf) and extended sites: Continuous abl observations since the early 1990s. *ARM Data Archive*, **1**, 1–10, https://doi.org/10.5439/1234567.

Aubrun, S., S. Loyer, P. E. Hancock, and P. Hayden, 2013: Wind turbine wake properties: comparison between a non-rotating simplified wind turbine model and a rotating model. *Journal of Wind Engineering and Industrial Aerodynamics*, **120**, 1–8, https://doi.org/10.1016/j.jweia.2013.06.007.

Bagley, J. E., L. M. Kueppers, D. P. Billesbach, I. N. Williams, S. C. Biraud, and M. S. Torn, 2017: The influence of land cover on surface energy partitioning and evaporative fraction regimes in the u.s. southern great plains. *Journal of Geophysical Research: Atmospheres*, **122**, 5793–5807, https://doi.org/10.1002/2017JD026740.

Baidar, S., T. J. Wagner, D. D. Turner, and W. A. Brewer, 2023: Using optimal estimation to retrieve winds from velocity-azimuth display (vad) scans by a doppler lidar. *Atmospheric Measurement Techniques*, **16**, 3715–3726, https://doi.org/10.5194/amt-16-3715-2023.

Baidya Roy, S., and J. J. Traiteur, 2010: Impacts of wind farms on surface air temperatures. *Proceedings of the National Academy of Sciences*, **107 (42)**, 17 899–17 904, https://doi.org/10.1073/pnas.1000493107.

Banghoff, J. R., D. J. Stensrud, and M. R. Kumjian, 2018: Convective boundary layer depth estimation from s-band dual-polarization radar. *Journal of Atmospheric and Oceanic Technology*, **35 (8)**, 1549–1564, https://doi.org/10.1175/JTECH-D-17-0210.1.

Banta, R. M., 2008: Stable-boundary-layer regimes from the perspective of the low-level jet. *Acta Geophysica*, **56 (1)**, 58–87, https://doi.org/10.2478/s11600-008-0010-0.

Banta, R. M., R. K. Newsom, J. K. Lundquist, Y. L. Pichugina, R. L. Coulter, and L. Mahrt, 2002: Nocturnal low-level jet characteristics over Kansas during CASES-99. *Boundary-Layer Meteorology*, **105 (2)**, 221–252.

Banta, R. M., Y. L. Pichugina, and W. A. Brewer, 2006: Turbulent velocity-variance profiles in the stable boundary layer generated by a nocturnal low-level jet. *Journal of the Atmospheric Sciences*, **63 (11)**, 2700–2719, https://doi.org/10.1175/JAS3776.1.

Banta, R. M., Y. L. Pichugina, and W. A. Brewer, 2015: Nocturnal low-level jet

characteristics over a wind turbine array. *Boundary-Layer Meteorology*, **157 (1)**, 95–122, https://doi.org/10.1007/s10546-015-0056-9.

Banta, R. M., Y. L. Pichugina, N. D. Kelley, R. M. Hardesty, and W. A. Brewer, 2013: Wind energy meteorology: Insight into wind properties in the turbine-rotor layer of the atmosphere from high-resolution Doppler lidar. *Bulletin of the American Meteorological Society*, **94 (6)**, 883–902, https://doi.org/10.1175/BAMS-D-11-00057.1.

Barthelmie, R. J., S. T. Frandsen, N. M. Nielsen, S. C. Pryor, P.-E. M. Rethore, and H. Ejsing Jørgensen, 2007: Modelling and measurements of power losses and turbulence intensity in wind turbine wakes at Middelgrunden offshore wind farm. *Wind Energy*, **10 (6)**, 517–528, https://doi.org/10.1002/we.238.

Basha, G., and M. V. Ratnam, 2009: Identification of atmospheric boundary layer height over a tropical station using high-resolution radiosonde refractivity profiles: Comparison with gps radio occultation measurements. *Journal of Geophysical Research: Atmospheres*, **114**, D16 101, https://doi.org/10.1029/2008JD011692.

Beck, H., and M. Kühn, 2017: Dynamic data filtering of long-range doppler lidar wind speed measurements. *Remote Sensing*, **9 (6)**, 561, https://doi.org/10.3390/rs9060561.

Bell, T. M., B. R. Greene, P. M. Klein, M. Carney, and P. B. Chilson, 2020: Confronting the boundary layer data gap: evaluating new and existing methodologies of probing the lower atmosphere. *Atmospheric Measurement Techniques*, **13**, 3855–3872, https://doi.org/10.5194/amt-13-3855-2020.

Bell, T. M., P. M. Klein, J. K. Lundquist, and S. Waugh, 2021: Remote-sensing and radiosonde datasets collected in the san luis valley during the lapse-rate campaign. *Earth System Science Data*, **13**, 1041–1051, https://doi.org/10.5194/essd-13-1041-2021.

Belmont, A. D., 1957: Apparent diurnal variations of arctic stratospheric temperatures. *Eos, Transactions American Geophysical Union*, **38 (4)**, 462, https://doi.org/10.1029/TR038i004p00462.

Beniston, M., J. P. Wolf, M. Beniston-Rebetez, H. J. Kölsch, P. Rairoux, and L. Wöste, 2017: Use of lidar measurements and numerical models in air pollution research. *Boundary-Layer Meteorology*, **95 (D7)**, 9879–9894.

Berg, L. K., R. K. Newsom, and D. D. Turner, 2017: Year-long vertical velocity statistics derived from doppler lidar data for the continental convective boundary layer.

Journal of Applied Meteorology and Climatology, **56 (9)**, 2441–2454, https://doi.org/10.1175/JAMC-D-16-0359.1.

Beyrich, F., 1997: Mixing height estimation from sodar data—a critical discussion. *Atmospheric Environment*, **31 (23)**, 3941–3953, https://doi.org/10.1016/S1352-2310(97)00231-8.

Bianco, L., and J. M. Wilczak, 2002: Convective boundary layer depth: Improved measurement by doppler radar wind profiler using fuzzy logic methods. *Journal of Atmospheric and Oceanic Technology*, **19 (11)**, 1745–1758, https://doi.org/10.1175/1520-0426(2002)019⟨1745:CBLDIM⟩2.0.CO;2.

Blackadar, A. K., 1957: Boundary layer wind maxima and their significance for the growth of nocturnal inversions. *Bulletin of the American Meteorological Society*, **38 (5)**, 283–290, https://doi.org/10.1175/1520-0477-38.5.283.

Bodini, N., J. K. Lundquist, and P. Moriarty, 2021: Wind plants can impact long-term local atmospheric conditions. *Scientific Reports*, **11**, 22 939, https://doi.org/10.1038/s41598-021-02089-2.

Bodini, N., D. Zardi, and J. K. Lundquist, 2017: Three-dimensional structure of wind turbine wakes as measured by scanning lidar. *Atmospheric Measurement Techniques*, **10 (8)**, 2881–2896, https://doi.org/10.5194/amt-10-2881-2017.

Bonin, T. A., W. G. Blumberg, P. M. Klein, and P. B. Chilson, 2015: Thermodynamic and turbulence characteristics of the Southern Great Plains nocturnal boundary layer under differing turbulent regimes. *Boundary-Layer Meteorology*, **157 (3)**, 401–420, https://doi.org/10.1007/s10546-015-0072-2.

Bonin, T. A., B. J. Carroll, R. M. Hardesty, W. A. Brewer, K. Hajny, O. E. Salmon, and P. B. Shepson, 2018: Doppler lidar observations of the mixing height in indianapolis using an automated composite fuzzy logic approach. *Journal of Atmospheric and Oceanic Technology*, **35**, 473–490, https://doi.org/10.1175/JTECH-D-17-0159.1.

Bonner, W. D., 1968: Climatology of the low level jet. *Monthly Weather Review*, **96 (12)**, 833–850, https://doi.org/10.1175/1520-0493(1968)096⟨0833:COTLLJ⟩2.0.CO;2.

Bony, S., and Coauthors, 2015: Clouds, circulation and climate sensitivity. *Nature Geoscience*, **8 (4)**, 261–268, https://doi.org/10.1038/ngeo2398.

Bradley, R. S., F. T. Keimig, and H. F. Diaz, 1993: Recent changes in the north american arctic boundary layer in winter. *Journal of Geophysical Research: Atmospheres*,

98 (D5), 8851–8858, https://doi.org/10.1029/93JD00311.

Brock, F. V., K. C. Crawford, R. L. Elliott, G. W. Cuperus, S. J. Stadler, H. L. Johnson, and M. D. Eilts, 1995: The oklahoma mesonet: A technical overview. *Journal of Atmospheric and Oceanic Technology*, **12 (1)**, 5–19, https://doi.org/10.1175/1520-0426(1995)012⟨0005:TOMAT⟩2.0.CO;2.

Browning, K. A., and R. Wexler, 1968: The determination of kinematic properties of a wind field using doppler radar. *Journal of Applied Meteorology*, **7**, 105–113, https://doi.org/10.1175/1520-0450(1968)007⟨0105:TDOKPO⟩2.0.CO;2.

Brugger, P., C. D. Markfort, and F. Porté-Agel, 2022: Field measurements of wake meandering at a utility-scale wind turbine with nacelle-mounted doppler lidars. *Wind Energy Science*, **7**, 185–199, https://doi.org/10.5194/wes-7-185-2022.

Caicedo, V., B. Rappenglück, B. Lefer, G. Morris, D. Toledo, and R. Delgado, 2017: Comparison of aerosol lidar retrieval methods for boundary layer height detection using ceilometer aerosol backscatter data. *Atmospheric Measurement Techniques*, **10 (4)**, 1609–1622, https://doi.org/10.5194/amt-10-1609-2017.

Calaf, M., C. Meneveau, and J. Meyers, 2010: Large eddy simulation study of fully developed wind-turbine array boundary layers. *Physics of Fluids*, **22 (1)**, 015 110, https://doi.org/10.1063/1.3291077.

Calaf, M., M. B. Parlange, and C. Meneveau, 2011: Large eddy simulation study of scalar transport in fully developed wind-turbine array boundary layers. *Physics of Fluids*, **23 (12)**, 126 603, https://doi.org/10.1063/1.3663376.

Campagnolo, F., F. Castellani, F. Natili, D. Astolfi, and F. Mühle, 2022: Wind tunnel testing of yaw by individual pitch control applied to wake steering. *Frontiers in Energy Research*, **10**, 883 889, https://doi.org/10.3389/fenrg.2022.883889.

Carlin, J. T., E. N. Smith, and K. Giannakopoulos, 2024: Contextualizing polarimetric retrievals of boundary layer height using state-of-the-art boundary layer profiling. *Journal of Applied Meteorology and Climatology*, **63 (7)**, 765–780, https://doi.org/10.1175/JAMC-D-23-0231.1.

Carroll, B. J., B. B. Demoz, and R. Delgado, 2019: An overview of low-level jet winds and corresponding mixed layer depths during PECAN. *Journal of Geophysical Research: Atmospheres*, **124 (17)**, 9141–9163, https://doi.org/10.1029/2019JD030658.

Cañadillas, B., R. Foreman, S. Barth, B. Sanderse, and S. Emeis, 2019: Lidar measure-

ments of offshore wind turbine wakes: Observations of wake structure and evolution. *Wind Energy Science*, **4 (3)**, 355–368, https://doi.org/10.5194/wes-4-355-2019.

Chamorro, L. P., M. Guala, R. E. A. Arndt, and F. Sotiropoulos, 2012: On the evolution of turbulent scales in the wake of a wind turbine model. *Journal of Turbulence*, **13**, 1–13, https://doi.org/10.1080/14685248.2012.697169.

Chamorro, L. P., and F. Porté-Agel, 2009: A wind-tunnel investigation of wind-turbine wakes: Boundary-layer turbulence effects. *Boundary-Layer Meteorology*, **132**, 129–149, https://doi.org/10.1007/s10546-009-9380-8.

Christiansen, M. B., and C. B. Hasager, 2005: Wake effects of large offshore wind farms identified from satellite sar. *Remote Sensing of Environment*, **98 (2–3)**, 251–268, https://doi.org/10.1016/j.rse.2005.07.009.

Churchfield, M. J., S. Lee, J. Michalakes, and P. J. Moriarty, 2012: A numerical study of the effects of atmospheric and wake turbulence on wind turbine dynamics. *Journal of Turbulence*, **13 (14)**, 1–32, https://doi.org/10.1080/14685248.2012.668191.

Collaud Coen, M., C. Praz, A. Haefele, D. Ruffieux, P. Kaufmann, and B. Calpini, 2014: Determination and climatology of the planetary boundary layer height above the swiss plateau by in situ and remote sensing measurements as well as by the cosmo-2 model. *Atmospheric Chemistry and Physics*, **14**, 13 205–13 221, https://doi.org/10.5194/acp-14-13205-2014.

Coniglio, M. C., J. Correia, P. T. Marsh, and F. Kong, 2013: Verification of convection-allowing wrf model forecasts of the planetary boundary layer using sounding observations. *Weather and Forecasting*, **28**, 842–862, https://doi.org/10.1175/WAF-D-12-00103.1.

Crum, T. D., and R. L. Alberty, 1993: The wsr-88d and the wsr-88d operational support facility. *Bulletin of the American Meteorological Society*, **74 (9)**, 1669–1687, https://doi.org/10.1175/1520-0477(1993)074⟨1669:TWATWO⟩2.0.CO;2.

de Arruda Moreira, G., and Coauthors, 2018: Study of the planetary boundary layer by microwave radiometer, elastic lidar and doppler lidar estimations in southern iberian peninsula. *Atmospheric Research*, **213**, 185–195, https://doi.org/10.1016/j.atmosres.2018.06.007.

Debnath, M., and Coauthors, 2022: Design of the american wake experiment (awaken) field campaign. *Journal of Physics: Conference Series*, **2265**, 022 058, https://doi.org/10.1088/1742-6596/2265/2/022058.

Draper, M., A. Guggeri, and G. Usera, 2016: Validation of the Actuator Line Model with coarse resolution in atmospheric sheared and turbulent inflow. *Journal of Physics: Conference Series*, **753**, 082 007, https://doi.org/10.1088/1742-6596/753/8/082007.

Duncan Jr., J. B., and Coauthors, 2022: Evaluating convective planetary boundary layer height estimations resolved by both active and passive remote sensing instruments during the cheesehead19 field campaign. *Atmospheric Measurement Techniques*, **15 (8)**, 2479–2502, https://doi.org/10.5194/amt-15-2479-2022.

Emeis, S., K. Schäfer, C. Münkel, R. Friedl, and P. Suppan, 2012: Evaluation of the interpretation of ceilometer data with rass and radiosonde data. *Boundary-Layer Meteorology*, **143 (1)**, 25–35, https://doi.org/10.1007/s10546-011-9604-6.

España, G., S. Aubrun, S. Loyer, and P. Devinant, 2012: Wake meandering of a wind turbine wake generated in a turbulent boundary layer. *Journal of Wind Engineering and Industrial Aerodynamics*, **110**, 85–97, https://doi.org/10.1016/j.jweia.2012.03.008.

Fairall, C. W., 1991: Parameterization and micrometeorology of surface fluxes. *Boundary-Layer Meteorology*, **54**, 111–135, https://doi.org/10.1007/BF00122027.

Fedorovich, E., J. A. Gibbs, and A. Shapiro, 2017: Numerical study of nocturnal low-level jets over gently sloping terrain. *Journal of the Atmospheric Sciences*, **74 (9)**, 2813–2834, https://doi.org/10.1175/JAS-D-17-0013.1.

Fernando, H. J. S., F. Porté-Agel, R. B. Cal, and Y.-T. Wu, 2019a: Wind farm wakes and boundary layer interactions: A review. *Renewable and Sustainable Energy Reviews*, **113**, 109 254, https://doi.org/10.1016/j.rser.2019.109254.

Fernando, H. J. S., and Coauthors, 2019b: The perdigão: Peering into microscale details of mountain winds. *Bulletin of the American Meteorological Society*, **100**, 799–820, https://doi.org/10.1175/BAMS-D-17-0227.1.

Fitch, A. C., J. B. Olson, and J. K. Lundquist, 2013: Mesoscale influences of wind farms throughout a diurnal cycle. *Monthly Weather Review*, **141 (7)**, 2173–2198, https://doi.org/10.1175/MWR-D-12-00185.1.

Fleming, P., and Coauthors, 2019: Initial results from a field campaign of wake steering applied at a commercial wind farm – Part 1. *Wind Energy Science*, **4**, 273–285, https://doi.org/10.5194/wes-4-273-2019.

Garratt, J. R., 1993: Sensitivity of climate simulations to land-surface and atmospheric

boundary-layer treatments — A review. *Journal of Climate*, **6 (3)**, 419–448.

Garratt, J. R., 1994: Review: the atmospheric boundary layer. *Earth-Science Reviews*, **37 (1-2)**, 89–134.

Garratt, J. R., and R. A. Brost, 1981: Radiative cooling effects within and above the nocturnal boundary layer. *Journal of the Atmospheric Sciences*, **38 (12)**, 2730–2746.

Gebauer, J. G., and T. M. Bell, 2024: A flexible, multi-instrument optimal estimation retrieval for wind profiles. *Journal of Atmospheric and Oceanic Technology*, **41**, 605–620, https://doi.org/10.1175/JTECHD230134.1.

Gebauer, J. G., A. Shapiro, E. Fedorovich, and P. Klein, 2018: Convection initiation caused by heterogeneous low-level jets over the Great Plains. *Monthly Weather Review*, **146 (8)**, 2615–2637, https://doi.org/10.1175/MWR-D-18-0002.1.

Geerts, B., and Coauthors, 2017: The 2015 plains elevated convection at night field project. *Bulletin of the American Meteorological Society*, **98 (4)**, 767–786, https://doi.org/10.1175/BAMS-D-15-00257.1.

Gero, J., and D. Hackel, 2025: Atmospheric emitted radiance interferometer (aeri) instrument handbook. *U.S. Department of Energy, Atmospheric Radiation Measurement (ARM) User Facility*, **DOE/SC-ARM-TR-054**, 1–120, https://doi.org/10.2172/1020273.

Ghobrial, M., T. Stallard, D. M. Schultz, and P. Ouro, 2025: Evaluation of six subgrid-scale models for LES of wind farms in stable and conventionally-neutral atmospheric stratification. *Boundary-Layer Meteorology*, **(4)**, 19, https://doi.org/10.1007/s10546-025-00907-y.

Gierens, R. T., S. Henriksson, M. Josipovic, V. Vakkari, P. G. van Zyl, and J. P. Beukes, 2019: Observing continental boundary-layer structure and evolution over the south african savannah using a ceilometer. *Theoretical and Applied Climatology*, **136 (1-2)**, 333–346.

Gomes, M. B., D. B. Parsons, and J. G. Gebauer, 2025: Using a numerical model to evaluate a proposed mechanism for nocturnal low-level jets and ascent over a warm tongue. *Monthly Weather Review*, **153 (7)**, https://doi.org/10.1175/MWR-D-24-0111.1.

Gourley, J. J., P. Tabary, and J. Parent du Châtelet, 2007: A fuzzy logic algorithm for the separation of precipitating from non-precipitating echoes using polarimetric radar observations. *Journal of Atmospheric and Oceanic Technology*, **24**, 1439–1451,

https://doi.org/10.1175/JTECH2035.1.

Grant, A. L. M., 1997: An observational study of the evening transition boundary-layer. *Quarterly Journal of the Royal Meteorological Society*, **123 (539)**, 657–677, https://doi.org/10.1002/qj.49712353907.

Guo, J., and Coauthors, 2024: A merged continental planetary boundary layer height dataset based on high-resolution radiosonde measurements, era5 reanalysis, and gldas. *Earth System Science Data*, **16 (1)**, 1–14, https://doi.org/10.5194/essd-16-1-2024.

Han, S., H. Bian, X. Tie, Y. Xie, M. Sun, and A. Liu, 2009: Impact of nocturnal planetary boundary layer on urban air pollutants: Measurements from a 250 m tower over tianjin, china. *Journal of Hazardous Materials*, **162**, 264–269, https://doi.org/10.1016/j.jhazmat.2008.05.056.

Hancock, P. E., and P. Hayden, 2024: The wake of a large wind turbine in stable atmospheric boundary layer flow, simulated in the EnFlo stratified-flow wind tunnel. *Journal of Renewable and Sustainable Energy*, **16 (2)**, 023 309, https://doi.org/10.1063/5.0188640.

Hancock, P. E., and F. Pascheke, 2014: Wind-tunnel simulation of the wake of a large wind turbine in a stable boundary layer: Part 2, the wake flow. *Boundary-Layer Meteorology*, **151 (1)**, 23–37, https://doi.org/10.1007/s10546-013-9887-x.

Heffter, J. L., 1980: Surface energy budget studies at the noaa climate monitoring and diagnostic laboratory. *Journal of Climate and Applied Meteorology*, **19 (5)**, 593–610, https://doi.org/10.1175/1520-0450(1980)019⟨0593:SEBSAT⟩2.0.CO;2.

Heinselman, P. L., D. J. Stensrud, R. M. Hluchan, P. L. Spencer, P. C. Burke, and K. L. Elmore, 2009: Radar reflectivity-based estimates of mixed layer depth. *Journal of Atmospheric and Oceanic Technology*, **26 (2)**, 229–239, https://doi.org/10.1175/2008JTECHA1091.1.

Hennemuth, B., and A. Lammert, 2006: Determination of the atmospheric boundary layer height from radiosonde and lidar backscatter. *Boundary-Layer Meteorology*, **120 (1)**, 181–200, https://doi.org/10.1007/s10546-005-9035-3.

Hereon, 2021: Wind energy research report: Assessing local climate impacts of turbine wakes. *Helmholtz-Zentrum Hereon*, **1**, 1–50, https://doi.org/10.48464/hereon.wind2021.

Hicks, M., B. Demoz, K. Vermeesch, and D. Atkinson, 2019: Intercomparison of mix-

ing layer heights from the national weather service ceilometer test sites and collocated radiosondes. *Journal of Atmospheric and Oceanic Technology*, **36 (1)**, 129–137, https://doi.org/10.1175/JTECH-D-18-0058.1.

Hirth, L., S. Muller, M. O'Sullivan, and Coauthors, 2021: The impact of large-scale wind power deployment on electricity markets and system operations. *Renewable Energy*, **169**, 1251–1265, https://doi.org/10.1016/j.renene.2020.12.058.

Hirth, L., F. Ueckerdt, and O. Edenhofer, 2013: The market value of variable renewables: The effect of solar wind power variability on their relative price. *Energy Economics*, **38**, 218–236, https://doi.org/10.1016/j.eneco.2013.02.004.

Holton, J. R., 1967: The diurnal boundary layer wind oscillation above sloping terrain. *Tellus*, **19 (2)**, 199–205, https://doi.org/10.1111/j.2153-3490.1967.tb01473.x.

Holzworth, G. C., 1964: Estimates of mean maximum mixing depths in the contiguous united states. *Monthly Weather Review*, **92 (5)**, 235–242, https://doi.org/10.1175/1520-0493(1964)092⟨0235:EOMMMD⟩2.3.CO;2.

Holzworth, G. C., 1967: Mixing depths, wind speeds and air pollution potential for selected locations in the united states. *Journal of Applied Meteorology*, **6 (6)**, 1039–1044, https://doi.org/10.1175/1520-0450(1967)006⟨1039:MDWSAA⟩2.0.CO;2.

Hu, X.-M., P. M. Klein, M. Xue, J. K. Lundquist, F. Zhang, and Y. Qi, 2013: Impact of low-level jets on the nocturnal urban heat island intensity in Oklahoma City. *Journal of Applied Meteorology and Climatology*, **52 (8)**, 1779–1802, https://doi.org/10.1175/JAMC-D-12-0256.1.

Hyvärinen, A., and A. Segalini, 2018: A wind-tunnel study of the wake development behind wind turbines over sinusoidal hills. *Wind Energy*, **21 (8)**, 605–617, https://doi.org/10.1002/we.2181.

Iowa Environmental Mesonet, Iowa State University, 2021: Norman westheimer airport automatic surface observing system (asos) archives. URL https://mesonet.agron.iastate.edu/, accessed online via the Iowa Environmental Mesonet (Iowa State University).

Jordan, A. M., E. N. Smith, J. T. Carlin, P. M. Klein, and S. Wharton, 2026: Validation of boundary-layer height detection methods for southern great plains u.s. summer cases. *Boundary-Layer Meteorology*, submitted.

Jordan, A. M., E. N. Smith, P. M. Klein, J. G. Gebauer, and S. Wharton, 2024: Probing the atmospheric boundary layer with integrated remote-sensing platforms

during the american wake experiment (awaken) campaign. *Journal of Renewable and Sustainable Energy*, **16**, 063 305, https://doi.org/10.1063/5.0211717.

Keck, R.-E., M. de Maré, M. J. Churchfield, S. Lee, G. Larsen, and H. A. Madsen, 2014a: On atmospheric stability in the dynamic wake meandering model. *Wind Energy*, **17 (11)**, 1689–1710, https://doi.org/10.1002/we.1662.

Keck, R.-E., R. Mikkelsen, N. Troldborg, M. de Maré, and K. S. Hansen, 2014b: Synthetic atmospheric turbulence and wind shear in large eddy simulations of wind turbine wakes. *Wind Energy*, **17**, 1247–1267, https://doi.org/10.1002/we.1631.

Keeler, E., 2025: Balloon-borne sounding system (sonde) instrument handbook. Tech. Rep. DOE/SC-ARM-TR-029, U.S. Department of Energy, Atmospheric Radiation Measurement (ARM) User Facility. URL https://www.arm.gov/publications/tech_reports/handbooks/sonde_handbook.pdf, dOE/SC-ARM-TR-029.

Klein, P. M., X.-M. Hu, and M. Xue, 2014: Impacts of mixing processes in nocturnal atmospheric boundary layer on urban ozone concentrations. *Boundary-Layer Meteorology*, **150 (1)**, 107–130, https://doi.org/10.1007/s10546-013-9864-4.

Klein, P. M., and Coauthors, 2015: LABLE: A multi-institutional, student-led, atmospheric boundary layer experiment. *Bulletin of the American Meteorological Society*, **96 (10)**, 1665–1686, https://doi.org/10.1175/BAMS-D-13-00267.1.

Knuteson, R. O., and Coauthors, 2004a: Atmospheric emitted radiance interferometer. part i: Instrument design. *Journal of Atmospheric and Oceanic Technology*, **21 (12)**, 1763–1776, https://doi.org/10.1175/JTECH-1662.1.

Knuteson, R. O., and Coauthors, 2004b: Atmospheric emitted radiance interferometer. part ii: Instrument performance. *Journal of Atmospheric and Oceanic Technology*, **21 (12)**, 1777–1789, https://doi.org/10.1175/JTECH-1663.1.

Kotthaus, S., and Coauthors, 2023: Atmospheric boundary layer height from ground-based remote sensing: a review of capabilities and limitations. *Atmospheric Measurement Techniques*, **16 (2)**, 433–479, https://doi.org/10.5194/amt-16-433-2023.

Krishnamurthy, R., M. Calaf, and M. Chamecki, 2017: Impact of wind turbines on atmospheric turbulence and flow structures in the atmospheric boundary layer. *Boundary-Layer Meteorology*, **165 (3)**, 519–541, https://doi.org/10.1007/s10546-017-0281-0.

Krishnamurthy, R., R. K. Newsom, L. K. Berg, H. Xiao, P.-L. Ma, and D. D. Turner,

2021a: On the estimation of boundary layer heights: a machine learning approach. *Atmospheric Measurement Techniques*, **14 (6)**, 4403–4424, https://doi.org/10.5194/amt-14-4403-2021.

Krishnamurthy, R., and Coauthors, 2021b: Boundary layer climatology at ARM southern great plains. Tech. Rep. PNNL-30832, Pacific Northwest National Laboratory. URL https://www.pnnl.gov/main/publications/external/technical_reports/PNNL-30832.pdf.

Krishnamurthy, R., and Coauthors, 2025: Observations of wind farm wake recovery at an operating wind farm. *Wind Energy Science*, **10**, 361–380, https://doi.org/10.5194/wes-10-361-2025.

Kumjian, M. R., 2013: Principles and applications of dual-polarization weather radar. part i: Description of the polarimetric radar variables. *Journal of Operational Meteorology*, **1 (19)**, 226–242, https://doi.org/10.15191/nwajom.2013.0119.

Lamraoui, F., J. F. Booth, C. M. Naud, M. P. Jensen, and K. L. Johnson, 2019: The interaction between boundary layer and convection schemes in a WRF simulation of post cold frontal clouds over the ARM east north atlantic site. *Journal of Geophysical Research: Atmospheres*, **124 (8)**, 4699–4721, https://doi.org/10.1029/2018JD029370.

Larsén, X. G., and J. Fischereit, 2021: A case study of wind farm effects using two wake parameterizations in the Weather Research and Forecasting (WRF) model (V3.7.1) in the presence of low-level jets. *Geoscientific Model Development*, **14 (5)**, 3141–3158, https://doi.org/10.5194/gmd-14-3141-2021.

Lenschow, D. H., M. Lothon, S. D. Mayor, P. P. Sullivan, and G. Canut, 2012: A comparison of higher-order vertical velocity moments in the convective boundary layer from lidar with in situ measurements and large-eddy simulation. *Boundary-Layer Meteorology*, **143 (1)**, 107–123, https://doi.org/10.1007/s10546-011-9615-3.

Lenschow, D. H., V. Wulfmeyer, and C. Senff, 2000: Measuring second-through fourth-order moments in noisy data. *Journal of Atmospheric and Oceanic Technology*, **17 (10)**, 1330–1347, https://doi.org/10.1175/1520-0426(2000)017⟨1330:MSFOMI⟩2.0.CO;2.

Li, H., B. Liu, X. Ma, S. Jin, Y. Ma, Y. Zhao, and W. Gong, 2021: Evaluation of retrieval methods for planetary boundary layer height based on radiosonde data. *Atmospheric Measurement Techniques*, **14**, 5977–5986, https://doi.org/10.5194/amt-14-5977-2021.

Lindley, T. T., D. A. Speheger, M. A. Day, G. P. Murdoch, B. R. Smith, N. J. Nauslar, and D. C. Daily, 2019: Megafires on the southern Great Plains. *Journal of Operational Meteorology*, **7 (12)**, 164–179, https://doi.org/10.15191/nwajom.2019.0712.

Lissaman, P. B. S., 1979: Energy effectiveness of arbitrary arrays of wind turbines. *Journal of Energy*, **3 (5)**, 323–328, https://doi.org/10.2514/3.62441.

Liu, H., and V. Chandrasekar, 2000: Classification of hydrometeors based on polarimetric radar measurements: development of fuzzy logic and neuro-fuzzy systems, and *in situ* verification. *Journal of Atmospheric and Oceanic Technology*, **17**, 140–164, https://doi.org/10.1175/1520-0426(2000)017⟨0140:COHBOP⟩2.0.CO;2.

Liu, S., and X.-Z. Liang, 2010: Observed structure of the planetary boundary layer over north america and its evaluation in three reanalyses. *Journal of Climate*, **23 (21)**, 5774–5800, https://doi.org/10.1175/2010JCLI3430.1.

Lundquist, J. K., M. J. Churchfield, I. Djalalova, A. Clifton, and J. Michalakes, 2019: Atmospheric processes in wind farm wakes and their impacts on energy production. *Journal of Renewable and Sustainable Energy*, **11**, 053 301, https://doi.org/10.1063/1.5108919.

Maahn, M., D. D. Turner, U. Löhnert, D. J. Posselt, K. Ebell, G. C. Mace, and J. M. Comstock, 2020: Optimal estimation retrievals and their uncertainties: What every atmospheric scientist should know. *Bulletin of the American Meteorological Society*, **101**, E1512–E1523, https://doi.org/10.1175/BAMS-D-19-0027.1.

Machefaux, E., G. C. Larsen, N. Troldborg, K. S. Hansen, N. Angelou, T. Mikkelsen, and J. Mann, 2016: Investigation of wake interaction using full-scale lidar measurements and large eddy simulation. *Wind Energy*, **19 (8)**, 1535–1551, https://doi.org/10.1002/we.1936.

Mahale, V. N., J. Vivekanandan, P. Tabary, K. Kerbrat, and J. J. Gourley, 2014: Fuzzy logic classification of s-band polarimetric radar echoes to identify three-body scattering and improve data quality. *Journal of Atmospheric and Oceanic Technology*, **31**, 2168–2181, https://doi.org/10.1175/JTECHD1300174.1.

Mahrt, L., 1999: Stratified atmospheric boundary layers. *Boundary-Layer Meteorology*, **90 (3)**, 375–396.

Mehta, D., A. H. van Zuijlen, B. Koren, J. G. Holierhoek, and H. Bijl, 2014: Large Eddy Simulation of wind farm aerodynamics: A review. *Journal of Wind Engineering and Industrial Aerodynamics*, **133**, 1–17, https://doi.org/10.1016/j.jweia.2014.07.002.

Melnikov, V. M., R. J. Doviak, D. S. Zrnić, and D. J. Stensrud, 2011: Mapping bragg scatter with a polarimetric wsr-88d. *Journal of Atmospheric and Oceanic Technology*, **28 (10)**, 1273–1285, https://doi.org/10.1175/JTECHD1005048.1.

Melnikov, V. M., R. J. Doviak, D. S. Zrnić, and D. J. Stensrud, 2013: Structures of bragg scatter observed with the polarimetric wsr-88d. *Journal of Atmospheric and Oceanic Technology*, **30 (7)**, 1253–1258.

Mitchell, M. K., R. W. Arritt, and K. Labas, 1995: A climatology of the warm season Great Plains low-level jet using wind profiler observations. *Weather and Forecasting*, **10 (4)**, 576–591.

Moriarty, P., and Coauthors, 2020: American wake experiment (awaken). *Technical Report, American WAKE experimeNt (AWAKEN)*, **1**, 1–44, https://doi.org/10.2172/1659798.

Moriarty, P., and Coauthors, 2024: Overview of preparation for the american wake experiment (awaken). *Journal of Renewable and Sustainable Energy*, **16**, 053 306, https://doi.org/10.1063/5.0141683.

National Centers for Environmental Information, 2026: National centers for environmental information. Accessed: YYYY-MM-DD, https://www.ncei.noaa.gov/.

Neunaber, I., M. Hölling, J. Whale, and J. Peinke, 2021: Comparison of the turbulence in the wakes of an actuator disc and a model wind turbine by higher order statistics: A wind tunnel study. *Renewable Energy*, **179**, 1650–1662, https://doi.org/10.1016/j.renene.2021.08.002.

Newman, J. F., P. M. Klein, S. Wharton, A. Sathe, T. A. Bonin, P. B. Chilson, and A. Muschinski, 2016: Evaluation of three lidar scanning strategies for turbulence measurements. *Atmospheric Measurement Techniques*, **9**, 1993–2013, https://doi.org/10.5194/amt-9-1993-2016.

Newsom, R. K., 2012: Doppler lidar (dl) handbook. Tech. Rep. DOE/SC-ARM-TR-101, Atmospheric Radiation Measurement (ARM) Climate Research Facility, U.S. Department of Energy. https://doi.org/10.2172/1034640, URL https://digital.library.unt.edu/ark:/67531/metadc838147/.

Newsom, R. K., and R. Krishnamurthy, 2022: Doppler lidar (dl) instrument handbook. Tech. Rep. DOE/SC-ARM-TR-101, Atmospheric Radiation Measurement (ARM) Climate Research Facility, U.S. Department of Energy. https://doi.org/10.2172/1034640, URL https://doi.org/10.2172/1034640.

Parish, T. R., 2000: Forcing of the summertime low-level jet along the California coast. *Journal of Applied Meteorology*, **39 (12)**, 2421–2433, https://doi.org/10.1175/1520-0450(2000)039⟨2421:FOTSLL⟩2.0.CO;2.

Parish, T. R., 2017: On the forcing of the summertime Great Plains low-level jet. *Journal of the Atmospheric Sciences*, **74 (12)**, 3937–3953, https://doi.org/10.1175/JAS-D-17-0059.1.

Parish, T. R., A. R. Rodi, and R. D. Clark, 1988: A case study of the summertime Great Plains low level jet. *Monthly Weather Review*, **116 (1)**, 94–105, https://doi.org/10.1175/1520-0493(1988)116⟨0094:ACSOTS⟩2.0.CO;2.

Park, H. S., A. V. Ryzhkov, D. S. Zrnić, and K. Kim, 2009: The hydrometeor classification algorithm for the polarimetric wsr-88d: Description and application to an mcs. *Weather and Forecasting*, **24**, 730–748, https://doi.org/10.1175/2008WAF2222205.1.

Pearson, G. N., F. Davies, and C. G. Collier, 2009: An analysis of the performance of the ufam pulsed doppler lidar for observing the boundary layer. *Journal of Atmospheric and Oceanic Technology*, **26**, 240–250, https://doi.org/10.1175/2008JTECHA1128.1.

Peña, A., and Coauthors, 2016: Ten years of boundary-layer and wind-power meteorology at høvsøre, denmark. *Boundary-Layer Meteorology*, **158**, 1–26, https://doi.org/10.1007/s10546-015-0079-8.

Pitchford, K. L., and J. London, 1962: The low-level jet as related to nocturnal thunderstorms over Midwest United States. *Journal of Applied Meteorology*, **1 (1)**, 43–47, https://doi.org/10.1175/1520-0450(1962)001⟨0043:TLLJAR⟩2.0.CO;2.

Platis, A., T. K. Barlas, A. N. Hahmann, and R. J. Barthelmie, 2018: Wind farm wake effects on local microclimate and energy production. *Renewable Energy*, **118**, 250–262, https://doi.org/10.1016/j.renene.2017.11.051.

Porté-Agel, F., M. Bastankhah, and S. Shamsoddin, 2020: Wind-Turbine and Wind-Farm Flows: A Review. *Boundary-Layer Meteorology*, **174 (1)**, 1–59, https://doi.org/10.1007/s10546-019-00473-0.

Porté-Agel, F., M. Bastankhah, and S. Shamsoddin, 2020: Wind-turbine and wind-farm flows: A review. *Boundary-Layer Meteorology*, **174**, 1–59, https://doi.org/10.1007/s10546-019-00473-0.

Porté-Agel, F., Y. Wu, H. Lu, and R. J. Conzemius, 2011: Large-eddy simulation of atmospheric boundary layer flow through wind turbines and wind farms. *Journal of*

Wind Engineering and Industrial Aerodynamics, **99 (4)**, 154–168, https://doi.org/10.1016/j.jweia.2011.01.011.

Poulos, G. S., and Coauthors, 2002: CASES-99: A comprehensive investigation of the stable nocturnal boundary layer. *Bulletin of the American Meteorological Society*, **83 (4)**, 555–581, https://doi.org/10.1175/1520-0477(2002)083⟨0555:CACIOT⟩2.3.CO;2.

Quint, D., J. K. Lundquist, N. Bodini, and D. Rosencrans, 2025: Simulated meteorological impacts of offshore wind turbines and sensitivity to the amount of added turbulence kinetic energy. *Wind Energy Science*, **10**, 1269–1301, https://doi.org/10.5194/wes-10-1269-2025.

Radünz, W. C., and Coauthors, 2025: Influence of simple terrain on the spatial variability of a low-level jet and wind farm performance in the awaken field campaign. *Wind Energy Science*, **10 (10)**, 2365–2393, https://doi.org/10.5194/wes-10-2365-2025.

Rajewski, D. A., E. S. Takle, A. VanLoocke, and S. L. Purdy, 2020: Observations show that wind farms substantially modify the atmospheric boundary layer thermal stratification transition in the early evening. *Geophysical Research Letters*, **47 (6)**, e2019GL086 010, https://doi.org/10.1029/2019GL086010.

Rife, D. L., J. O. Pinto, A. J. Monaghan, C. A. Davis, and J. R. Hannan, 2010: Global distribution and characteristics of diurnally varying low-level jets. *Journal of Climate*, **23 (19)**, 5041–5064, https://doi.org/10.1175/2010JCLI3514.1.

Riihimaki, L. D., T. Shippert, and D. D. Turner, 2019: Atmospheric emitted radiance interferometer optimal estimation (aerioe) value-added product report. Tech. Rep. DOE/SC-ARM-TR-234, Atmospheric Radiation Measurement (ARM) Climate Research Facility, U.S. Department of Energy. https://doi.org/10.2172/1808550, URL https://doi.org/10.2172/1808550.

Rodgers, C. D., 2000: Inverse methods for atmospheric sounding: Theory and practice. *World Scientific, Series on Atmospheric, Oceanic and Planetary Physics*, **2**, 238–256, https://doi.org/10.1142/3171.

Rose, T., S. Crewell, U. Löhnert, and C. Simmer, 2005: A network-suitable microwave radiometer for operational monitoring of the cloudy atmosphere. *Atmospheric Research*, **75**, 183–200, https://doi.org/10.1016/j.atmosres.2004.12.005.

Ryzhkov, A., P. Zhang, H. Reeves, M. Kumjian, T. Tschallener, S. Trömel, and C. Simmer, 2016: Quasi-vertical profiles – a new way to look at polarimetric radar data. *Journal of Atmospheric and Oceanic Technology*, **33 (3)**, 551–562, https://doi.org/

10.1175/JTECHD150020.1.

Santanello, J. A., M. A. Friedl, and M. B. Ek, 2007: Convective planetary boundary layer interactions with the land surface at diurnal time scales: Diagnostics and feedbacks. *Journal of Hydrometeorology*, **8 (5)**, 1082–1097.

Sathe, A., J. Mann, N. Vasiljevic, and G. Lea, 2015: A six-beam method to measure turbulence statistics using ground-based wind lidars. *Atmospheric Measurement Techniques*, **8**, 729–740, https://doi.org/10.5194/amt-8-729-2015.

Savitzky, A., and M. J. E. Golay, 1964: Smoothing and differentiation of data by simplified least squares procedures. *Analytical Chemistry*, **36 (8)**, 1627–1639, https://doi.org/10.1021/ac60214a047.

Sawyer, V., and Z. Li, 2013: Detection, variations and intercomparison of the planetary boundary layer depth from radiosonde, lidar and infrared spectrometer. *Atmospheric Environment*, **79**, 518–528, https://doi.org/10.1016/j.atmosenv.2013.07.019.

Saxion, D. S., and R. L. Ice, 2012: New science for the wsr-88d: Status of the dual polarization upgrade. *92nd American Meteorological Society Annual Meeting & 28th Conference on Interactive Information Processing Systems (IIPS)*, New Orleans, LA, conference paper.

Schneemann, J., A. Clifton, J. K. Lundquist, and M. van der Laan, 2020: Wind farm wake interactions and their influence on energy yield and atmospheric conditions. *Renewable Energy*, **146**, 1191–1205, https://doi.org/10.1016/j.renene.2019.07.122.

Seaman, N. L., and S. A. Michelson, 2000: Mesoscale meteorological structure of a high-ozone episode during the 1995 NARSTO-Northeast study. *Journal of Applied Meteorology*, **39 (3)**, 384–398.

Seibert, P., F. Beyrich, S. Gryning, S. Joffre, A. Rasmussen, and P. Tercier, 2000: Review and intercomparison of operational methods for the determination of the mixing height. *Atmospheric Environment*, **34 (7)**, 1001–1027.

Seidel, D. J., C. O. Ao, and K. Li, 2010: Estimating climatological planetary boundary layer heights from radiosonde observations: Comparison of methods and uncertainty analysis. *Journal of Geophysical Research: Atmospheres*, **115**, D16 113, https://doi.org/10.1029/2009JD013680.

Seidel, D. J., C. O. Ao, K. Li, and Coauthors, 2024: A merged continental planetary boundary layer height dataset based on high-resolution radiosonde measurements, era5 reanalysis, and gldas. *Earth System Science Data*, **16**, 1–?, https://doi.org/

10.5194/essd-16-1-2024.

Seliga, T. A., and V. N. Bringi, 1976: Theory and application of a polarization radar for probing precipitation. *Journal of Applied Meteorology*, **15 (1)**, 69–76, https://doi.org/10.1175/1520-0450(1976)015⟨0069:TAOAAP⟩2.0.CO;2.

Shapiro, A., and E. Fedorovich, 2010: Analytical description of a nocturnal low-level jet. *Quarterly Journal of the Royal Meteorological Society*, **136 (650)**, 1255–1262, https://doi.org/10.1002/qj.628.

Shapiro, A., J. G. Gebauer, and D. B. Parsons, 2022: Emergence of a nocturnal low-level jet from a broad baroclinic zone. *Journal of the Atmospheric Sciences*, **79 (5)**, 1363–1383, https://doi.org/10.1175/JAS-D-21-0187.1.

Siedersleben, S. K., J. K. Lundquist, A. Platis, J. Bange, K. Bärfuss, and A. Lampert, 2018: Microscale effects of wind turbines on local meteorology. *Boundary-Layer Meteorology*, **169 (1)**, 1–25, https://doi.org/10.1007/s10546-018-0363-2.

Sisterson, D. L., R. A. Peppler, T. S. Cress, P. J. Lamb, and D. D. Turner, 2016: The arm southern great plains (sgp) site. *Meteorological Monographs*, **57**, 6.1–6.14, https://doi.org/10.1175/AMSMONOGRAPHS-D-16-0004.1.

Smith, C. M., R. J. Barthelmie, and S. C. Pryor, 2013: Wind farm impacts on local climate: A case study. *Journal of Applied Meteorology and Climatology*, **52 (3)**, 659–670, https://doi.org/10.1175/JAMC-D-12-0120.1.

Smith, E. N., and J. T. Carlin, 2024: A multi-instrument fuzzy logic boundary-layer-top detection algorithm. *Atmospheric Measurement Techniques*, **17**, 4087–4107, https://doi.org/10.5194/amt1740872024.

Smith, E. N., J. G. Gebauer, P. M. Klein, E. Fedorovich, and J. A. Gibbs, 2019: The Great Plains low-level jet during PECAN: Observed and simulated characteristics. *Monthly Weather Review*, **147 (6)**, 1845–1869, https://doi.org/10.1175/MWR-D-18-0293.1.

Solheim, F., J. Godwin, E. Westwater, Y. Han, S. Keihm, K. Marsh, and R. Ware, 1998: Radiometric profiling of temperature, water vapor, and cloud liquid water using various inversion methods. *Radio Science*, **33 (3)**, 393–404, https://doi.org/10.1029/97RS03656.

Song, J., K. Liao, R. L. Coulter, and B. M. Lesht, 2005: Climatology of the low-level jet at the southern Great Plains Atmospheric Boundary Layer Experiments site. *Journal of Applied Meteorology*, **44 (10)**, 1593–1606, https://doi.org/10.1175/JAM2294.1.

Sørensen, J. H., A. Rasmussen, and H. Svensmark, 1996: Forecast of atmospheric boundary-layer height utilised for ETEX real-time dispersion modelling. *Physics and Chemistry of the Earth*, **21 (5–6)**, 435–439.

Stanislawski, B. J., R. Thedin, A. Sharma, E. Branlard, G. Vijayakumar, and M. A. Sprague, 2023: Effect of the integral length scales of turbulent inflows on wind turbine loads. *Renewable Energy*, **217**, 119 218, https://doi.org/10.1016/j.renene.2023.119218.

Stevens, R. J. A. M., L. A. Martínez-Tossas, and C. Meneveau, 2018: Comparison of wind farm large eddy simulations using actuator disk and actuator line models with wind tunnel experiments. *Renewable Energy*, **116**, 470–478, https://doi.org/10.1016/j.renene.2017.08.072.

Stouffer, B. C., D. J. Stensrud, C. L. Comer, Y. Zhang, and M. R. Kumjian, 2024: An investigation of convective boundary layer depth and entrainment zone properties using dual-polarization radar and balloon-borne observations. *Journal of Atmospheric and Oceanic Technology*, **41 (12)**, 1213–1228, https://doi.org/10.1175/JTECH-D-23-0165.1.

Stull, R. B., 1988: *An Introduction to Boundary Layer Meteorology*. Kluwer Academic Publishers, Dordrecht.

Summa, D., P. Di Girolamo, D. Stelitano, and M. Cacciani, 2013: Characterization of the planetary boundary layer height and structure by raman lidar: comparison of different approaches. *Atmospheric Measurement Techniques*, **6 (12)**, 3515–3525, https://doi.org/10.5194/amt-6-3515-2013.

Sun, J., 2011: Vertical variations of mixing lengths under neutral and stable conditions during cases-99. *Journal of Applied Meteorology and Climatology*, **50 (10)**, 2030–2041, https://doi.org/10.1175/JAMC-D-11-010.1.

Tennekes, H., and J. L. Lumley, 1972: *A First Course in Turbulence*. MIT Press, Cambridge, MA.

Tobin, D. M., and M. R. Kumjian, 2017: Polarimetric radar and surface-based precipitation-type observations of ice pellet to freezing rain transitions. *Weather and Forecasting*, **32 (6)**, 2065–2082, https://doi.org/10.1175/WAF-D-17-0054.1.

Trier, S. B., C. A. Davis, D. A. Ahijevych, M. L. Weisman, and G. H. Bryan, 2006: Mechanisms supporting long-lived episodes of propagating nocturnal convection within a 7-day WRF model simulation. *Journal of the Atmospheric Sciences*, **63 (10)**, 2437–2461, https://doi.org/10.1175/JAS3768.1.

Tucker, S. C., C. J. Senff, A. M. Weickmann, W. A. Brewer, R. M. Banta, S. P. Sandberg, D. C. Law, and R. M. Hardesty, 2009: Doppler lidar estimation of mixing height using turbulence, shear, and aerosol profiles. *Journal of Atmospheric and Oceanic Technology*, **26 (4)**, 673–688, https://doi.org/10.1175/2008JTECHA1157.1.

Turner, D. D., and W. G. Blumberg, 2019: Improvements to the aerioe thermodynamic profile retrieval algorithm. *IEEE Journal of Selected Topics in Applied Earth Observations and Remote Sensing*, **12**, 1339–1354, https://doi.org/10.1109/JSTARS.2018.2874968.

Turner, D. D., and R. G. Ellingson, 2016: The atmospheric radiation measurement (arm) program: Introduction to the first 20 years. *Meteorological Monographs*, **57**, v–x, https://doi.org/10.1175/AMSMONOGRAPHS-D-16-0001.1.

Turner, D. D., R. A. Ferrare, V. Wulfmeyer, and A. J. Scarino, 2014a: Aircraft evaluation of ground-based raman lidar water vapor turbulence profiles in convective mixed layers. *Journal of Atmospheric and Oceanic Technology*, **31 (5)**, 1078–1088, https://doi.org/10.1175/JTECHD1300075.1.

Turner, D. D., and U. Löhnert, 2014: Information content and uncertainties in thermodynamic profiles and liquid cloud properties retrieved from the ground-based atmospheric emitted radiance interferometer (aeri). *Journal of Applied Meteorology and Climatology*, **53**, 752–771, https://doi.org/10.1175/JAMC-D-13-0126.1.

Turner, D. D., and U. Löhnert, 2021: Ground-based temperature and humidity profiling: combining active and passive remote sensors. *Atmospheric Measurement Techniques*, **14**, 3033–3048, https://doi.org/10.5194/amt-14-3033-2021.

Turner, D. D., V. Wulfmeyer, L. K. Berg, and J. H. Schween, 2014b: Water vapor turbulence profiles in stationary continental convective mixed layers. *Journal of Geophysical Research: Atmospheres*, **119 (19)**, 11 151–11 165, https://doi.org/10.1002/2014JD022202.

United States National Weather Service, Field Systems Operations Center, Observing Systems Branch, 2018: Radiosonde replacement system (rrs) workstation user guide for rws software version 3.4.0.2. Includes description of corrected and smoothed radiosonde data processing (e.g., solar heating and other adjustments), https://doi.org/10.25923/1mjd-n765.

U.S. Geological Survey, 2026: U.s. geological survey. Accessed: YYYY-MM-DD, https://www.usgs.gov/.

Vahidi, D., and F. Porté-Agel, 2024: Influence of incoming turbulent scales on the wind

turbine wake: A large-eddy simulation study. *Physics of Fluids*, **36 (9)**, 095 177, https://doi.org/10.1063/5.0222372.

Vajda, A., and Coauthors, 2011: Probabilities of adverse weather affecting transport in europe: Climatology and scenarios up to the 2050s. Tech. rep., Clin. Epigenetics. URL https://helda.helsinki.fi/handle/10138/28592, last accessed: 12 January 2023.

Vanderwende, B. J., J. K. Lundquist, M. E. Rhodes, E. S. Takle, and S. L. Irvin, 2015: Observing and simulating the summertime low-level jet in central iowa. *Monthly Weather Review*, **143**, 2319–2336, https://doi.org/10.1175/MWR-D-14-00325.1.

Vivekanandan, J., D. S. Zrnić, S. M. Ellis, R. Oye, A. V. Ryzhkov, and J. Straka, 1999: Cloud microphysics retrieval using s-band dual-polarization radar measurements. *Bulletin of the American Meteorological Society*, **80**, 381–388, https://doi.org/10.1175/1520-0477(1999)080⟨0381:CMRUSB⟩2.0.CO;2.

Wagner, T. J., P. M. Klein, and D. D. Turner, 2019: A new generation of ground-based mobile platforms for active and passive profiling of the boundary layer. *Bulletin of the American Meteorological Society*, **100**, 137–153, https://doi.org/10.1175/BAMSD170165.1.

Wallace, J. M., and P. V. Hobbs, 2006: *Atmospheric Science: An Introductory Survey*. 2nd ed., Academic Press, Burlington, MA.

Wang, X. Y., and K. C. Wang, 2010: Observed diurnal cycle climatology of planetary boundary layer height. *Journal of Climate*, **23**, 5790–5809.

Wang, X. Y., and K. C. Wang, 2014: Estimation of atmospheric mixing layer height from radiosonde data. *Atmospheric Measurement Techniques*, **7 (6)**, 1701–1709.

Weber, B. L., D. B. Wuertz, D. C. Welsh, and R. McPeek, 1993: Quality controls for profiler measurements of winds and rass temperatures. *Journal of Atmospheric and Oceanic Technology*, **10 (4)**, 452–464, https://doi.org/10.1175/1520-0426(1993)010⟨0452:QCFPMO⟩2.0.CO;2.

Weckwerth, T. M., and Coauthors, 2004: An overview of the international H2O project (IHOP_2002) and some preliminary highlights. *Bulletin of the American Meteorological Society*, **85 (2)**, 253–277, https://doi.org/10.1175/BAMS-85-2-253.

Wharton, S., and J. K. Lundquist, 2011: Atmospheric stability affects wind turbine power collection. *Environmental Research Letters*, **6 (1)**, 014 005, https://doi.org/10.1088/1748-9326/6/1/014005.

Whiteman, C. D., X. Bian, and S. Zhong, 1997: Low-level jet climatology from enhanced rawinsonde observations at a site in the southern Great Plains. *Journal of Applied Meteorology*, **36 (10)**, 1363–1376, https://doi.org/10.1175/1520-0450(1997)036⟨1363:LLJCFE⟩2.0.CO;2.

Wildmann, N., N. Bodini, J. K. Lundquist, L. Bariteau, and J. Wagner, 2019: Estimation of turbulence dissipation rate from doppler wind lidars and in situ instrumentation for the perdigão 2017 campaign. *Atmospheric Measurement Techniques*, **12**, 6401–6423, https://doi.org/10.5194/amt-12-6401-2019.

Wu, Y.-T., and F. Porté-Agel, 2012: Atmospheric turbulence effects on wind-turbine wakes: An LES study. *Energies*, **5 (12)**, 5340–5362, https://doi.org/10.3390/en5125340.

Wyngaard, J. C., and M. A. LeMone, 1980: Observations of the flux richardson number in the unstable surface layer. *Journal of the Atmospheric Sciences*, **37 (9)**, 1791–1801, https://doi.org/10.1175/1520-0469(1980)037⟨1791:OOTFRI⟩2.0.CO;2.

Yang, X., F. Sotiropoulos, R. J. Conzemius, J. N. Wachtler, and M. B. Strong, 2015: Large-eddy simulation of turbulent flow past wind turbines/farms: the Virtual Wind Simulator (VWiS). *Wind Energy*, **18 (12)**, 2025–2045, https://doi.org/10.1002/we.1802.

Yang, Y., X. Chen, and Y. Qi, 2013: Classification of convective/stratiform echoes in radar reflectivity observations using a fuzzy logic algorithm. *Journal of Geophysical Research: Atmospheres*, **118**, 1896–1905, https://doi.org/10.1002/jgrd.50214.

Yassin, M. F., S. K. Almutairi, and A. Al-Hemoud, 2018: Dust storms backward trajectories' and source identification over Kuwait. *Atmospheric Research*, **212**, 158–171.

Ye, J., L. Liu, Q. Wang, S. Hu, and S. Li, 2022: A novel machine learning algorithm for planetary boundary layer height estimation using aeri measurement data. *IEEE Geoscience and Remote Sensing Letters*, **19**, 1–5, https://doi.org/10.1109/LGRS.2021.3073048.

Zhan, W., S. Wang, S. Baidya Roy, and J. K. Lundquist, 2020: Wind turbine wake effects on surface energy fluxes and local climate. *Nature Energy*, **5**, 195–203, https://doi.org/10.1038/s41560-020-0563-7.

Zhang, D., J. Comstock, and V. Morris, 2022: Comparison of planetary boundary layer height from ceilometer with arm radiosonde data. *Atmospheric Measurement Techniques*, **15**, 4735–4749, https://doi.org/10.5194/amt-15-4735-2022.

Zhang, G. J., 2003: Roles of tropospheric and boundary layer forcing in the diurnal cycle of convection in the U.S. southern great plains. *Geophysical Research Letters*, **30 (24)**, https://doi.org/10.1029/2003GL018554.

Zhong, S., J. D. Fast, and X. Bian, 1996: A case study of the Great Plains low-level jet using wind profiler network data and a high-resolution mesoscale model. *Monthly Weather Review*, **124 (5)**, 785–806, https://doi.org/10.1175/1520-0493(1996)124⟨0785:ACSOTG⟩2.0.CO;2.

Zhou, L., Y. Tian, S. Baidya Roy, C. Thorncroft, L. F. Bosart, and Y. Hu, 2012: Impacts of wind farms on land surface temperature. *Nature Climate Change*, **2 (7)**, 539–543, https://doi.org/10.1038/nclimate1505.